PhD-FSTC-2018-71
The Faculty of Sciences, Technology and Communication

DISSERTATION

Presented on 02/10/2018 in Luxembourg

to obtain the degree of

DOCTEUR DE L'UNIVERSITÉ DU LUXEMBOURG

EN SCIENCES DE L'INGÉNIEUR

by

Yu-Chung LIAO
Born on 30 March 1989 in Taichung City, Taiwan

IMPACT OF FLOATING BODIES ON BUILDINGS AND STRUCTURES DURING FLOODING

Dissertation defence committee

Dr-Ing. Bernhard Peters, dissertation supervisor
Professor, Université du Luxembourg (LU)

Dr-Ing. Jürgen Stamm, Vice Chairman
Professor, Technische Universität Dresden (DE)

Dr. Joachim Hansen, Chairman
Professor, Université du Luxembour (LU)

Dr. Patrick Matgen
Lead Research and Technology Associate, Luxembourg Institute of Science and Technology (LU)

Dr. Alvaro Antonio Estupinan Donoso
Postdoctoral Researcher, Ceratizit Group (LU)

Impact of Floating Bodies on Buildings and Structures during Flooding

Yu-Chung Liao

A thesis presented for the degree of
Doctor of Philosophy

Faculty of Science, Technology and Communication
University of Luxembourg
Luxembourg
Oct 2018

Impact of Floating Bodies on Buildings and Structures during Flooding

Yu-Chung LIAO

Abstract

Flood is one of the most serious natural disasters that affect human beings, so how to effectively reduce flood damage to human beings is of vital importance. One of the keys to reducing flood damage is to design buildings effectively enough to withstand flooding and the impact of floating debris on the structures.

Although, many studies exist to address the impact of floods on structures, the impact of floating debris on the buildings and structures, i.e. wall or bridge during flooding have not been fully addressed yet. Thus, the objective of this dissertation is to predict the trajectory of floating debris of rivers during flooding and analyze its impact on the structures.

For achieving this goal, a numerical tool based on the mesh-less method of Smoothed Particle Hydrodynamics (SPH), Discrete Element Method (DEM) and Finite Element Method (FEM) is proposed in this dissertation. Where SPH is employed to describe the fluid flow and DEM is employed to obtain the contact force between the floating debris and structures. And a coupling model of SPH and DEM is presented and implemented based on the OpenFPM, a scalable and open C++ framework for particles and mesh simulation in parallel. Buildings and structures are represented by Finite Element Method (FEM) mesh, for which impact with floating debris is determined. These contacts of floating debris cause forces at the positions of impact, e.g. mechanical load and are evaluated by using commercial Finite Element Analysis (FEA) software Abaqus.

As a result, a numerical tool combing the SPH-DEM and FEA is presented in this dissertation It is worth to notice, that treating the inlet/outlet condition in SPH is a challenging issue due to its Lagrangian nature. A suitable boundary treatment for the inlet / outlet condition in SPH for river flooding problem in 3D is unavailable in literatures. Thus, this dissertation extended the open boundary treatment for SPH using semi-analytical conditions and Riemann solver in 2D (Ferrand et al., 2017) to 3D. Which in results, a new open boundary treatment that is suitable for describing the inlet/outlet condition of SPH in 3D is presented and applied to describe the inlet/outlet condition in this dissertation.

The numerical tool is applied to study the scenario of floating trees, transporting in the Mosel river and hitting the flood control wall at Kesten town in the west Germany during flooding. As the result of simulation shows, the floating trees are driven by the river and heading to the downstream and eventually collide with the flood control wall. This impact causes the flood control wall crack from the position of impact. Which means that the flood control wall is not capable of standing the impact of floating trees that transported in the river.

Overall, this dissertation proposed a 3-way coupling numerical tool that is capable of predicting and analyzing the impact of floating debris on building or structures during flooding.

Acknowledgements

Foremost, I would like to thank my Ph.D. supervisor Bernhard Peters, whose support and constant feedback were of inestimable value for my study. Without his support, it is impossible to obtain this work. I would also like to thank my committee member Dr. Alvaro Estupinan for giving me all the help he could whenever I needed. I am also greatly thankful to Dr. Patrick Matgen for his highly appreciated comments and suggestions all along my study.

I would like to thank the authorities in Luxembourg and Germany, namely Administration de la gestion de l'eau and Wasserwirtschaftsamt Trier for providing advises and data. Many thanks to the High Performance Computing (HPC), I am able to take the advantage of the computational power they provide to reduce the simulation time. Very special thanks to Prof. Dr. Ivo F. Sbalzarini and Mr. Pietro Incardona for providing me the OpenFPM and giving me the relative training. Without their help, it is impossible to

Also, I would like to thank to all my colleagues at the University of Luxembourg, especially Xavier Besseron and Alban Rousset for their aid in increasing the performance of my solver. I would like to thank Mohammad Mohseni and Gabriele Pozzetti for the nice discussions during my stay at the University of Luxembourg. I would like to thank Abdoul Wahid Mainassara C., Andrew Ignatenko, Anas Obeidat, Brice Wendlassida Kabore, Edoardo Copertaro, Fenglei Qi, Florian Hoffmann, Maryam and Mehdi Baniasadi, Mingqiu Wu, Edder Rabadan as well as Pascal Loew for their support and advice during my study.

Last but not the least, I would also like to express my gratitude to my family and my girlfriend for their moral support and warm encouragement. Without their support I would not able to complete this study.

This work has been supported by the National Research Fund (FNR), Luxembourg under AFR (Aid for Research Training) grant (Reference 7690847).

Contents

List of Figures

List of Tables

Abbreviations

AASHTO	**A**merican **A**ssociation of **S**tate **H**ighway and **T**ransportation **O**fficials
ALE	**A**rbitrary **L**agrangian-**E**ulerian
ASCE	**A**merican **S**ociety of **C**ivil **E**ngineers
APR	**A**daptive **P**article **R**efinement
CFD	**C**omputational **F**luid **D**ynamics
CFL	**C**ourant–**F**riedrichs–**L**ewy
CIP	**C**onstrained **I**nterpolation **P**rofile
DEM	**D**iscrete **E**lement **M**ethod
EOS	**E**quation **O**f **S**tate
FEA	**F**inite **E**lement **A**nalysis
FEM	**F**inite **D**ifference **M**ethod
FEM	**F**inite **D**ifference **M**ethod
FEMA	**F**ederal **E**mergency **M**anagement **A**gency
FSI	**F**luid–**S**tructure **I**nteractions
FVM	**F**inite **V**olume **M**ethod
HPC	**High P**erformance **C**omputing
LS	**L**evel **S**et
MPS	**M**oving **P**article **s**emi-implicit
SWE	**S**hallow **W**ater **E**quations
SPH	**S**mooth **P**article **H**ydrodynamics
ISPH	**I**nompressible **S**mooth **P**article **H**ydrodynamics

WCSPH	**W**eakly **C**ompressible **S**mooth **P**article **H**ydrodynamics
USACE	**U**nited **S**tates **A**rmy **C**orps of **E**ngineers
VOF	**V**olume **O**f **F**luid
xXDEM	e**X**tended **D**iscrete **E**lement **M**ethod

Symbols

c	reference speed	Ns/m
d_p	default distance between particles	m
h	kernel length	m
c_0	speed of sound	m/s
$\mathbf{F}$	force	N
g	gravity	m/s^2
I	moment of inertia	J/kg
k	spring stiffness	N/m
l	length	m
m	mass	kg
$\dot{m}$	mass flow rate	kg/s
p	pressure	Pa
r	radius; radial coordinate	m
Re	Reynolds number	-
t	time	s
$\mathbf{T}$	torque	Nm
$\mathbf{v}$	Lagragian velocity	m/s
$\mathbf{u}$	Eulerian velocity	m/s
V	volume	m^3

Greek Symbols

δ	differential operator	-
Δ	difference	-
μ	dynamic viscosity	kg/ms
ν	kinematic viscosity	m^2/s
ρ	density	kg/m^3
$\boldsymbol{\tau}'$	viscous stress tensor	Pa
ω	angular velocity	rad/s
γ	renormalized factor	-

Subscripts

D	drag
f	fluid
fp	fluid-particle interaction
l	liquid
g	gas
i	specie i
ij	effective
n	normal
p	particle
s	solid
R	radius
t	tangential
0	initial value
v	vertex

Chapter 1

Introduction

1.1 Background

Flood is one of the most serious natural disasters affecting human life as reported by Doocy et al. (2013). According to the European Environment Agency, during the period 1998-2009, European countries suffered 213 severe floods, resulting in 1,266 deaths, 500,000 people displaced, and at least 5.2 billion € economic losses. Therefore, it is vital for European countries to introduce flood safety planning to reduce the impact of the flood. One of the key aspects of flood safety planning is to design the structure, which is unavoidable in the flood hazard area, to withstand the flood. In the literature, several methods have been proposed to determine the flood forces for the design of buildings and other structures in the flood hazard area.

And it can be determined by using the following three methods: (1) by using the analytical method (2) by using laboratory test method, or (3) by using the numerical modeling method.

However, a key limitation of determining the flood forces by using the analytical method and the laboratory test method, is that the interaction between the flood and floating bodies is over simplified. Which makes it not suitable to analysis the actual flood forces on the structures and floating bodies with

arbitrary geometry. Moreover, most of the analytical method and the laboratory test method for design flood forces on structures were derived from limited data. Therefore, to better analysis the flood forces on the structure during flooding, the numerical modeling method is required.

The interaction between flooding with its associated transport consists of following three aspects:

- Interaction between the free surface (i.e., the surface of water that is in contact with air) and structures.
- Interaction between floating bodies and waves.
- Interaction between floating bodies and structures.

Much research on interaction between free surface and structures, interaction between floating body and waves and the interaction between floating bodies and structures has been done. For example, Wang et al. (2015) presented a numerical model for analyzing the flood impact on the bridge pier, Liang et al. (2016) developed a numerical model based on the finite volume Godunov-type scheme to model the flow impact on structures under extreme flow conditions, Hu et al. (2000) presented a numerical tool based on the finite volume method to simulate storm waves that is overtopping on coastal structures.

Although, several numerical tools are available for analyzing the interaction between water and structure, a numerical tool for predicting the impact of floating bodies on buildings and structures during flooding is still unavailable in the literature.

1.2 Motivation

Although, both mesh-based and meshless methods have been applied to floating bodies, an impact on buildings/structures caused by a floating body has not been addressed in the literature yet. Therefore, **the objective of this dissertation is to construct a numerical tool that is capable to predict both flow and floating bodies during flooding and their impact on buildings or structures.** The floating bodies are considered as arbitrary shapes represented by triangular meshes and treated as individuals that interact with both fluid and solid. For this purpose, SPH, which according to Zhen et al. (2010) has the advantages of treating free surface flow as compared with the mesh-based method, is employed in this dissertation to describe the fluid flow and the interaction between fluid and solid. And the impact force, caused by floating bodies, is addressed by using DEM. Thus, the interaction between fluid and solid and the interaction between solid and solid can be treated separately. Finally, the FEM is applied to analyze the deformation of structure due to the impact of floating bodies and hydrodynamics pressure of the fluid flow.

1.3 Disposition

- Chapter 2: This chapter covers the literature review of SPH, boundary treatment of SPH, SPH with floating bodies, SPH coupling with DEM.
- Chapter 3: This chapter presents the mathematical model of the SPH and DEM that is used in this dissertation. The boundary condition, including inlet/outlet model, and dissipation methods employed in this dissertation.
- Chapter 4: A series of validation test, including 2D cavity, 3D dam break, 2 boxes floating in the 3D dam break, the free cylinder dropping test and a flow passing though a rectangular duct with inlet/outlet condition are presented in this chapter.
- Chapter 5: This chapter introduces a simulation case and analyzes the impact of floating bodies on flood prevention devices. The test case is constructed based on the Mosel river and the flood protection devices at Kesten town, which is located at the Rheinland-Pfalz region of West Germany.
- Chapter 6: Conclusion, suggestions and future works are given in this chapter.

Chapter 2

Literature Review

2.1 Overview

This literature review discusses the method for calculating the flood forces, its modelling and numerical simulation, and gives a brief overview of the research conducted in the area. A brief review of computational fluid dynamics (CFD) methods for interaction between free surface and structures, interaction between floating bodies and waves and interaction between floating bodies and structures. Lastly, the SPH method is introduced, discussing the main advantages and drawbacks of the method, reviewing the use of SPH for solving fluid-structure problem.

2.2 Flood forces

This section gives a brief overview of common methods for determining the flood forces adopted by the design codes for determining the maximum flood forces acting on the structure. According to American Society of Civil Engineers (ASCE) ASCE (2017) and Federal Emergency Management Agency (FEMA) FEMA (2001), the flood forces include hydrostatic forces, hydrodynamic forces, wave forces and impact forces. The hydrostatic forces are the force of standing or slow rising water acting on the inundated structure,

which can be derived from the difference in water level of two sides of the structure. The hydrodynamic forces are the dynamic effect of the moving water acting on the structure. The wave forces are the force acing on the structure when water waves propagating over the surface of the water and striking on the structure. The impactforces are the force acting on the structure results from the collision between the structure and floating bodies (i.e., any objects transported by water such as cars, trees and any other floating bodies).

2.2.1 Hydrostatic forces

The hydrostatic forces include the hydrostatic horizontal force (i.e., hydrostatic pressure on the vertical element of the structure) and buoyancy (i.e., the hydrostatic force acting on the horizontal element).

2.2.1.1 Hydrostatic horizontal force

The hydrostatic horizontal force derives from the difference in water level on the upstream side and downstream side of the structure. The flood force per unit length it is given by: The hydrostatic forces per unit length can be determined by

$$F_{\textbf{hydrostatic pressure force}} = \frac{\rho g}{2} \cdot (h_{us}^2 - h_{ds}^2) \tag{2.1}$$

where F

Buoyancy is the force exerted by fluid that is in the opposite direction to the gravity. The buoyancy length can be determined by

$$F_{buoyancy} = \rho_{fluid} V_{immersed} \tag{2.2}$$

in which $F_{buoyancy}$ is the buoyancy, ρ_{fluid} is the density of the fluid that the concern object immersed in and $V_{immersed}$ is the volume of water displaced by the concern object.

2.2.2 Hydrodynamic forces

The Hydrodynamic forces are the dynamic effect of the moving water acting on the structure. An additional force is exerted by fluid when the fluid flows around the structure, which can be determined by a function of flow velocity and structural geometry.

According to ASCE (2017), if the velocity of the flow is less than $3.05m/s$, it is considered as the low velocity hydrodyanmic force. To determine low velocity hydrodyanmic force on a vertical structure, the hydrodyamic force can be converted to an equivalent hydrostatic force by increasing the head (depth of the water) above the flood level. This increasing equivalent head can be determined as

$$d_h = \frac{C_d V_{avg}^2}{2g} \tag{2.3}$$

where d_h is equivalent head due to the low velocity of flood flows, V_{avg} is the average velocity of flow and C_d is the drag coefficient (taken from the United States Army Corps of Engineers (USACE) USACE (1984)). After obtaining the equivalent head, then the hydrodynamic force can be determined by

$$F_{hydrodynamic} = \rho d_h H_{\text{design depth}} \tag{2.4}$$

where $F_{hydrodynamic}$ is the equivalent hydrostatic force due to low velocity flow and $H_{\text{design depth}}$ is depth of water level.

TABLE 2.1: Drag Coefficients for Ratios of Width to Height (USACE, 1984)

Width to Height Ratio (b/H)	Drag Coefficient (C_d)
1-12	1.2 5
13–20	1.3
21–32	1.4
33–40	1.5
41–80	1.75
81–120	1.8
>120	2.0

When the velocity of the flow is greater than $3.05m/s$ or a special structure and conditions, a more detailed concept of fluid mechanics model should be adopted. The basic method provided by ASCE (2017) to to determine the hydrodynamic force on the vertical structure is given by

$$F_{hydrodynamic} = C_d \rho \frac{V^2}{2} A \tag{2.5}$$

where C_d is the drag coefficient (taken from Table 2.1), and A is the submerged area of the upstream face of the structure.

2.2.3 Wave forces

The wave forces are the force acing on the structure due to water waves propagating over the surface of the water and striking on the structure. ASCE (2017) suggests that the wave forces of non-breaking and broken wave can be determined by using the same procedures as the one for determining the hydrodynamic forces when the velocity of flow is low.

And, if the water is assumed to be still water, the breaking waves force on a rigid vertical pile or column can be determined by

$$P_{max} = C_p \gamma_w d_s + 1.2 \gamma_w d_s F_t = 1.1 C_p \gamma_w d_s^2 + 2.4 \gamma_w d_s^2 \tag{2.6}$$

where P_{max} is the maximum combined dynamic and static wave pressures, F_t is the wave impact force in unit length acting near the still water elevation. C_p is the dynamic pressure coefficient, γ_w is the unit weight of water and d_s is the still water depth of structure where the waves is breaking.

2.2.4 Impact forces

The impact forces are the force acting on the structure results from the collision between a floating body and structures. In the literature, there are three most common approaches can be found to determine the maximum

impact force when designing the structures that have to withstand the flood. These three approaches are:

- Contact Stiffness Approach
- Impulse-Momentum Approach
- Work-Energy Approach

All these three approaches are based on the one degree of freedom system, which only the mass of the floating body is involved in determining the impact forces. The one degree of freedom system as shown in Fig. 2.1, where $m_{\text{floating body}}$ is mass of the floating body, m_s is mass of the structure, u_b is velocity of the floating body. The impact zone of the structure is considered to have a stiffness k_i and the floating body is considered to have a stiffness k_b with associated a net displacement of x_0 due to the impact. In the one degree of freedom system, the structure is considered to be so heavy that it does not move during the impact and the stiffness of the structure is considered to be rigid, where $k_i >> k_b$, then the model of the one degree system can be described as follows:

$$m_{\text{floating body}}\ddot{x} + \overline{k}x = 0 \tag{2.7}$$

where x is the summation of the displacement of floating body during collision and $\overline{k}$ is the effective contact stiffness between the structure and the floating object during the collision, which can be determined by

$$\frac{1}{\overline{k}} = \frac{1}{k_i} + \frac{1}{k_b} \tag{2.8}$$

Since x is the displacement of the system and at the beginning of the contact, the displacement is equal to 0, which means that $x = 0$ at $t = 0$. And the initial impact velocity of the floating body is u_b, which means $\dot{x} = u_b$ at $t = 0$. If the relationship between displacement and impact force is linear, where $F = \overline{k}x$, then the maximum impact force $F_{\max}$ can be determined by

$$F_{\max} = u_b\sqrt{\overline{k}m_{\text{floating body}}} \tag{2.9}$$

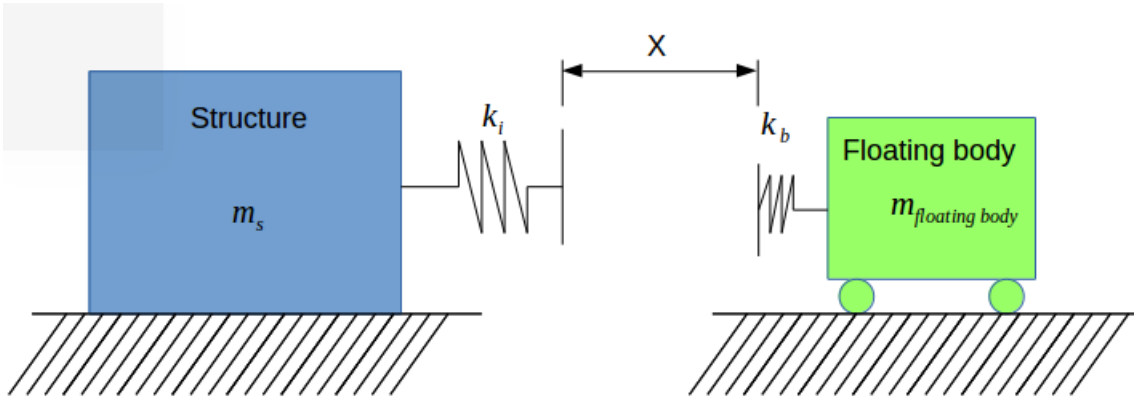

FIGURE 2.1: Schematic of the one degree of freedom model proposed.

2.2.4.1 Contact stiffness approach

The contact stiffness approach is adopted by the American Association of State Highway and Transportation Officials (AASHTO) AASHTO (1997). This approach is originally developed for evaluating maximum vessel impact force on bridge piers, where the impact force depends on the dead-weight tonnage of the vessel, DWT and the vessel velocity. The maximum impact force can be determined by

$$F_{\text{contact stiffness}} = 0.122 u_{\text{vessel}} \sqrt{DWT} \tag{2.10}$$

where $F_{\text{contact stiffness}}$ is the impact force determined by using the contact stiffness approach in MN, u_{vessel} is impact velocity of the vessel in m/s and DWT is the dead weight tons of vessel in $tons$. Haehnel and Daly (2004) suggest that this approach is considered as contact stiffness approach due to this approach requires only the effective contact stiffness of the collision to determine the impact force with known mass and velocity.

2.2.4.2 Impulse-momentum approach

The impulse-momentum approach is adopted by the FEMA (2001) to predict the impact of floating bodies striking the structure. The governing equation of this approach is based on the definition of impulse, which is the integral of force with respect to time:

$$I = \int F dt = \int d(um) \tag{2.11}$$

where I is the impulse of the collision due to the collision between the floating body and the structure. By assuming the momentum of the floating body becomes zero after the impact, the above equation become:

$$F = \frac{um}{t_{duration}} \tag{2.12}$$

where $t_{duration}$ is the impact duration, which is given by FEMA (2000) and shown in Table 2.2.

TABLE 2.2: The impact duration suggested by FEMA (2000)

Type of material	Duration of impact (s)	
	Wall	Pile
Wood	0.7-1.1	0.5-1.0
Steel	NA	0.2-0.4
Reinforced Concrete	0.2-0.4	0.3-0.6
Concrete Masonry	0.3-0.6	0.3-0.6

2.2.4.3 Work energy approach

The work energy approach is adopted by Australian bridge design standard (AS5100, 2004), which comes from the definition of work and energy:

$$W = \int F(x)\partial x = \int (\partial \frac{1}{2} m u^2) \tag{2.13}$$

where W is the work done on the structures with respect of the collision between the structure and the floating body. Assuming the velocity of floating body goes to zero due to the collision, the equation above can be written as follows:

$$W = \int_0^s \overline{k}xdx = \frac{1}{2}mu_0 or W = ks^2 = mu_0^2 \tag{2.14}$$

where s is the stopping distance of the floating body due to the collision. Since, $F_max = ks$, the equation above becomes

$$F_{max} = \frac{mu_0^2}{s} = \frac{wu_0^2}{gs} \tag{2.15}$$

To determine the F_{max}, it is necessary to know the stopping distance. AS5100 (2004) suggests a range of the stopping distance for estimating the maximum impact force of a bridge pier impact by a 2 metric-ton log as Table 2.2 shows.

TABLE 2.3: The stopping distance of pier impact by a 2 metric-ton log recommended by AS5100 (2004).

Material of pier	Stopping distance (s) (mm)
Timber	300
Hollow concrete	150
Concrete	75

2.2.4.4 Summary of flood loads

Although the design codes mentioned above provide a general guideline for determining the maximum of impact force. These design codes only consider the impact force of a single debris on a structure. As a result, the multiple floating bodies impact on the structure simultaneously, which is more likely to happen in the nature, has not been fully addressed yet. And the approaches mentioned above are based on the empirical scale down model, which results in uncertainty of predicting the maximum of impact force. Moreover, these approaches adopted by the design codes are reliant on the

velocity, duration of the impact, impact angle, materials of the structure and location of the impact relative to the building geometry that are challenge to collect. Which in results, to accurately determine the maximum impact forces caused by the floating body is extremely difficult.

2.3 Numerical Modeling of Floods with associated floating bodies

In the field of river engineering, many complex processes have taken place in the process of floods. In the past century, many researches have been carried out through field observation and laboratory experiments. However, the information collected by field observation and laboratory experiments is very limited. In addition, the complexity of floods makes them difficult to measure, difficult to model in laboratory experiments, and expensive. Moreover, when it comes to the problem of the interaction between flood and floating bodies, the earlier established methods in the literature are often analytical methods, which are limited to treating the interaction between flow and floating body with simple geometry. An alternative way to solve the, the numerical methods, such as Computational fluid dynamics (CFD), have been widely applied to address the interaction between flow and floating bodies. The interaction between the flow and floating body is considered as a Fluid–Structure Interactions (FSI) problem, which is a common topic in different engineering topics.

Computational fluid dynamics tool can be categorized into mesh-based methods and meshless method. The mesh-based methods such as Finite Difference Method (FDM), Finite Volume Method (FVM) and Finite Element Method (FEM), have been successfully applied to investigate a wide range of river flooding problems by Ghani et al. (2010), Morvan (2001) and Rüther and Pedersen (2014).

Conventional mesh-based methods such as FVM, FEM and FDM to model interaction between free surface and structures is by applying free-surface

modelling techniques to capture free surfaces. These modelling techniques include Volume of Fluid (VOF) method, Level Set (LS) method and Constrained Interpolation Profile (CIP). However, using these techniques requires a very fine mesh to successfully capture the structure of the fluid surface. This greatly increases the computational cost of simulation.

Due to the actual flow motion is a very non-linear problem, the interaction between floating body and waves becomes a more complicated nonlinear problem. Interaction between floating body and waves is still regarded as a major challenge for the mesh-based methods due to nonlinear coupling between the body motion and the force and motion of floating bodies inside the fluid domain. Furthermore, the motion of floating bodies is far from infinitesimal displacements, which results in a large mesh displacement and distortion. For this purpose, Hadžić et al. (2005) employed sliding mesh as an interface between fixed mesh and moving mesh. Carrica et al. (2007), Henshaw and Schwendeman (2003), Quallen et al. (2014) employed dynamically overlapping grids and the most common way is employed immersed boundary method (IBM) as Calderer et al. (2014), Kallemov et al. (2016), Shen and Chan (2008) demonstrated. Another alternative approach is the Arbitrary Lagrangian-Eulerian (ALE) formulation which combines advantages of both Lagrangian approach and Eulerian approach as Walhorn et al. (2005) presented. However, this approach fails when the large deformation of the fluid surface which leads to excessive element distortion. And it also requires re-meshing in every time steps which make this approach computational costly.

On the contrast to the mesh-based method, meshless method, such as Smooth particle hydrodynamic (SPH) Monaghan (1994) and moving particle semi-implicit (MPS) Koshizuka and Oka (1996), in general, is more capable of dealing with violent free surface flow and fluid-solid interaction compares with mesh-based method as Zhen et al. (2010) and Violeau and Rogers (2016) reported.

2.4 Smooth Particle Hydrodynamic

SPH is a fully Lagrangian meshless method, originally developed to solve astrophysical problems by Lucy (1977) and Gingold and Monaghan (1977), and later extended to solve fluid problems by Monaghan (1992) and Monaghan (1994). The system consists of a set of discrete particles. The physical properties of the fluid particles are calculated by smoothing the kernel function on the basis of neighboring particles. SPH's meshless feature offers several advantages over mesh-based methods (Violeau and Rogers, 2016, Zhen et al., 2010). Firstly, SPH is capable of dealing with the interface between fluid-solid and fluid-air without surface tracking technique. This alleviates the difficulty of coupling moving solid objects in a fluid. Even when a complex geometry is involved in simulation, SPH can still track the rapid distorted free surface. Secondly, SPH is suitable for simulating the highly nonlinear, inertial dominated process flow and its impact. Finally, it is a difficult and time-consuming task for grid based methods to generate quality grid for complex geometries.

2.5 Weakly Compressible Smooth Particle Hydrodynamic and Incompressible Smooth Particle Hydrodynamic

Weakly Compressible smooth particle hydrodynamic (WCSPH) and incompressible smooth particle hydrodynamic (ISPH) are two types of typical SPH framework in the literature. The WCSPH solves the compressible Navier-Stokes equation, and uses an equation of state (EOS) to relate density and pressure. To ensure incompressibility of the fluid, the reference sound speed of fluid should be set as Mach number when obtaining the pressure by using EOS. However, since the Courant–Friedrichs–Lewy (CFL) condition is employed in the most of SPH models, the high reference sound speed lead to very small time steps and which results in increasing of computational cost. Therefore, in practice, the reference speed is only set to 10 times the

maximum speed of the system to allow larger time step and limit the density variation of SPH fluid particles within 1% (Monaghan, 1992).

The ISPH presented by Cummins and Rudman (1999) is considered as a truly incompressible SPH approach, which solves the pressure Poisson equation to obtain the pressure field instead of calculating pressure from density by using EOS. This ensures that the ISPH can achieve higher pressure accuracy than WCSPH as reported by Lee et al. (2008). Moreover, the reference sound speed of the system is no longer required which enables the ISPH to adopt a larger time step.

Although the ISPH seems to be more suitable than WCSPH in the applications of the most engineering problems, this dissertation still applies WCSPH approach with following reasons. Firstly, several methods can be found in the literature to improve the accuracy of WCSPH pressure field, such as using an MLS density filter that is proposed by Colagrossi and Landrini (2003) or adding dissipation terms as Molteni and Colagrossi (2009) proposed. Secondly, no further free surface treatment is required (due to the pressure at free surface is automatically becomes to zero) and the pressure Poisson equation is replaced by EOS when solving the pressure field, which result in faster to construct the code of WCSPH than ISPH. Lastly, since the EOS is adopted in WCSPH, which result in constructing a parallel program of WCSPH is straightforward. Therefore, this thesis only focuses on the WCSPH framework.

2.6 Boundary Treatment

One of the main challenges in SPH is insufficient particles in the support domain, which is the effective area of a particle, to perform an accurate approximation. This support domain problem generally only happens in the fluid surface of fluid or the solid boundary. Colagrossi et al. (2009) concluded that with proper WCSPH formulation, it still satisfies the dynamic free-surface condition without further implementation of explicitly

free-surface terms.

For solid boundaries, several methods have been developed, including repulsive force method, dummy particle boundary, mirror particle method, and normal flux method. In this section, the common boundary methods for solid boundaries in SPH will be introduced.

2.6.1 Repulsive Force Boundary Method

Monaghan (1994) presented a repulsive force boundary method based on Lennard–Jones repulsive force. In this method, as Fig. 2.2 shown, a layer of boundary particles is placed at the boundary and these particles generate paired force exerted on the fluid particles to keep fluid particles inside the computational domain. This method is straightforward to implement, capable of dealing with complex shapes, and computationally cheaper than the other methods. Yet, this approach may have an inconsistency problem, because of the problem of the insufficient particles in the support domain still exists.

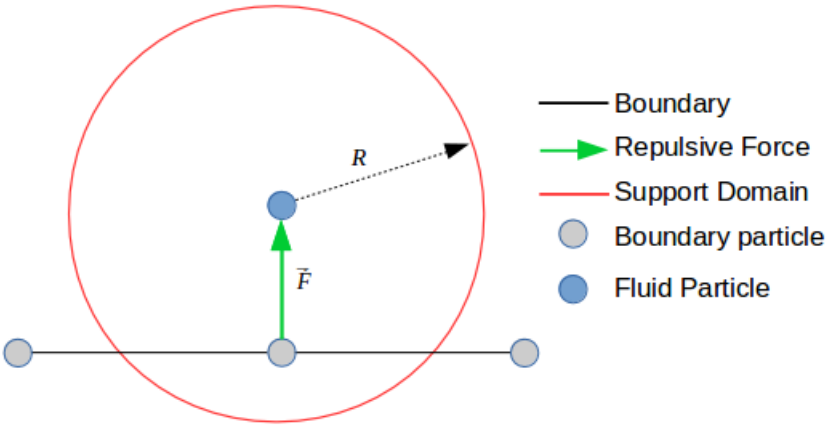

FIGURE 2.2: Sketch of repulsive force boundary method.

2.6.2 Mirror Particle Method

The mirror particle method, as Fig. 2.3 shown, proposed by Morris et al. (1997), is a straightforward method, which the fluid particles are mirrored through the boundary to fill up the void space in the interior of the boundary as Fig. 2.2 shown. And the physical properties of these mirrored particles are adjusted based on the boundary condition. The drawback of this method is that it is computationally more costly than other method since the particles need to be mirrored to another side of boundary in every time step.

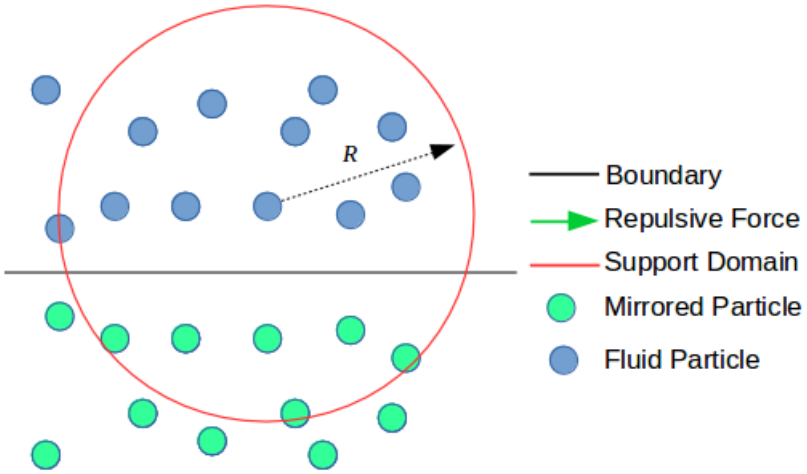

FIGURE 2.3: Sketch of mirror boundary method.

2.6.3 Normal Flux Method

In the normal flux method, a kernel renormalized factor is introduced. This renormalized factor is calculated through surface integrals of the boundaries and as compensation for the missing particles in the field of support on the boundary as Fig. 2.4 shown. This method is applicable for both 2D (Leroy et al., 2014, Mayrhofer et al., 2013, M.Ferrand et al., 2011) and 3D (Mayrhofer et al., 2015a,b). The advantage of this method is that the boundary conditions of Neumann and Dirichlet can be realized as presented

by Ferrand et al. (2017). The drawback of this method is that when a complex 3D geometry boundary is involved, it is necessary to calculate renormalisation factor based on the intersection between particles and boundary through a domain decomposition algorithm. This increases the cost of computation and the difficulty of implementation. Moreover, this method is not suitable for every kind of kernel function. For example, if a Gaussian or a super Gaussian kernel function is employed, then it is impossible to calculate the analytic value of the renormalized factor in 3D (Mayrhofer et al., 2015a).

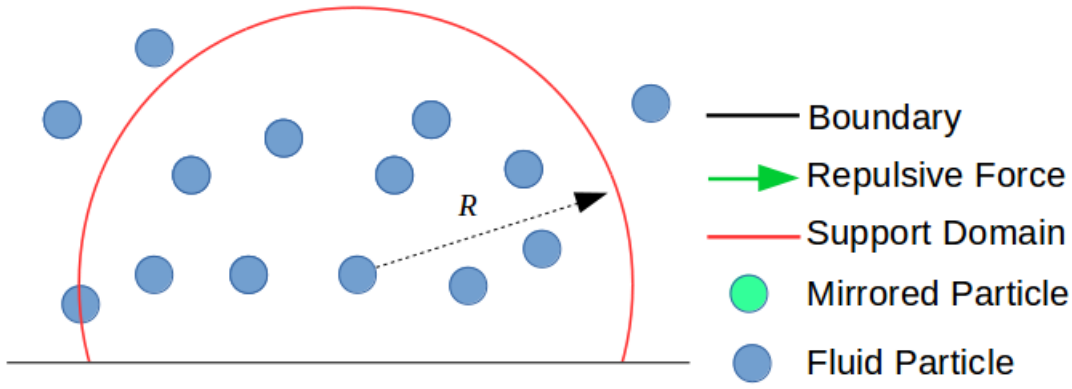

FIGURE 2.4: Sketch of normal flux boundary method.

2.6.4 Dummy Particle Boundary Method

In the dummy particle boundary method, proposed by Libersky et al. (1993), a few layers of fixed particles are deployed outside of the boundary to compensate the void space of support domain of fluid particles that are nearby the wall boundary as Fig. 2.5 shown. Marrone et al. (2010) compared the level set and SPH with dummy particle boundary by using the case dam break flow impact on the structure and the results show that the dummy particle boundary method is an accurate and robust boundary treatment. Adami et al. (2012) introduced a pressure boundary condition to apply on

the dummy particle, which prevents the fluid particle penetrate the wall boundary and increases accuracy. This method has the advantage of being applied to complex three-dimensional geometry, and it is straightforward to construct as parallel code. Therefore, the dummy particle boundary method is applied to deal with the wall boundaries and the surface of floating bodies in this dissertation.

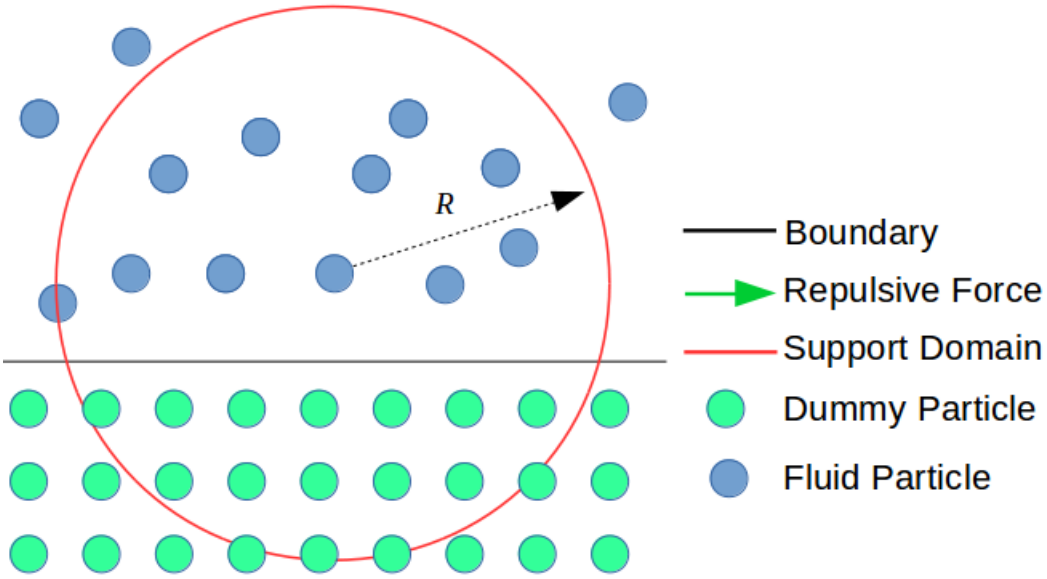

FIGURE 2.5: Sketch of Dummy particle boundary method.

2.7 Flooding with SPH

Based on the advantages of meshless, SPH is considered as one of the most ideal tools for modeling floods. Extensive research has applied SPH to investigate and predict floods. Vacondio (2012) used SPH to solve shallow water equations (SWEs) for modeling Okushiri tsunami in Japan. Kao and Chang (2012) compared the 2D-SPH-SWE model for the flooding problem with the experiment results and conclude that the 2D-SPH-SWE model is

reasonably accurate. However, the SWE equation is not suitable for treating the interaction between flow and the floating body problem. Since the vertical pressure gradients are considered as hydrostatic. Shen et al. (2000) used SPH to simulate the dynamic transport and jamming of surface ice in rivers. Ghazali and Kamsin (2008) presented a model to simulate the river flood in Kuala Lumpur on 10 June 2007. Guo et al. (2017) simulated water flooding into a damaged floating cabin, and their numerical results are in good agreements with experimental data. Prakash et al. (2014) presented a SPH-DEM model for analysing the impact of dam failure in different scenarios. Their research shows that SPH can model flood and debris transport during the flood.

2.8 Floating body in SPH

Monaghan and Kos (2000) are the first one to deal with the interaction between the floating body with and flow by using SPH. In their work, a vertical sinking box, whose acceleration depends on hydrodynamic force, is used to produce a two dimensional solitary wave. Oger et al. (2006b) presented a wedge entering the water surface in 2D and their result shows a fair consistency compared to the analytical and experimental result. For wedge entering water problems, the air cavity enclosed by the water may affect the local free surface profile significantly. Therefore, Gong et al. (2011) employed a two-phase model, which takes the interaction between air and water into consideration and successfully improves the force prediction. Ulrich and Rung (2012) used SPH to model a 3D cube entering the water, their simulation results are in good agreement with the experimental results.

Bouscasse et al. (2013) designed a model to couple viscous Fluid–Solid interactions by using the δ-SPH (a SPH model with numerical diffusive terms) proposed by Antuono et al. (2010). Their model can simulate the interaction between complex viscous flows and floating bodies with a good accuracy.

Sun et al. (2015a) presents an algorithm to improve the accuracy and stability of violent Fluid–Solid interaction problem by using the method presented by Bouscasse et al. (2013) with modified boundary condition based on the model presented by Adami et al. (2012).

The improved dummy particle technique for boundary treatment proposed by Sun et al. (2015a) agrees well with both experimental data and other numerical results, where trajectory of the floating body in the fluid is well captured, in terms of violent fluid–solid interactions. Therefore, their boundary method for treating fluid–solid interactions is adopted to deal with the solid wall boundary in this thesis.

2.9 Inflow/Outflow condition

Currently, three types of methods can be found in the literature for open boundary conditions. The most common method is the buffer particle method (Khorasanizade and Sousa, 2016, Klapp and Sigalotti, 2017, Pahar and Dhar, 2017, Vacondio, 2012). In this method, several layers of buffer particles are placed outside of inflow/outflow boundaries. The physics quantities of these buffer particles are prescribed by the given value and move according to the imposed velocity. Once the buffer particles enter the computational domain from inflow boundary, they are marked as fluid particles and move freely. When the fluid particles pass through the outflow boundary, it will be marked as a buffer and move at a specified velocity. This sudden change, turns a buffer particle into a fluid particle, could lead to a spurious shock wave. Moreover, in this method, open boundary conditions with complex geometric conditions cannot be solved.

Kunz et al. (2016) proposed an inflow/outflow method based on the mirror particle method, which can realize the real Dirichlet boundary conditions.

However, this method is only applicable to ISPH. Because the ISPH pressure field is independent of density, which leads to the specified pressure at open boundary, is possible.

Ferrand et al. (2017) proposed a method that deals with open boundary conditions using the semi-analysis scheme with Riemann solver. By using this method, it is possible to implement both Dirichlet and Neumann conditions at open boundaries without experiencing a spurious shock wave during the fluid particle enter/leave the system. This method requires to calculate the analytical value of renomrlization factor γ to avoid fluid particles to penetrate walls. Mayrhofer et al. (2015b) proposed a method to calculate the γ based on the integral of the Wendland kernel over a triangular element, which leads to 8 triangle / sphere intersection domain decomposition algorithms, which requires more computational resource. The only exception is the plane / sphere intersection case that then the γ can be computed easily. **Therefore, this dissertation proposes an open boundary condition that based on the semi-analytical method, this method only needs to calculate the plane / sphere intersection case, and coupling with the dummy boundary particle method to deal with the complex at open boundary geometry.** The detail of this method will be presented in chapter 3.

2.10 Interaction Between Solid and Solid

Discrete lement Method is one of the most commonly used numerical methods for tracking particle trajectories in a system and have been applied to a wide range of application such as granular flows, rock mechanics, and powder mechanics (J.A.C. et al., 1992, P.A. and O.D.L., 1979, P.K. and B.T., 1986, Walton and Braun, 1986). In DEM, each solid object is considered as an individual entity, and the motion of the object depends on its own

velocity, which is dominated by the force model. And according to Kruggel-Emden et al. (2008), the DEM method is capable of ensuring computational efficiency for contact detection and force calculation of complex shapes by using the multi-shpere method (i.e. an object with complex shape represented by multiple spherical particles).

Both SPH and DEM are Lagrangian frames, so the coupling between these two approaches is straightforward. Therefore, the most common method to deal with the interaction between solids and solids in SPH is by coupling with DEM.

The most common way of coupling DEM with SPH is by applying the dummy particle methods on DEM object (Canelas et al., 2013, 2016, Potapov et al., 2001, Ren et al., 2013, 2015, Sarfaraz and Pak, 2017, Sun et al., 2013, Wu et al., 2016). In this method, the dummy particles are filled inside the surface of DEM object/particle, and these dummy particles serve as intermediate to exert the hydrodynamic force on the DEM object.

Potapov et al. (2001) is the first one, who developed the SPH-DEM model. In their model, the no-slip condition is implemented in the surface of DEM object. The velocity of dummy particle boundary is interpolated through the nearby fluid particles and the surface of the DEM object, while the density stays unchanged. Canelas et al. (2013) uses a similar scheme, but allows the density of dummy particle boundary to evolve during the simulation to achieve higher accuracy. Ren et al. (2013) applied Riemann solver to address the interaction force between solid and fluid phase to increase the accuracy.

In Sun et al. (2013), DEM and SPH are coupled by using local averaging technique. They develop a variational approach model to ensure conservative momentum exchange between DEM-SPH. The dummy particle boundary might cause SPH suffer from abnormally high density gradients Gómez-Gesteira et al. (2005). Therefore, Ren et al. (2015) used density buffers from

mean densities of fluid particles to eliminate high density gradient problems. Wu et al. (2016) uses bonded DEM particles to study deformation and failure of the structure. In their model, the DEM particle's position evolved according to the hydrodynamic force. Where the bonded particle can be separated when the force exceeds the limit. Their model successfully captures the deformation and failure of the structure due to the hydrodynamic force. Robb et al. (2016) use SPH-DEM model to capture the accumulation of spherical ice particles at river channel due to cylindrical piles.

Based on Canelas et al. (2013)'s work, Sarfaraz and Pak (2017) presented a SPH polyhedral DEM scheme to investigate the hydraulic stability of rock and concrete blocks. Nassauer et al. (2016) proposed a model that couples SPH with polyhedral DEM particles. In this model, the repulsive force boundary treatment is applied on the DEM polyhedral object. And the position of the boundary particles of the DEM particles is varied based on the relative position of the SPH particle that is inside the DEM particle's support domain.

Robinson and Ramaioli (2011) develop a mesoscale SPH-DEM model, which uses an unresolved fluid model based on the locally averaged Navier Stokes equations. In their model the fluid particle of SPH can be larger than the DEM particles, which is very useful for solving problems such as fluidized bed that the granular particle in the system is too small to fully discretized with dummy particle method. Robinson et al. (2014) based on Robinson and Ramaioli (2011)'s model, developed a mesoscale multiphase SPH-DEM model, which successfully reproduce sedimentation of a homogeneous porous block and an inhomogeneous Rayleigh Taylor Instability.

Although DEM is suitable for obtain the collision force between two complex shapes, which are the floating body in the current work, from author's knowledge, it is still challenge to accuracy predict the deformation of the structure due to the impact of floating bodies. While the FEM has been

widely applied to study the deformation of the materials due to the collision. For example, Carlebur (1995) has carried out a series of experiments of full-scale collision between two ships, in which the bow of the rigid striking ship hitting and penetrating the side of deformable struck ship, and the finite element program MSC/DYNA is used to reproduce the collision process, and the numerical results are compared with the experimental results in terms of maximum penetration depth and contact force. Haris and Amdahl (2012) use FEA software LS-DYNA to simulate the scenario of the collision between a rigid striking bow and a ductile ship side structure. And they presented a new formula to determine the force of shell plating loaded by the general shape of a striking bow. And as stated by Kitamura (2002), the FEM is the most powerful approach to study the collision to the hull structures at present.

2.11 Summary

The traditional methods for determining flood forces, as described in section 2.1, have multiple drawbacks on solving the impact of floating bodies on the structure. Which including the traditional method is limited to solving the impact between simple geometry of both floating bodies, difficult to predict the impact of the flows on the structures during flooding, not able to capture the trajectory of the floating body during flooding and interaction between floating body and fluid and not able to predict the flow. Meanwhile, numerical approaches have been widely applied to the aforementioned difficulties that traditional method encountered. However, as mentioned in this section, there is not a single numerical method that is suitable to solve all the physics of the impact of floating bodies on buildings and structures during flooding. The SPH apparently has its advantage of treating free surface flow and solving interaction between floating bodies and flow. At meanwhile, the DEM is suitable for solving the collision between floating bodies and structure and tracking the dynamics of floating bodies. While the FEM has its advantage in solving deformation of structure due to the impact of floating bodies and flood loads. Therefore, in the current work an SPH-DEM

model is presented to solve the impact of floating bodies on buildings and structures during flooding. And FEM is applied to analysis the deformation of the structure due to the impact. Fig. 2.5 shows the current coupling framework of the SPH-DEM-FEM coupling model.

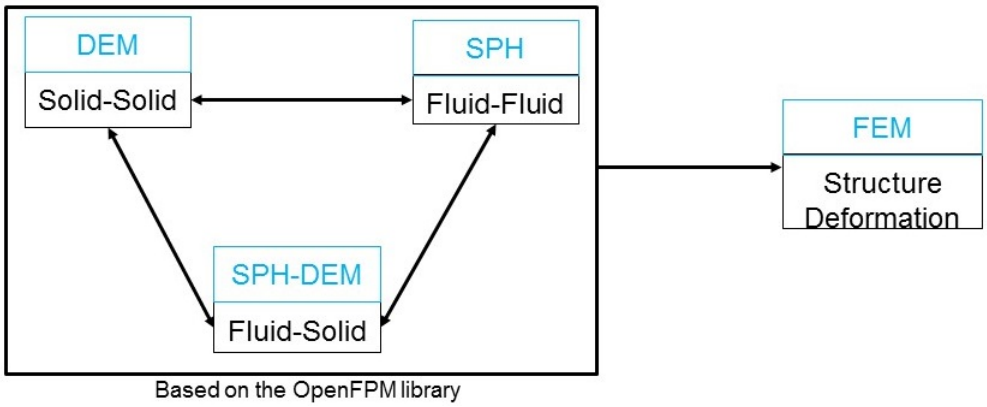

FIGURE 2.6: The current framework of the numerical model.

Chapter 3

Numerical model

3.1 Overview

This section describes the formulation of WCSPH that the fluid is considered as weakly compressible flow, the boundary conditions, the implementation of rigid bodies in SPH, the SPH coupling with DEM and the time integration scheme.

3.2 SPH Basic Formulation

3.2.1 Governing Equation of Weakly Compressible Flow

The continuity equation and momentum equation in Lagrangian form are as follows:

The continuity equation:

$$\frac{D\rho}{Dt} = -\rho \nabla \cdot \mathbf{v} \tag{3.1}$$

where $\rho, t, \mathbf{v}$ denote density, time and velocity.

The momentum equation:

$$\rho \frac{D\mathbf{v}}{Dt} = \nabla \boldsymbol{\sigma} + \mathbf{F_B} \tag{3.2}$$

where σ and $\mathbf{F_B}$ denotes stress tensor and body force. The body force in this thesis is $\rho\mathbf{g}$, where $\mathbf{g}$ denotes gravity. The stress tensor is defined as follows:

$$\sigma = -P\mathbf{I} + \eta\{-\frac{2}{3}(\nabla \cdot \mathbf{v})\mathbf{I} + (\nabla\mathbf{v} + \nabla\mathbf{v}^T)\} \tag{3.3}$$

where P is pressure, I is identity tensor and η is dynamic viscosity. In WC-SPH, the pressure is calculated by using the equation of state. The most common choice of equation of state is Tait's equation of state that a small change in density can cause a great variation in pressure. The Tait's equation of state, according to Macdonald (1966), is given as:

$$P = \frac{\rho_0 c_0^2}{\gamma}[(\frac{\rho}{\rho_0})^\gamma - 1] \tag{3.4}$$

where ρ_0, c_0 and γ denote the reference density, the reference speed and the polytropic constant, respectively. For water, it is common to set the reference density $\rho_0 = 1000kg/m^3$ and polytropic constant $\gamma = 7$. The speed of sound c_0 plays an important role in determining the compressibility of the fluid. However, based on the Courant-Fredrich-Levy(CFL) condition, when choosing the actual value of the speed of sound as reference speed (the maximum expected flow speed), the time step becomes very small and increase computational cost. Monaghan (1994) recommends that the reference speed can be set to 10 times the maximum velocity fluid, which limits the density fluctuation less than 1% and allows the SPH to take larger time step. The mathematical expression of the choice of the sound speed is given by

$$max(\frac{V_{max}^2}{c_0^2}, \frac{\mathbf{g}H}{c_0^2}) < 0.01 \tag{3.5}$$

where V_{max} is the maximum velocity of the entire system and H is the maximum height of fluid.

3.2.2 Kernel Approximation

The kernel approximation of SPH is based on the integration of an identity function $f(x)$,

$$f(x) = \int_{\Omega} f(x')\delta(x - x')dx' \tag{3.6}$$

where f is a function based on the position vector x, while x' denotes the material positions in the compact supported domain and $\delta(x - x')$ denotes the Dirac delta function, which is given by

$$\delta(x - x') = \begin{cases} 1 & x = x' \\ 0 & x \neq x' \end{cases} \tag{3.7}$$

Replacing the Dirac delta function with a smoothing kernel function, W, the equation 3.6 can be written as

$$f(x) \approx < f(x) > \doteq \int_{\Omega} f(x')W(x - x', h)dx' \tag{3.8}$$

where angle bracket $<>$ is conventional notation of kernel approximation operator in SPH literature and h is kernel length.

By applying Taylor series, the Eq. 3.8 becomes

$$\begin{aligned} < f(x) > &= \int_{\Omega} [f(x) + f'(x)(x' - x) + r((x' - x)^2)]W(x - x', h)dx' \\ &= f(x) \int_{\Omega} W(x - x', h)dx' \\ &+ f'(x) \int_{\Omega} (x' - x)W(x - x', h)dx' + r(h^2) \end{aligned} \tag{3.9}$$

If W is chosen to be an even function with respect to x, it is straightforward to obtain

$$\int_{\Omega} (x' - x)W(x - x', h)dx' = 0 \tag{3.10}$$

By applying Eq. 3.8 and 3.10 into Eq. 3.9, Eq. 3.9 becomes

$$< f(x) >= f(x) + r(h^2) \tag{3.11}$$

Eq. 3.11 showing that the integral representation of a function based on kernel approximation is a second order accuracy in SPH method.
Based on the same method, the gradient of $f(x)$ in the support domain can be written as

$$\nabla f(x) \approx < \nabla f(x) > = \int_{\Omega} \nabla f(x') W(x - x', h) dx' \tag{3.12}$$

By applying integration by parts, the Eq. 3.12 can be rewritten as

$$\nabla f(x) \approx \int_{S} f(x') W(x - x', h) n dS - \int_{\Omega} f(x') \nabla W(x - x', h) dx' \tag{3.13}$$

where S is the surface of the domain Ω. If the kernel function W is a compact function, which its value equal to zero at the S, then Eq. 3.13 can be simplified as follows

$$\nabla f(x) \approx - \int_{\Omega} f(x') \nabla W(x - x', h) dx' \tag{3.14}$$

By applying the same method, the approximation of $\nabla \cdot f(x)$ can be obtained as follows

$$\nabla \cdot f(x) \approx < \nabla \cdot f(x) > = \int_{\Omega} f(x') \cdot \nabla W(x - x', h) dx' \tag{3.15}$$

In SPH, the entire system is discritized by a finite number of particles that carry physics quantities and occupy individual space. According to particle approximation method suggested by Liu and Liu (2003), x and x' are replaced finite point x_a and x_b, and the continuous integration above can be converted to the particle approximation integration form as follows:

$$\begin{aligned} f(x_a) &= \sum_b f(x_b) W(x_a - x_b, h) V_b \\ \nabla f(x_a) &= \sum_b f(x_b) \nabla W(x_a - x_b, h) V_b \\ \nabla \cdot f(x_a) &= \sum_b f(x_b) \cdot \nabla W(x_a - x_b, h) V_b \end{aligned} \tag{3.16}$$

where a represents the concerned particle and b is a particle in the support domain of particle a. V is the volume of the particle which can be calculated

by $V = m/\rho$.

The SPH operator in Eq. 3.16 can be directly applied to obtain the governing equation in SPH form. However, Monaghan, J. (1992) suggests that the SPH operator that is the derivative of the alternative terms of ∇f, such as $\rho[\nabla \cdot (\frac{f(x)}{\rho}) + \frac{f(x)}{\rho^2} \cdot \nabla\rho]$, can conserve the linear and angular momentum if the kernel length is a constant or a symmetric function of a and b. Therefore, it is preferable to use an alternative term of ∇f to construct SPH operator. By using the alternative forms of ∇f and method mention above to obtain the SPH operator (Eq. 3.16), the most common form of SPH operator in the SPH community can be obtained as follows:

$$\begin{aligned} Grad_a A_b &\equiv \rho_a \sum_{b \in F} m_b (\frac{A_a}{\rho_a^2} + \frac{A_b}{\rho_b^2}) \nabla w_{ab} \\ Div_a A_b &\equiv -\frac{1}{\rho_a} \sum_{b \in F} m_b (A_{ab}) \cdot \nabla w_{ab} \end{aligned} \tag{3.17}$$

Eq. 3.17 is a general form of the SPH operator that is most often used in weakly compressible SPH method in literature. Where $Grad_a$ and Div_a stand for gradient operator and divergence operator, respectively. Since Laplacian operator $\triangle f$ is equal to $\nabla \cdot \nabla f$, the SPH Laplacian operator Lap_a can be defined as

$$Lap_a(B_b, A_b) \equiv \rho_a \sum_{b \in F} m_b \frac{B_b + B_a}{\rho_a \rho_b} \frac{A_{ab}}{r_{ab}^2} r_{ab} \cdot \nabla w_{ab} \tag{3.18}$$

3.2.3 Kernel Choice

Liu and Liu (2003) suggests that a kernel function suitable for SPH should satisfy the following conditions.

$$\begin{aligned}
\text{Unity} &: \int_{\Omega} W(x-x',h)dx' = 1 \\
\text{Compactly support} &: W(x-x') = 0, \quad for \quad |x-x'| > \kappa h \\
\text{Positive} &: W(x-x') \geq 0, \text{when} \quad x' \quad \text{inside} \quad \Omega \\
\text{Delta function properties} &: \lim_{x\to\infty} W(x-x',h) = \delta(x-x') \\
\text{Normalization} &: \int_{\Omega} W(x-x')dx' = 1 \\
\text{Decay} &: W(x-x') - W(x-x") > 0 \\
&, \quad \text{when} \quad |x-x'| < |x-x"|
\end{aligned} \tag{3.19}$$

Any function that meets the requirement mentioned above can be used as kernel function. Several different kernel functions, including Gaussian kernel, B-spline and Wendland kernels, have been widely employed in the different SPH application. Mayrhofer et al. (2015b) suggests that when the semi-analytical method is employed for dealing with boundary, the truncation error of calculating $\nabla\gamma$ and γ (the renormalized factor) numerically may cause fluid particles to penetrate the boundary. Thus, they suggest to calculate $\nabla\gamma$ and γ analytically when the semi-analytical method is employed. The analytical $\nabla\gamma$ and γ can be calculated by integrating the kernel function over the boundary, which appears in a fluid particle's support domain. However, as appendix A shows, it is impossible to obtain an analytical function to calculate γ when Gaussian kernel is chosen. And analytical function for calculating γ and $\nabla\gamma$ constructed by using piecewise polynomial functions are over complicated to implement. Therefore, the only choice for the kernel function from the literature is Wendland kernel.

The Wendland kernel meets all the requirements of SPH kernel function. Besides that, Dehnen and Aly (2012), Macia Lang et al. (2011) mentioned that when using Wendland kernel function to construct SPH governing equation, the problem of paired instability of particle clustering in the simulation process can be avoided. Moreover, the Wendland kernel is considered as the best balance between accuracy and computational cost (Panizzo et al., 2007). Most importantly, it is suitable to derive the function to calculate $\nabla\gamma$ and γ analytically.
Therefore, the Wendland kernel is used exclusively to construct all the work in this thesis. The Wendland kernel can be written as

$$W(x-x',h) = \begin{cases} \alpha_d(2q+1)(1-\frac{q}{2})^4, & 0 \leq q \leq 2 \\ 0, & else \end{cases} \tag{3.20}$$

Its derivative is

$$\nabla W(x-x',h) = \begin{cases} \frac{\alpha_d}{h}(-5q(1-\frac{q}{2})^3), & 0 \leq q \leq 2 \\ 0, & else \end{cases} \tag{3.21}$$

where $\alpha_d = \frac{7}{4\pi}$ in two dimensional and $\alpha_d = \frac{21}{16\pi}$ in three dimensional and d denotes the dimension of system. And h is the smoothing length, while q is a dimensionless value which is defined as:

$$q = \frac{x-x'}{h} \tag{3.22}$$

The smoothing length is chosen based on the default distance of particles Δx as:

$$h = w_h \delta x \tag{3.23}$$

w_h is a value that will affect the radius of the support domain. Commonly, it is chosen as $w_h = 1.3$, which respectively gives 21 neighboring particles in 2D and 71 neighboring particles in 3D. This value is considered as best value balancing number of interacting particles and the computational cost.

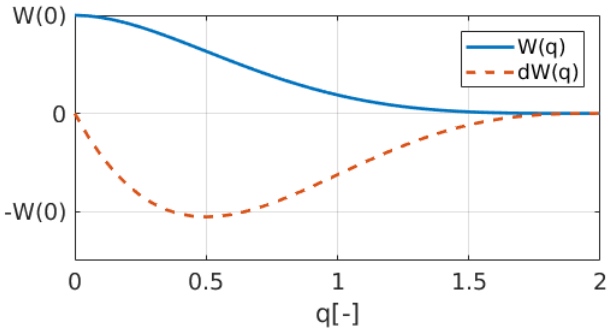

FIGURE 3.1: Values of the Wendland kernel and its derivative divided by α_d and $\frac{\alpha_d}{h}$ respectively.

3.2.4 Governing Equation in SPH Form

By applying SPH operator in Eq. 3.16 and Eq. 3.17 to governing equation 3.1 and 3.2, the governing equation in SPH form can be obtained as follows

$$\begin{aligned} \frac{D\rho_a}{Dt} &= -\rho_a Div_a(u_b) \\ \frac{Du_a}{Dt} &= -\frac{1}{\rho_a} Grad_a(P_b) + \frac{1}{\rho_a} Lap_a(\mu_b, u_b) + g \end{aligned} \tag{3.24a}$$

which can be written as

$$\begin{aligned} \frac{D\rho_a}{Dt} &= \sum_{b\in F} m_b(u_a - u_b)\cdot\nabla w_{ab} \\ \frac{Du_a}{Dt} &= -\sum_{b\in F} m_b(\frac{P_a}{\rho_a^2} + \frac{P_b}{\rho_b^2})\nabla w_{ab} + \sum_{b\in F} m_b(\frac{\mu_a + \mu_b}{\rho_a\rho_b})\frac{u_{ab}}{r_{ab}^2}\cdot\nabla w_{ab} + g \end{aligned} \tag{3.24b}$$

Eq. 3.24(a) is the most commonly used form of the governing equation of the weakly compressible SPH model, in which the density of particles is based on the velocity difference between current particle and its neighboring particles. The acceleration of particle a is dominated by the pressure of particle a and its neighboring particle b.

3.3 Boundary Condition

The boundary conditions in SPH consisted of the free surface boundary condition and the solid wall boundary condition. The free surface boundary condition has to satisfy both free surface kinetic boundary condition (FSKBC) and free surface dynamic boundary condition (FSDBC). The FSKBC is the boundary condition of free surface movement of the flow. The velocity of fluid particles at the free surface is equal to the velocity of the free surface. And the FSDBC is the dynamic boundary condition of free surface, means that the pressure of fluid particles at the free surface is equal to the atmospheric pressure.

According to Colagrossi et al. (2009) and Violeau and Rogers (2016), due to the Lagrangian nature, the FSKBC can be satisfied without additional treatment in WCSPH, the particles at free surface always remain at free surface. While for FSDBC, due to lack of particles above the free surface, the pressure at free surface is automatically set to zero by the equation of state in WCSPH framework. Consequently, the WCSPH does not require any additional free surface boundary conditions.
The dummy particles method is one of the most robust boundary treatment in WCSPH framework. In this method, three to four layers of fictitious particles are deployed outside of the fluid domain and adjacent to a solid boundary as shown in Fig. 3.1. These fictitious particles are called dummy particles, and their position evolves according to the motion of the wall boundary. The physical properties of these dummy particles do not evolve according to time, but interpolate through the fluid particles that is inside their support domain. Following (Adami et al., 2012, Sun et al., 2015b), the pressure of the dummy particles can be calculated as follows,

$$P_w = \frac{\sum_F P_F W_{wF} - \sum_F (\rho_F \mathbf{g} + \mathbf{F_v} - \rho_F \mathbf{a_w}) \cdot \mathbf{x_{wF}} W_{wF}}{\sum_F W_{wF}} \tag{3.25}$$

where $(.)_w$ and $(.)_F$ denotes the dummy particle and fluid particle respectively, while a_w denotes the acceleration of the dummy particle. For the velocity assigned to dummy particles, the method proposed by Sun et al.

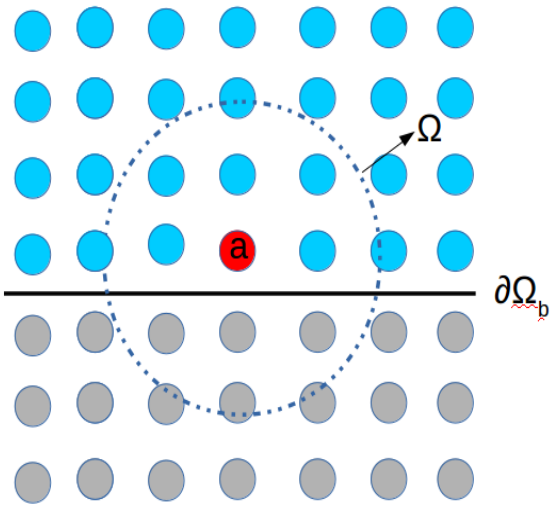

FIGURE 3.2: Illustration of dummy particles boundary conditions that the full kernel support Ω is filled even with the presence of the boundary $\delta\Omega_b$.

(2015b) is applied as follows:

$$\begin{cases} free-slip: & u_F - u_w = 0 \\ no-slip: & \begin{cases} u_w \cdot n_s = u_{ext} \cdot n_s \\ u_w \cdot t_s = (2u_B - u_{ext}) \cdot t_s \end{cases} \end{cases} \tag{3.26}$$

where the u_{ext} is defined as

$$u_{ext} = \frac{\sum_F u_F W_{wF}}{\sum_F W_{wF}} \tag{3.27}$$

and n_s and t_s is the normal direction and the tangential direction on the solid boundary surface. u_B is the velocity of solid boundary.

3.4 Open Boundary Condition

When it comes to the large-scale flow simulation, the open boundary condition becomes necessary. The simplest way to deal with open boundary condition in SPH is by using buffer layers method developed by Vacondio

(2012). However, as explained by Vacondio (2012), this method might create the spurious shock when the buffer particles suddenly turns into fluid particle during simulation. Moreover, this method is not capable to treat the inlet when the flow direction is not parallel to the normal of the inlet boundary. Another method to deal with open condition is the Semi-analytical method proposed by Ferrand et al. (2017), Leroy et al. (2014), M.Ferrand et al. (2011). In this method, Eulerian particles evolve at the open boundaries. And the mass of these Eulerian particle is evolving based on the inflow/outflow condition applied at the open boundaries. When the mass of Eulerian particles is above over the assigned threshold, then a fluid particle is released at the location of the Eulerian particle. When an outgoing fluid particle exit from a fluid domain, it is dispatched over the Eulrerian particles. This method can avoid the spurious wave problem and allows treatment of open boundaries in a unified way. Therefore, in order to treat the open boundary, the semi-analytical method is employed.

3.4.1 Semi-analytical Method

The boundary of a three dimensional geometry is two dimensional. And the most basic bounded two dimensional element is the triangular element. Therefore, the boundary element of semi-analytical method in 3D in this work is triangular element. In the Semi-analytical method, boundaries are discretized by a set of vertex particles v where the properties of the vertices is denoted by $(.)_v$. The vertex are connected to boundary segments s and connected by three vertex particles as Fig. 3.3 (a) shows, where the properties of the segments is denoted by $(.)_s$. An additional field variable γ is introduced to address the boundary term. The γ refers to the part of kernel support that is inside the support domain as shown in Fig. 3.3b, and is defined as:

$$\gamma_a \equiv \int_{\Omega_a \cap \Omega} w(r_a - r)dr \tag{3.28}$$

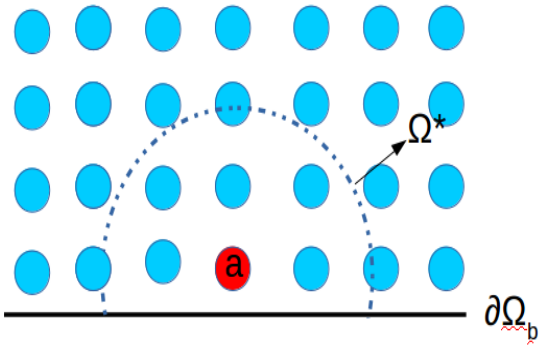

FIGURE 3.3: Illustration of semi-analytical boundary condition with truncated kernel support domain Ω^* with presence of the boundary $\delta\Omega_b$.

The gradient of γ_a is given by:

$$\nabla\gamma_a \equiv \left(\int_s w(r)dS\right)n_s \tag{3.29}$$

Following (Mayrhofer et al., 2015b), when the support domain of a fluid particle intersects a flat wall in 3D, its analytical value of γ_a and $\nabla\gamma_a$ can be calculated as

$$\begin{aligned}\gamma_a &= 1 - \frac{1}{512}(2-d)^6(4+6d+3d^2)\\ \nabla\gamma_a &= \alpha_d\frac{2}{7}\pi(2+5d+4d^2)(1-\frac{d}{2})^5 n_s\end{aligned} \tag{3.30}$$

where d is the distance between the particle and wall and n_s is the surface normal vector that points inwards from the domain. It is worth noting that the above formula is derived from the Wendland kernel and applies only to applications that use the Wendland kernel. When the Semi-analytical method is introduced, the SPH operator in Eq. 3.16 and 3.17 have to be modified as follows

$$\begin{aligned}Grad_a^{\gamma}(A_b) \equiv \frac{\rho_a}{\gamma_a}\sum_{b\in F} m_b(\frac{A_a}{\rho_a^2}+\frac{A_b}{\rho_b^2})\nabla w_{ab}\\ -\frac{\rho_a}{\gamma_a}\sum_{s\in\delta}(\frac{A_a}{\rho_a^2}+\frac{A_s}{\rho_s^2})\rho_s\nabla\gamma_{as}\end{aligned}$$

$$
\begin{aligned}
Div_a^{\gamma}(A_b) \equiv & -\frac{1}{\rho_a \gamma_a} \sum_{b \in F} m_b (A_{ab}) \cdot \nabla w_{ab} \\
& + \frac{1}{\gamma_a} \sum_{s \in \delta} u_{as} \cdot \nabla \gamma_{as} \qquad (3.31) \\
Lap_a^{\gamma}(B_b, A_b) \equiv & \frac{\rho_a}{\gamma_a} \sum_{b \in F} m_b \frac{2 B_a B_b}{B_a + B_b} \frac{A_{ab}}{r_{ab}^2} r_{ab} \cdot \nabla w_{ab} \\
& - \frac{1}{\gamma_a} \sum_{s \in \delta} (B_s \nabla A_s + B_a \nabla A_a) \cdot \nabla \gamma_{as} \qquad \textit{dotted}
\end{aligned}
$$

As explained by Leroy et al. (2014), M.Ferrand et al. (2011) and Ferrand et al. (2017), the two boundary terms $(B_s \nabla A_s + B_a \nabla A_a)$ in the Laplacian operator of Eq. 3.31 is the flux at the boundary. As the current approach is the first order approximation, the two boundary terms can be replaced by $2|\nabla \gamma_{as}| B_s \nabla A_s \cdot n_s$ when a Neumann boundary condition is imposed. And when a Dirichlet condition is imposed, the two boundary terms can be replaced by $-2|\nabla \gamma_{as}| \frac{2 B_a B_s}{B_a + B_s} / (r_{as} \cdot n_s)$.

The governing equation of the current SPH model will become

$$
\begin{aligned}
\frac{D \rho_a}{D t} &= -\rho_a Div_a^{\gamma_a}(u_b) \\
\frac{D u_a}{D t} &= -\frac{1}{\rho_a} Grad_a^{\gamma_a}(P_b) + \frac{1}{\rho_a} Lap_a^{\gamma_a}(\mu_b, u_b) + g
\end{aligned} \qquad (3.32)
$$

By using the divergence-operator definition, the continuity equation of Eq. 3.32 can be rewritten as

$$
d\rho_a = \frac{1}{\gamma_a} \sum_{b \in P} m_b \nabla w_{ab} \cdot u_{ab} dt - \frac{\rho_a}{\gamma_a} \sum_{s \in \delta} \nabla \gamma_{as} \cdot u_{as} dt \qquad (3.33)
$$

However, the above continuity equation does not consider the situation that is at the open boundary, the particle velocity $v_a = \frac{dr}{dt}$ (i.e. the Lagrangian derivative of the position) and fluid velocity u_a (i.e. the velocity field at position r_a) are not equivalent. This leads to density errors and spurious shock waves when particles are produced or deleted on the open boundary. Therefore, to stop introducing errors on the density at each time step, it is

necessary to rewrite the Eq. 3.33 as:

$$\begin{aligned} d\rho_a = & \frac{1}{\gamma_a}\sum_{b\in P} m_b \nabla w_{ab}\cdot u_{ab} dt \\ & - \frac{1}{\gamma_a}\sum_{v\in V^{i/o}} m_v \nabla w_{av}\cdot (u_v - v_v) dt \\ & - \frac{\rho_a}{\gamma_a}\sum_{s\in\delta} \nabla\gamma_{as}\cdot u_{as} dt \\ & + \frac{\rho_a}{\gamma_a}\sum_{s\in\delta^{i/o}} \nabla\gamma\cdot (u_s - v_s) dt. \end{aligned} \tag{3.34}$$

where the vertex and segments belong to the open boundaries are denoted by $v^{i/o}$ and $\delta^{i/o}$, respectively. $(.)_P$ denotes both fluid and solid particles. Following (Ferrand et al., 2017), the time integration of the continuity equation above gives us:

$$\begin{aligned} \rho_a^{n+1} = & \frac{1}{\gamma_a^{n+1}}\gamma_a^n \rho_a^n + \sum_{b\in P^n} m_b^n (W_{ab}^{n+1} - W_{ab}^n) \\ & + \sum_{v\in V^{i/o}} m_v^n [W_{av}^n - W(r_{av}^n + \delta r_v^{i/o})] \\ & + \frac{\rho_a^n}{2}\sum_{s\in\delta^{i/o}} [\nabla\gamma_{as}(r_{as}^n + \delta r_s^{i/o}) + \nabla\gamma_{as}(r_{as}^n)]\cdot \delta r_s^{i/o} \end{aligned} \tag{3.35}$$

where $\delta r_v^{i/o} \equiv \triangle t(u_v - v_v)$ and $\delta r_s^{i/o} \equiv \triangle t(u_s - v_s)$. The velocity of triangle segments above is defined by $u_s = (u_{v1} + u_{v2} + u_{v3})/3$, where u_{v1}, u_{v2} and u_{v3} denote the three connected vertices of a triangular segments s as Fig. 3.3 (b) shows.

3.4.2 Update Mass of Vertex

To ensure the mass change smoothly, the mass of vertex particles at the open boundaries is calculated according to desired mass fluxes through the open boundary $\dot{m}_v$, which can be calculated through the mass fluxes of the connected segment s. When a vertex is connected with triangle elements at

the open boundaries, the mass changed of the vertex can be calculated as:

$$\dot{m_v} = \frac{1}{3} \sum_{s \in N_{sv}^{i/o}} \rho_s A_s (u_s - v_s) \cdot n_s \text{ for v} \in V^{i/o} \tag{3.36}$$

where $N_{sv}^{i/o}$ is the segments that connoted with the concerned vertex V, while A_s is the area of the triangular segment. And the mass of the vertex at the open boundaries are updated according to

$$m_v^{n+1} = m_v^n + \triangle t \dot{m_v}^n \tag{3.37}$$

For the inlet boundary, when the mass of a vertex on open boundaries reaches the threshold value $\theta_v m_{ref}$, then a fluid particle is created and released on the position of the vertex. And at mean time, the mass of the created fluid particle is subtracted from the vertex on open boundaries. Where θ_v is defined as the open angle of the vertex divided by 2π, which is 0.5 for a plane boundary, and m_{ref} is the mass of a fluid particle. In the outlet case, when a fluid particle passes through the outlet boundary segment, the fluid particle is removed and its mass is dispatched to the vertex connected to the segments by a weight $\beta_{a,v}$. Following (Leroy et al., 2016), the weight $\beta_{a,v}$ is given as:

$$\begin{aligned}
\beta_{a,v_0} &= \frac{0.5[P_2 \times r_{v_2 v_1}] \cdot n_s}{0.5[r_{v_0 v_1} \times r_{v_0 v_2}] \cdot n_s} \\
\beta_{a,v_1} &= \frac{0.5[P_0 \times r_{v_0 v_2}] \cdot n_s}{0.5[r_{v_0 v_1} \times r_{v_0 v_2}] \cdot n_s} \\
\beta_{a,v_2} &= \frac{0.5[P_1 \times r_{v_1 v_0}] \cdot n_s}{0.5[r_{v_0 v_1} \times r_{v_0 v_2}] \cdot n_s}
\end{aligned} \tag{3.38}$$

where P_i is the projection vector of r_{av_i}, while r_{ab} is defined as the vector from particle a to particle b. The masses of vertex particles at the open boundaries are updated as:

$$m_v^{n+1} = m_v^n + \triangle t \dot{m_v}^n + \delta m_v^n \text{ for } v \in V^{i/o} \tag{3.39}$$

where δm_v is the mass variation due to the created/removed fluid particles. It is worth to mention that, in order to keep the mass conservation during

a time step, Eq. 3.38 is added to the end of each time step.

3.4.3 Imposing Pressure and Velocity

At the open boundaries, either pressure or velocity is given. The quantity that is not given required to be computed by using Riemann invariants. As WSPH is adopted, the boundary conditions can be derived by using linearized Riemann problem. Since WCSPH is barotropic fluid and the chosen reference speed of sound is significantly larger than the flow velocity, it is suitable to adopt the approach proposed by Blondel et al. (2013).

3.4.3.1 Imposing Velocity

When the Neumann velocity condition is imposed on open boundary, the given velocity is directly assigned to the vertex while the velocity of segments is calculated from the connected vertex as follows:

$$u_s = \frac{1}{N_{vs}} \sum_{v \in N_{vs}} u_v \tag{3.40}$$

where N_{vs} is the number of connected vertices, for a triangular segment $N_{vs} = 3$. This value will be set to the velocity of external state that $u_{ext} = u_s$. Where $(.)_{ext}$ and $(.)_{int}$ denotes the external and the internal state of the quantity at the open boundary. The velocity of the internal state is extrapolated as:

$$u_{int} = \frac{1}{\alpha_s} \sum_{b \in F} V_b u_b w_{bs} \tag{3.41}$$

where a_s is defined by :

$$\alpha_s = \sum_{b \in F} V_b w_{bs} \tag{3.42}$$

Similarly, the pressure of the internal state is extrapolated as:

$$\begin{aligned} P_{int} &= \frac{1}{\alpha_s}\sum_{b\in F} V_b P_b w_{bs} \\ \rho_{int} &= EOS^{-1}(P_{int}) = \rho_0(P_{int}\frac{\gamma}{\rho_0 C_0^2}+1)^{\frac{1}{\gamma}} \end{aligned} \tag{3.43}$$

where EOS is the equation of state defined by Eq. 3.4.

To calculate the external state of pressure P_{ext}, it is necessary to consider that there is an interface between internal state and external state of the open boundary. Based on the discontinuity between two states and assumption of the 1D problem of open boundary, the Riemann problem is employed to find the external state of pressure. The solution can be divided into three possible types of discontinuity, which are expansion wave, shock wave and contact wave. The external state of pressure, according to the three states, can be calculated as follows:

$$\begin{aligned} Expansion\ wave &: \rho_{ext,e} = \psi^{-1}(\psi(\rho_{int}) + u_{ext} - u_{int}) \\ Shock\ wave &: \rho_{ext,s} = EOS^{-1}(P_{int} + \rho_{int}u_{int}(u_{int} - u_{ext})) \\ Contact\ discontinuity &: \rho_{ext,c} = \rho_{int} \end{aligned} \tag{3.44}$$

where ψ is defined as:

$$\begin{aligned} \psi(\rho) &= \frac{2c_0}{\zeta-1}(\frac{\rho}{\rho_0})^{\frac{\zeta-1}{2}} \quad for \quad \zeta > 1 \\ \psi(\rho) &= c_0 ln(\frac{\rho}{\rho_0}) \quad for \quad \zeta = 1 \end{aligned} \tag{3.45}$$

after finding all three external states of pressure. The proper external pressure is chosen by using following relations:

$$\begin{aligned} Expansion\ wave: &\quad u_{ext} + c(\rho_{ext,e}) \le u_{int} + c(\rho_{int}) \\ Shock\ wave: &\quad u_{ext} + c(\rho_{ext,s}) > u_{int} + c(\rho_{int}) \\ Contact\ discontinuity: &\quad u_{ext} + c(\rho_{ext,e}) > \\ &\quad u_{int} + c(\rho_{int}) \ge u_{ext} + c(\rho_{ext,s}) \end{aligned} \tag{3.46}$$

where the u_{ext} and u_{int} are calculated by using Eq. 3.40 and Eq. 3.41 respectively. The function $c(x)$ is a speed of sound as a function of density defined by

$$c(\rho) = c_0(\frac{\rho}{\rho_0})^{\frac{\zeta-1}{2}} \tag{3.47}$$

By applying Eq. 3.40 into Eq. 3.47, one can obtain the external state of pressure P_{ext}. This value then is prescribed to the pressure of segments P_s. And at the end, the pressure of a vertex is calculated by averaging the surrounding segments as:

$$P_v = \frac{1}{N_{vs}} \sum_{s \in N_{vs}} P_s \tag{3.48}$$

3.4.3.2 Imposing Pressure

The procedure to impose the pressure condition is similar to impose velocity conditions as above. However, the pressure is given, while the rest of the quantities need to be computed by using Riemann invariants. For Neumann pressure condition, the given pressure is directly prescribed to the vertex and considered as the external state of pressure $P_{ext} = P_v$. Then the pressure of the segments is computed through the connected vertex as follows:

$$P_s = \frac{1}{N_{vs}} \sum_{s \in N_{vs}} P_v \tag{3.49}$$

The velocity and pressure at internal state can be calculated as Eq. 3.41 and Eq. 3.43, while the velocity at external state is computed by

$$\begin{aligned} Expansion\ wave &: u_{ext,e} = u_{int} + \psi(\rho_{ext}) - \psi(\rho_{int}) \\ Shock\ wave &: u_{ext,s} = u_{int} + \frac{P_{int} - P_{ext}}{\rho_{int} max(u_{int}, 10^{-5} * c_0)} \\ Contact\ discontinuity &: u_{ext,c} = u_{int} \end{aligned} \tag{3.50}$$

When the three states of velocity at external state are known, the proper u_{ext} is determined by using Eq. 3.46. This value will then be prescribed to

the velocity of vertex that $u_v = u_{ext}$, and velocity of the segments at the open boundary is then computed by using Eq. 3.40.

3.5 Motion of a solid body

The motion of a solid body at a free surface can be divided into translational velocity and rotational velocity. The conservation equations of momentum and moment of momentum of the solid body are given as follows(Oger et al., 2006a),

$$\begin{aligned} \frac{DU_c}{Dt} &= \frac{F_{solid-body}}{M_c} + g \\ \frac{D\Omega_c}{Dt} &= \frac{T_{solid-body}}{I_c} \end{aligned} \tag{3.51}$$

where $F_{solid-body}$ and $T_{solid-body}$ denote the total force and torque applied to the solid body. U_c, Ω_c, M_c and I_c denote translational velocity, rotational velocity, mass, and moment of inertia from the center of gravity of the solid body. For a solid object, a boundary condition is required to avoid fluid particles penetrating the surface of the solid body. Thus, the dummy boundary particle technique mentioned in section 3.2 is applied to the solid object that a solid body is represented by a set of dummy particles inward to the solid body's surface. The resultant forces and the resultant toques applies to the solid body by the fluid particles can be calculated as follows Sun et al. (2015a):

$$\begin{aligned} F_{solid-body} &= F_{fluid-solid} \\ &= \sum_{a \in fluid} \sum_{b \in solid} -[-(V_a^2 + V_b^2)\widetilde{P_{ab}}] + F_{ab}^v \\ T_{solid-body} &= T_{fluid-solid} \\ &= \sum_{a \in fluid} \sum_{b \in solid} -(\frac{x_a + x_b}{2} - x_c) \times [-(V_a^2 + V_b^2)\widetilde{P_{ab}}] + F_{ab}^v \end{aligned} \tag{3.52}$$

where $F_{fluid-solid}$ and $T_{fluid-solid}$ denote the resultant force and resultant torque between fluid and solid body and $\widetilde{P}_{ab}$ is defined by $2P_aP_b/(P_a+P_b)$, while F^v_{ab} is the viscous force between a pair of interacting fluid particle and dummy particle. As a rigid body, the relative position between a solid body's center of gravity and those dummy boundary particles that filled inside the solid body remain unchanged during entire simulation. Therefore, the position, velocity and the acceleration of each boundary particles of the solid body are described as follows:

$$\begin{aligned} \frac{Dx}{Dt} &= u_b \\ u_b &= U_c + \Omega_c \times (x_b - x_c) \\ a_b &= \frac{DU_c}{Dt} + \frac{D\Omega_c}{Dt} \times (x_b - x_c) + \Omega_c \times (u_b - U_c) \end{aligned} \tag{3.53}$$

The velocity u_b is used for updating the position of the particles, while the acceleration a_b is used in Eq. 3.25 as the acceleration of the dummy particles.

3.6 Discrete Element Method

The above SPH formulation has addressed the fluid-solid interaction, yet the interaction between solid and solid remains unsolved. Since both SPH and DEM are Lagragian approaches, it is straight forward to couple these two methods. Therefore, in this work to prevent a solid body from penetrating or overlapping with another solid body, the DEM method is employed. In DEM, the multisphere approach is one of the most straightforward way to model a rigid body with complex shape. In this approach, the boundary surface is filled with a set of spherical subshapes as Fig. 3.4 shown. These spherical subshapes serve as medium to compute overlapping and contact force of two collide objects. In general, the multisphere DEM approach consists of following three steps:

1. Calculating the overlapping of two subshapes that belongs to two solid bodies.

2. Calculating the contact force between two solid objects based on the force model.

3. Time integration of entire system.

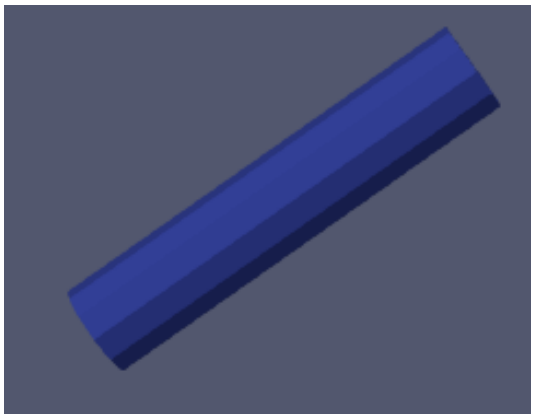

(a)

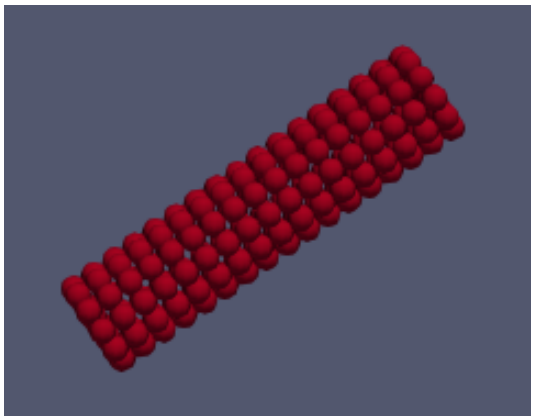

(b)

FIGURE 3.4: (a) a cylinder object with surface mesh. (b) an example of a cylinder object constructed with the multisphere method.

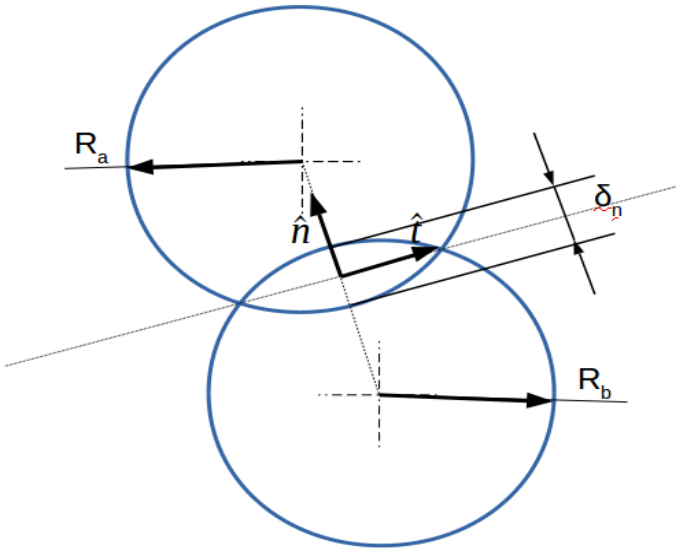

FIGURE 3.5: Contact configuration of two spherical subshapes.

In the DEM model, the contact force of two overlapping subjects can be decomposed into F_n^{DEM} and F_t^{DEM}, which is normal and tangential components respectively. In this work, the non-linear, Hertzian model (Kuwabara and Kono, 1987) is employed to determine the normal contact force as follows:

$$F_n^{DEM} = k_n \delta_n^{3/4} \hat{e} - \gamma^{DEM} \delta_n^{1/4} \dot{\delta_n} \hat{e} \tag{3.54}$$

where k_n denotes stiffness, δ_n denotes overlapping in normal direction, $\hat{e}$ denotes the unit vector between two over lapping subshapes and γ^{DEM} denotes the damping constant. The first term and second term of Eq. 3.54 is elastic term and dissipative terms, respectively. The stiffness and damping constant are defined by

$$\begin{aligned} k_n &= \frac{4}{3} E^* \sqrt{R^*}; \\ \gamma^{DEM} &= C_n \sqrt{6 M^* E^* \sqrt{R^*}}; \end{aligned} \tag{3.55}$$

where C_n is equal to 10^{-5}. The other parameters are given as follows:

$$\begin{aligned} \frac{1}{E^*} &= \frac{1-\nu_a^2}{E_a} + \frac{1-\nu_b^2}{E_b} \\ R^* &= \frac{R_a R_b}{R_a + R_b} \\ M^* &= \frac{M_a M_b}{M_a + M_b} \end{aligned} \tag{3.56}$$

where E and ν is Young modulus and Poisson ratio, respectively, while R is the radius of the spherical subshape.
Regarding tangential contacts force ${F_t}^{DEM}$, it is predicted from the static friction between two spherical subshapes and is limited by the dynamic friction force. This is given as follows:

$$F_t^{DEM} = min(static \quad friction, \quad dynamics \quad friction) \tag{3.57}$$

The static friction of the model is the viscous damping force, and the dynamic friction is based on Coulomb's law of friction. Hence, in this study, the tangential force F_t^{DEM} is given as follows

$$F_t^{DEM} = min(c_t\dot{\delta}, \mu F_n^{DEM})\hat{t} \tag{3.58}$$

where c_t and μ is the tangential damping coefficient and Coulomb's friction coefficient, respectively. $\dot{\delta}$ is the relative tangential velocity.

3.6.1 Coupling with SPH

To reduce the memory consumption and ease the difficulties of coupling, the dummy boundary particles in section 3.2 are directly used as the spherical subshpaes of DEM. When the DEM model is included, an additional contact force term has to be introduced to the Eq.3.36

$$\begin{aligned} F_{solid-body} &= F^{DEM} + F_{fluid-solid} \\ T_{solid-body} &= T^{DEM} + T_{fluid-solid} \end{aligned} \tag{3.59}$$

where F^{DEM} term denotes the total contact force computed by the DEM model while T^{DEM} term denotes the total torque computed by the DEM model. They are defined as follows.

$$\begin{aligned} F^{DEM} &= \sum_{a\in solid}\sum_{b\in solid}(F_{n_{ab}}^{DEM}+F_{t_{ab}}^{DEM}) \\ T^{DEM} &= \sum_{a\in solid}\sum_{b\in solid}(F_{n_{ab}}^{DEM}+F_{t_{ab}}^{DEM})\times(x_a-x_b) \end{aligned} \tag{3.60}$$

3.7 Time Integration

Considering that when the semi-analytical method is employed for the open boundary problem, to calculate the γ mentioned in (section 3.31) becomes most computational costly part of the program. Therefore, it is more appropriate to follow the time integral scheme suggested by Ferrand et al. (2017). That in a time step, γ only needs to be calculated once. The time integration scheme in this thesis is arranged as

$$\begin{aligned} \frac{Du_a}{Dt} &= -\frac{1}{\rho_a}Grad_a^{\gamma_a}(P_b)+\frac{1}{\rho_a}Lap_a^{\gamma_a}(\mu_b,u_b)+g \\ u_a^{n+1} &= u_a^n+\delta t\frac{Du_a}{Dt} \\ v_a^{n+1} &= u_a^{n+1} \text{ for } i\in F/V \\ r_a^{n+1} &= r_a^n+\delta t\ v_a^{n+1} \\ \gamma_a^{n+1} &= \gamma_a^n+\delta\sum_{s\in\delta}\frac{1}{2}(\nabla\gamma_a^{n+1}+\nabla\gamma_a^n)\cdot v_{as}^{n+1} \\ \rho_a^{n+1} &= \frac{1}{\gamma_a^{n+1}}\gamma_a^n\rho_a^n+\sum_{b\in P^n}m_b^n(W_{ab}^{n+1}-W_{ab}^n) \\ &\quad+\sum_{v\in V^{i/o}}m_v^n[W_{av}^n-W(r_{av}^n+\delta r_v^{i/o})] \\ &\quad+\frac{\rho_a^n}{2}\sum_{s\in\delta^{i/o}}[\nabla\gamma_{as}(r_{as}^n+\delta r_s^{i/o})+\nabla\gamma_{as}(r_{as}^n)]\cdot\delta r_s^{i/o} \end{aligned} \tag{3.61}$$

3.7.1 Constrains on Time Step

Due to the above time scheme being explicit, it is required to consider the time-step stability restrictions, which depend on the advection, diffusion and forcing terms. Following (Monaghan and Kos, 1999), a particle's time-step, Δt has to satisfy conditions as follows

$$\Delta t_a = C_{\Delta t} \quad min(\delta t_f, \delta t_{cv}) \tag{3.62}$$

where δt_f and δt_{cv} are defined as follows

$$\begin{aligned} \delta t_f &= min_b \sqrt{\frac{h}{|F_{ab}|}} \\ \delta t_{cv} &= min_a \frac{h}{c_0 + max|\frac{h(v_a - v_b)\cdot(x_a - x_b)}{|(x_a - x_b)|^2}|} \end{aligned} \tag{3.63}$$

Since semi-analytical method is employed, an additional time-step constraint related to $\nabla\gamma$ is required. Following (Ferrand et al., 2017), the additional time-step constrain is given as:

$$\Delta t \leq 0.004 \frac{1}{max_{a\in F}(max_{s\in\delta}[|\nabla\gamma_{as}\cdot(u_{as} - v_{as})|])} \tag{3.64}$$

3.8 Computation Aspects

In this work, the Wendland kernel is employed with the kernel length 1.3 times to the spacing of particles ($h = 1.3\triangle x$) that results in the cutoff radius of 2.6 times to the spacing of particles ($r_c = 2.6\triangle x$). This allows each particle, in the computational domain, to contain about $O(90)$ neighboring particles in 3D. Therefore, it is important to implement SPH using a library that can efficiently create interaction lists and calculate the rate of change in the governing equation. An open and scalable framework for particle simulations that provides all the necessary functionality, including domain decomposition, dynamic force balancing, communication abstractions transparent handling of cross-processor interactions in a parallel code

was presented by Incardona et al. (2018), Sbalzarini et al. (2006). They distributed an open source C++ library called OpenFPM, which is capable of managing scalable particle and hybrid particle-mesh simulations on distributed-memory parallel computer systems. In this thesis, the SPH code is constructed based on OpenFPM library, which allows for highly efficient SPH simulations more than millions of particles on the High Performance Cluster at University of Luxembourg (Varrette et al., 2014). The current software architecture is shown as Fig. 3.6.

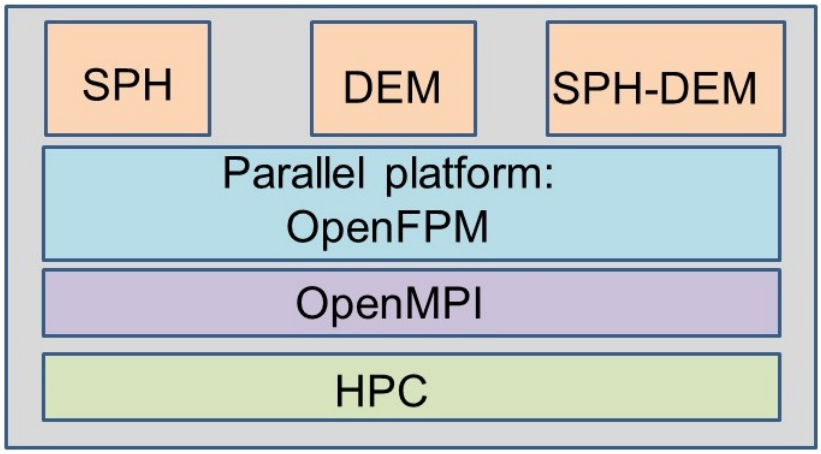

FIGURE 3.6: Software architecture of current work.

Chapter 4

Validation

4.1 Overview

This chapter presents a variety of tests conducted to verify and validate the SPH code that is constructed by the author using the parallel library OpenFPM in C++. In the section 4.1, a 2D lid driven cavity case is used to verify the viscosity model and boundary implementation in the current SPH model. In the section 4.2, a 3D dam break case is used to verify the accuracy of the approximation of hydrodynamic pressure and its ability to deal with the violent interaction between free surface and solid. In section 4.3, a cylinder water entry case is employed to verify that the current SPH model is capable of capturing the interaction between fluid and floating body. The effectiveness of the current DEM-SPH model is validated by using a test case based on the 3D dam break case in the section 4.4 with additional two free moving floating boxes. Lastly, in section 4.5, flow passing though a rectangular duct is applied to verify the current open boundary model.

4.2 Lid-driven cavity

The Lid-driven cavity case in this section aims to verify the effectiveness of no-slip and moving wall boundary condition and validate the viscous model

with the experimental result presented by Ghia et al. (1982). The sketch of the case is shown in Fig. 4.1, where the boundary is constructed with no-slip walls and one moving wall at top with constant velocity $V = (U, 0)$. In the current case, the length (L) of both moving walls and no-slip walls is chosen to be 1. The region enclosed by the boundaries is the fluid domain, where the initial density and initial pressure are chosen to be 1 and 0 respectively. The initial velocity of the fluid domain is set to 0. Since the experimental result presented by Ghia et al. (1982), was setup with $Re = 1000$, the dimension of viscosity in the current case is chosen to be $\nu = 0.001$. The reference sound speed of water in this case is chosen according to Eq. 3.5, where $c_0 = 10$. The fluid domain is discretised with particle spacing $dp = 0.005$, which results in 200×200 particles. For determining, whether the flow of the system reaches steady state, the velocity changed along the Y axis is applied as follows

$$\begin{cases} \text{steady} & \text{if} \quad max(\frac{V^t(0,y) - V^{t-1}(0,y)}{V^t(0,y)}) < 0.01 \\ \text{unsteady} & \text{else} \end{cases} \tag{4.1}$$

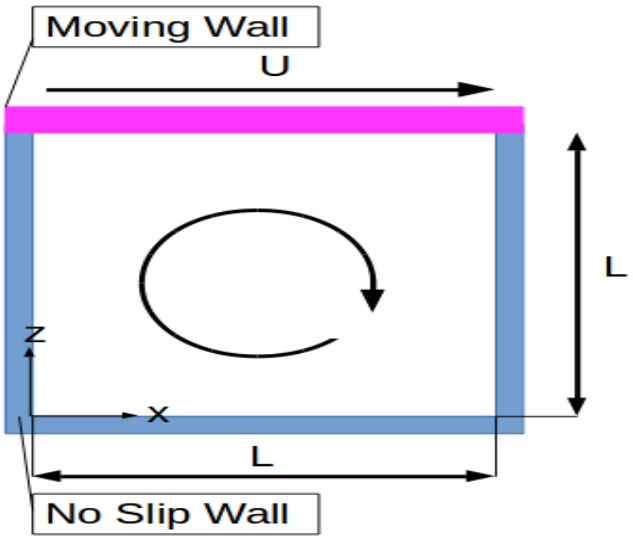

FIGURE 4.1: Sketch of the 2D lid-driven cavity test case.

In the current model, the simulation reaches steady state at $t = 42s$ and velocity contour at $t = 42s$ as shown in Fig. 4.2. At $t = 42s$, a vortex is formed in the center of the fluid domain, and the velocity of the fluid region near the non-slip boundaries is 0. It can also be observed that the velocity of the fluid region near the moving wall is 1, which corresponds to the specified velocity of the moving wall. This result shows that the current moving boundary and non-slip boundary implementation are effective. The velocity profile of the current SPH model compares with the result presented by (Ghia et al., 1982) at steady state, is shown in Fig. 4.3 and 4.4. As shown in Fig. 4.3, the velocity of flow in the Y direction along the X-axis is 0 at X = -0.5 and X = 0.5. This is because the flow next by the fixed wall boundary on the left and right side of the system is affected by the viscosity model. A similar trend can be seen in the Fig. 4.4 that the velocity along the Y-axis in the X direction is equal to 1 when the flow approaches to the moving wall at the top of the system and decrease to 0 when the flow is affected by static wall at the bottom of the system. Obviously, the simulation results agree well with Ghia et al. (1982)'s results and verify the boundary conditions and viscosity models of the current SPH model.

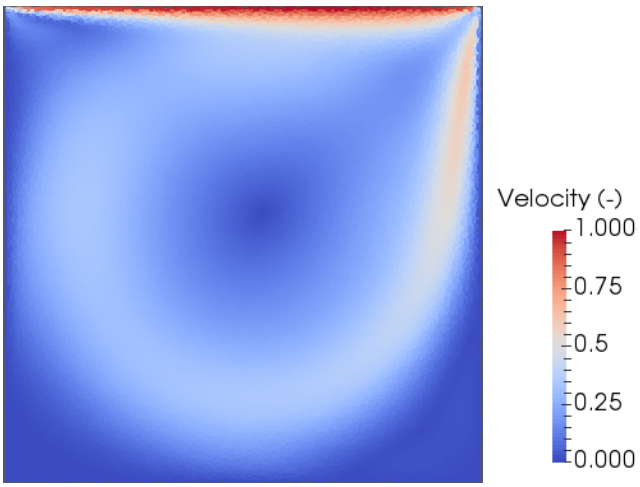

FIGURE 4.2: Contour of velocity of 2D lid driven case at $t = 42s$, where the flow reached the steady state.

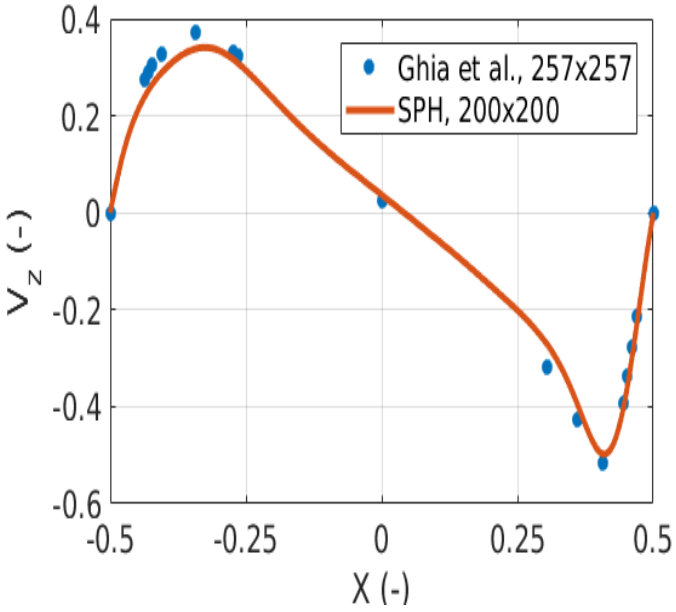

FIGURE 4.3: The velocity profile of 2D lid driven case at $t = 42s$ on $y = 0$.

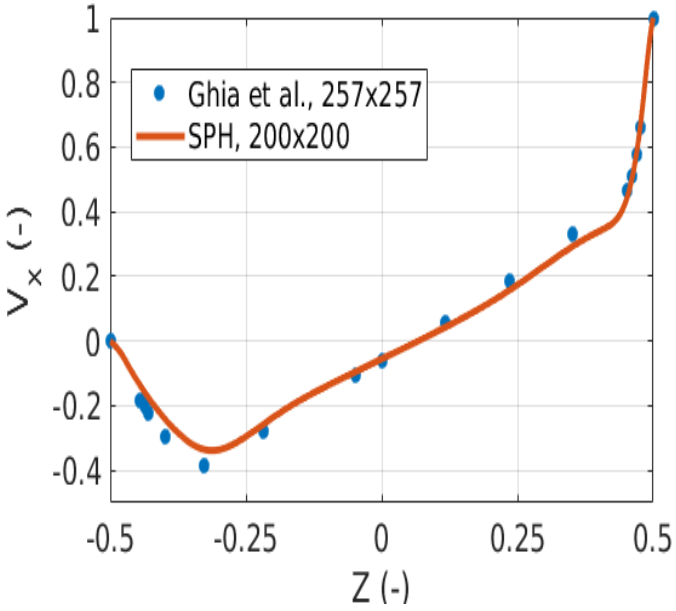

FIGURE 4.4: The velocity profile of 2D lid driven case at $t = 42s$ on $x = 0$.

4.3 3D dam break

A 3D dam break experiment in Kleefsman et al. (2005) was originally designed to analyze the impact of green water on the deck equipment. This test case is a violent interaction between free surface and rigid body. Therefore, in this section the 3D dam break test case, presented by Kleefsman et al. (2005), is used to validate the interaction between free surface flow and rigid body in the current SPH model. The sketch of the test case is shown in Fig. 4.5 (a). Still water with density $\rho = 1000kg/m^3$ is placed at the right-hand side of the domain and a rigid obstacle is deployed at the left-hand side of the domain. The free slip boundary condition is assigned to all solid wall boundaries. The entire system is discretized with initial particle spacing $\triangle x = 0.0161m$. The artificial sound speed is chosen according to Eq. 3.5, where $c_0 = 25m/s$, while the initial pressure of the fluid is calculated based on the Bernoulli equation as follows:

$$p = \rho_0 * g * \triangle z; \tag{4.2}$$

where $\triangle z$ is defined as the vertical distance from the fluid surface to the fluid particle.

In order to analysis the impact of flow on the obstacle, pressure sensor P1 and P2, is placed on the right side of the obstacle, as shown in Fig. 4.5(b). Besides P1 and P2, an additional pressure sensor P5 is placed on the top of the obstacle. Snapshots of simulation and experiment are shown in Fig. 4.6 - Fig. 4.10. As Fig. 4.6 - Fig. 4.10 show, there is a good agreement between the current SPH model and the experimental results. As Fig. 4.6 shows, a flow front has been formed that is heading toward the obstacle at $t = 0.25s$. The flow front firstly hits the obstacle at $t = 0.4s$ and it is being separated by the obstacle at $t = 0.56s$ as shown in Fig. 4.7 and Fig. 4.8. At $t = 0.84s$, the separated flow front reaches the left side of the boundary and merged together at $t = 1.2s$ as shown in Fig. 4.9 and Fig. 4.10.

Pressure time histories at P1, P2 and p5 are shown in Fig. 4.11. It can be observed that the flow front reaches the obstacle at about $t = 0.4s$, and

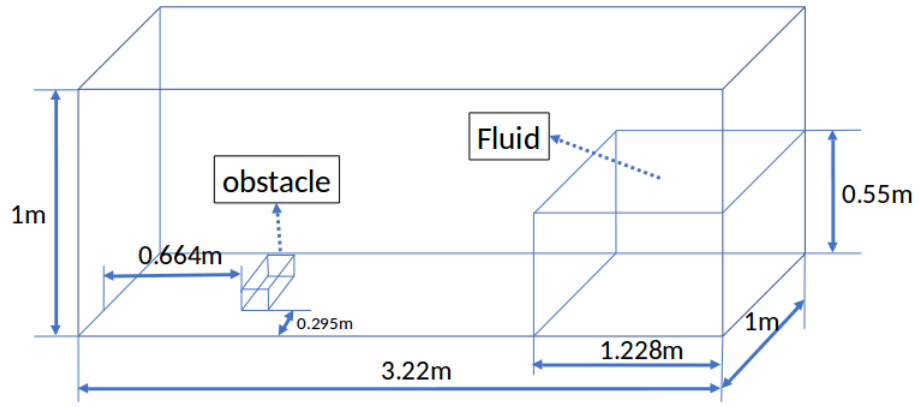

(a)

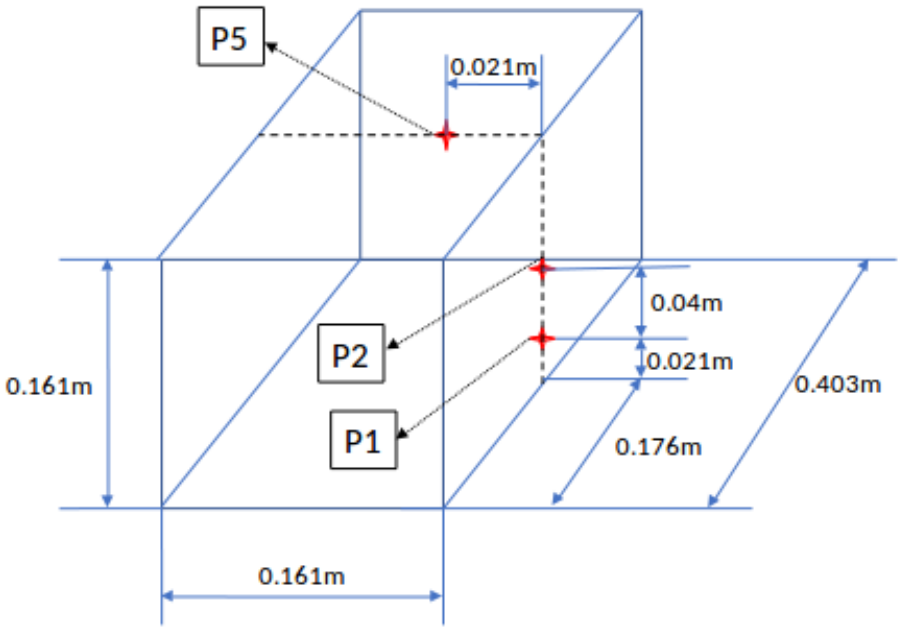

(b)

FIGURE 4.5: (a) Sketch of the 3D dam break case. (b) Sketch of the obstacle and the pressure transducers on the obstacle (P1,P2,P5).

the flow direction of the flow hitting the obstacle is suddenly altered to the opposite direction. This sudden change creates a peak of pressure, which can be observed from pressure time diagrams of P1 and P2 at $t = 0.4s$. The peak of both P1 and P2 is higher than the experimental data. This is due to the fact that particle resolution is not fine enough, which could be solved by simply increasing the particle resolution. As the Fig. 4.11 (c) shows, the pressure at p5 starts to increase at $t = 1.2s$. This is mainly due to the fact that the flow front after hitting the left side of the wall boundary has returned and covered the top of the obstacle. In general, approximation of the pressure of the current model agrees very well with the experimental result. Which means that the current SPH model is capable of capturing the violent interaction between free surface flow and rigid body very well.

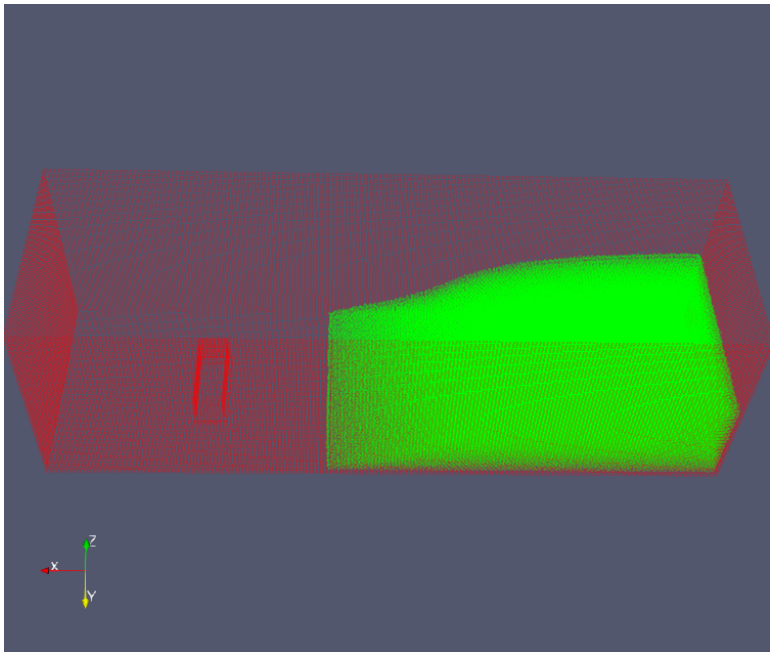

(a)

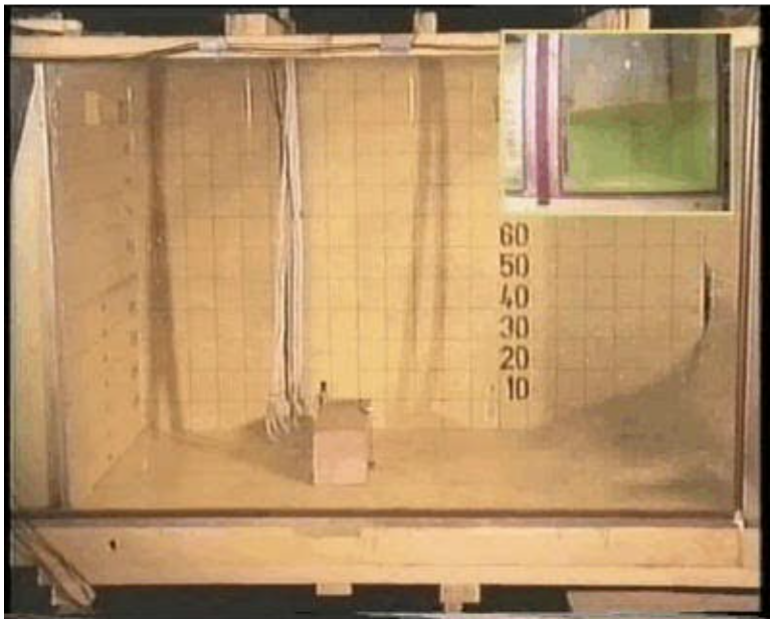

(b)

FIGURE 4.6: Snapshot of the 3-D dam breaking test compared with experiment (Kleefsman et al., 2005) at $t = 0.25s$.

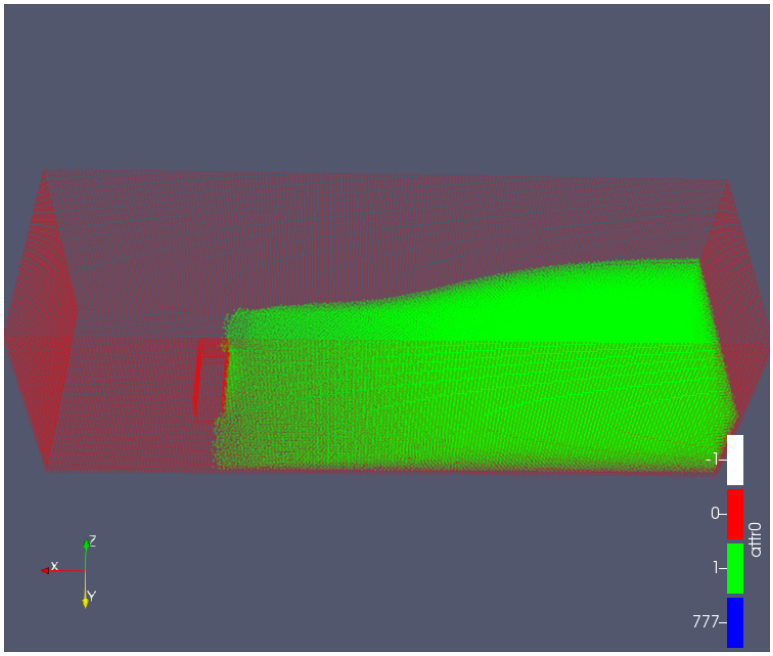

(a)

(b)

FIGURE 4.7: Snapshot of 3-D dam breaking test compared with experiment (Kleefsman et al., 2005) at $t = 0.4s$.

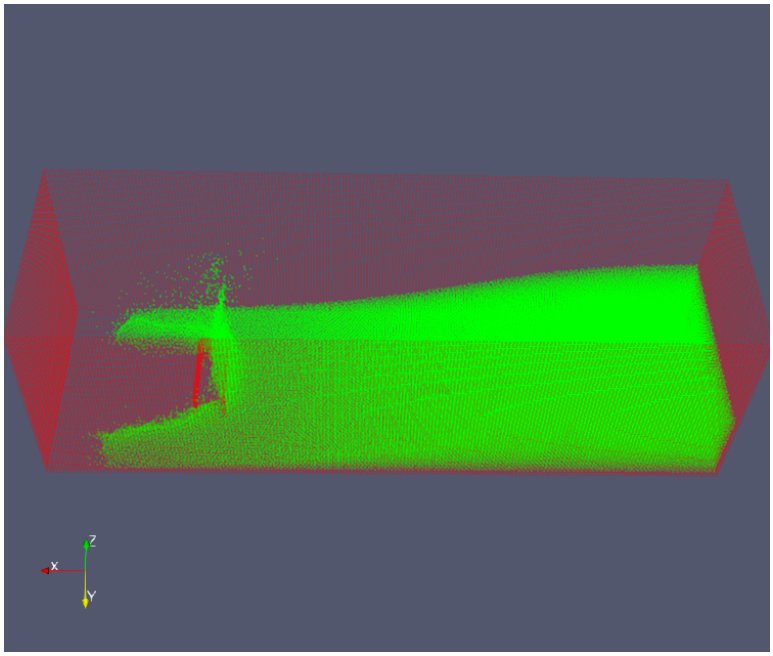

(a)

(b)

FIGURE 4.8: Snapshot of 3-D dam breaking test compared with experiment (Kleefsman et al., 2005) at $t = 0.56s$.

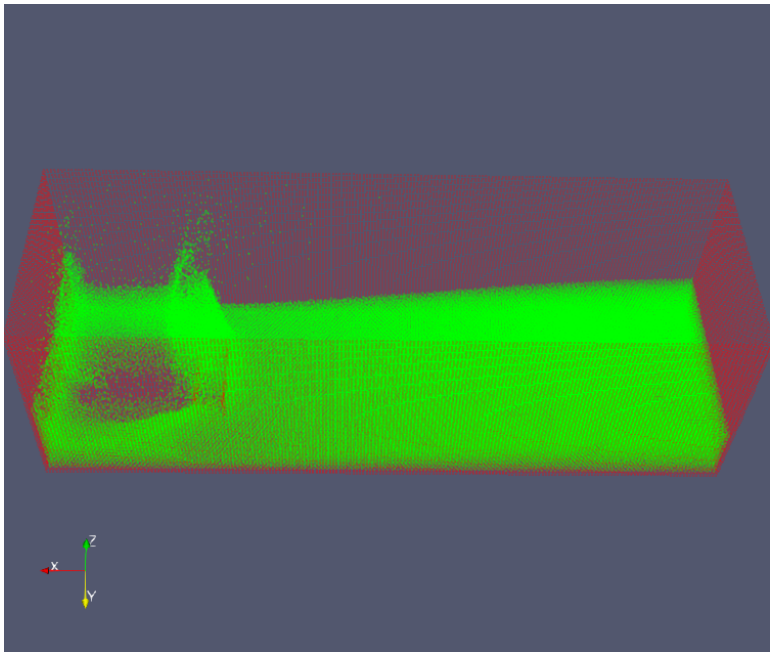

(a)

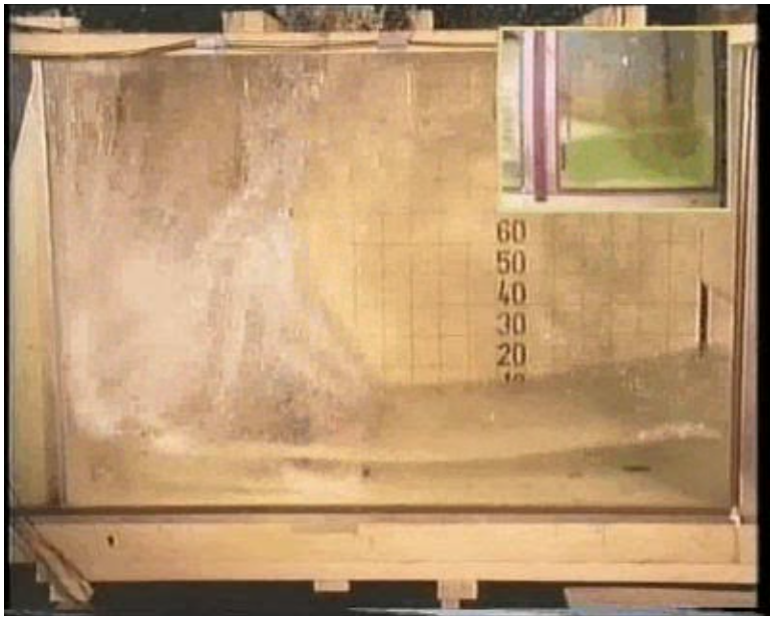

(b)

FIGURE 4.9: Snapshot of 3-D dam breaking test compared with experiment (Kleefsman et al., 2005) at $t = 0.84s$.

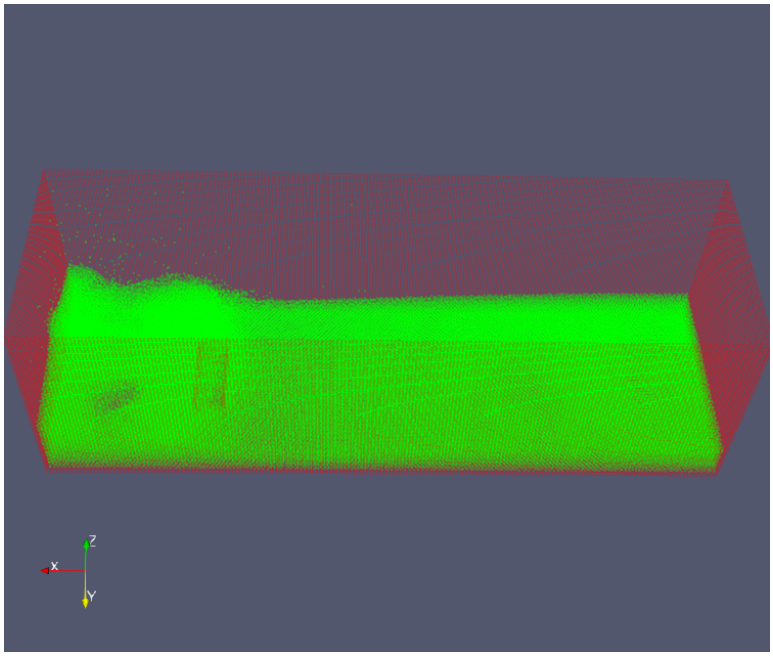

(a)

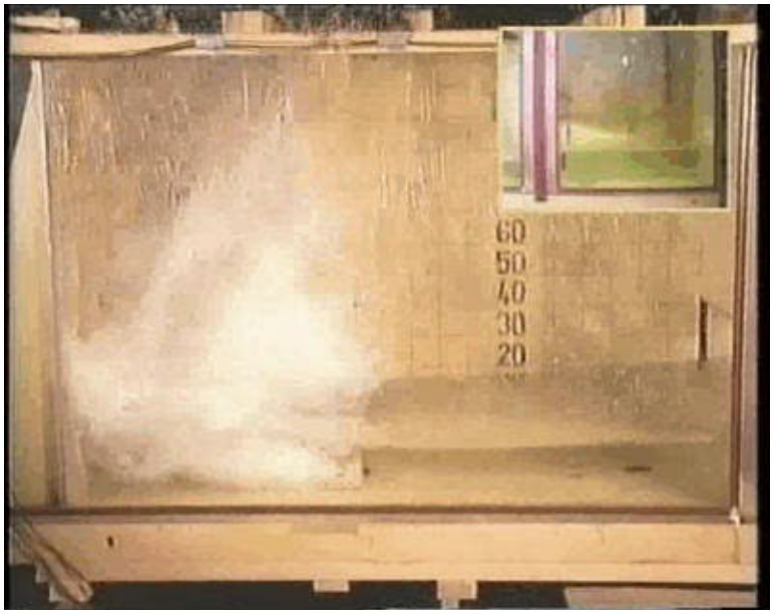

(b)

FIGURE 4.10: Snapshot of 3-D dam breaking test compared with experiment (Kleefsman et al., 2005) at $t = 1.2s$.

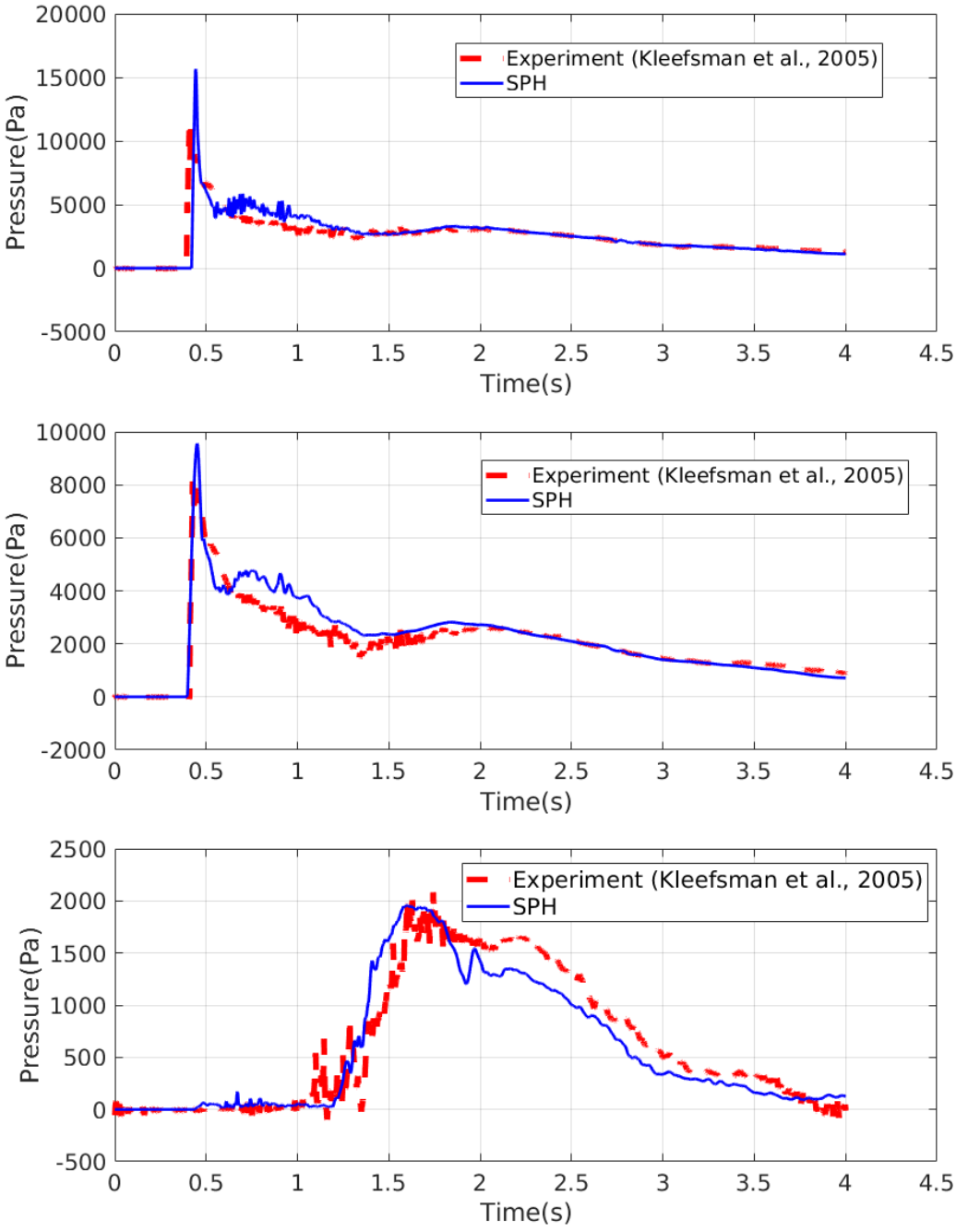

FIGURE 4.11: Pressure time histories at (a) P1, (b) P2 and (c) P5, compared with experimental data presented by Kleefsman et al. (2005).

4.4 3D cylinder water entry

In this section, a cylinder with an oblique angle entering the water case, as the water entry of a 3-D cylinder test case presented by Sun et al. (2015b), is used to verify that the current model is suitable to simulate the interaction between floating body and free surface flow in 3D. The sketch of this test case is shown in Fig. 4.12 that a cylinder is entering the water with initial velocity $-1.92m/s$ in Z direction. The oblique angle between the cylinder and the water surface is $\theta = 35°$, while the center of gravity of the cylinder is at $(0.025m, 0m, 0.34m)$. The mass of the cylinder is $0.145kg$ and the diameter of the cylinder is $0.032m$ with 0.15m in length. No slip boundary condition and free slip condition are assigned to wall boundary and the cylinder respectively. The initial pressure of the water is given according to Eq. 4.2. The entire system, including wall boundary, cylinder and fluid domain, is discritized with the particle spacing $dp = 2.410^{-3}m$. And the reference sound speed is chosen to be $20m/s$. Fig. 4.13 -15 are the snapshots of the velocity contour. As Fig. 4.13 shows, the right side of the cylinder starts to enter the water at 0.05s and the center of gravity of the cylinder is completed under the water surface at $t = 0.02s$. At $t = 0.035s$, after the cylinder has entered the water its falling speed has decreased dramatically as shown in Fig. 4.14. Fig. 4.15 shows that the cylinder is in the water and an empty area is created above the cylinder.

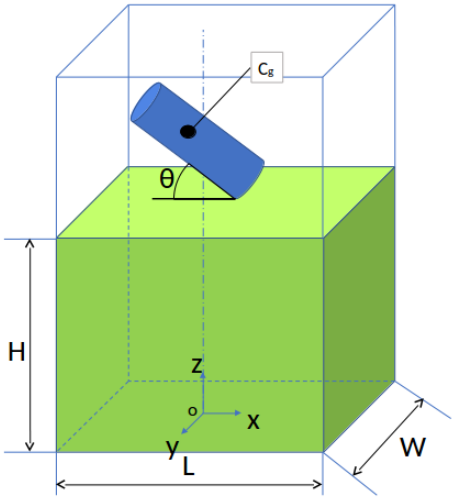

FIGURE 4.12: The Sketch of cylinder water entry case.

Fig. 4.16 shows the position and rotation history of the cylinder. It could be observed that between $t = 0s$ and $t = 0.1s$, the center of gravity in the Z direction drops from 0.35m to 0.205m and the oblique angles of the cylinder decrease from 35 to 4. The change of the oblique angles is due to the fact that the right side of the cylinder impact the water faster than the left side, which gives a counter clockwise moment force in the Y direction about its central of gravity. It can be seen that in the simulation, the cylinder's sinking speed is slightly slower than the experimental data, and the cylinder's rotating speed is faster than the experimental data. The main reason is that the current SPH model does not consider the surface tension, so the void area on the top of the cylinder (as shown in Fig. 4.17(b)) is larger than the experimental result (as shown in FIG. 4.17(a)), and eventually leads to the cylinder in SPH experiences more resistance. In summary, the result of simulation in this test case verifies that the current SPH model is capable of simulating the interaction between floating body and free surface.

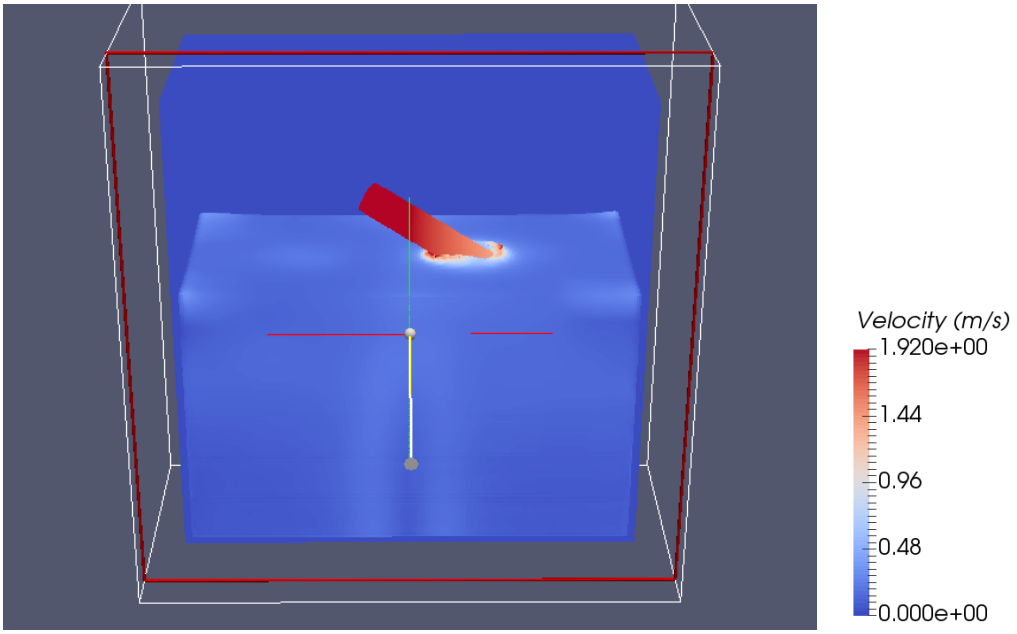

(a)

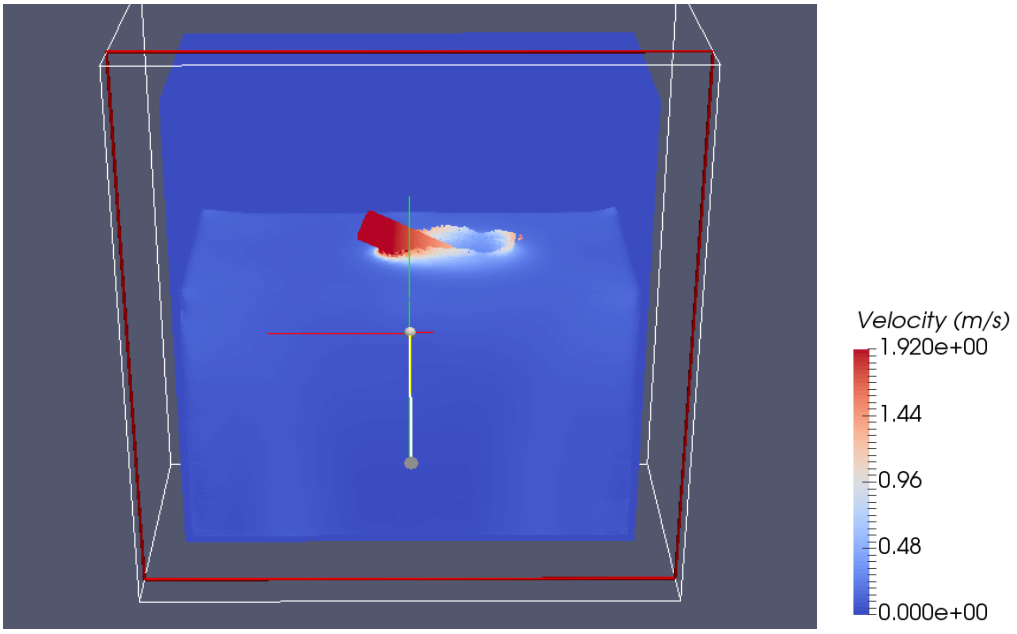

(b)

FIGURE 4.13: Snapshots of the contour of the velocity of the cylinder falling case at (a) $t = 0.005s$ and (b) $t = 0.02s$.

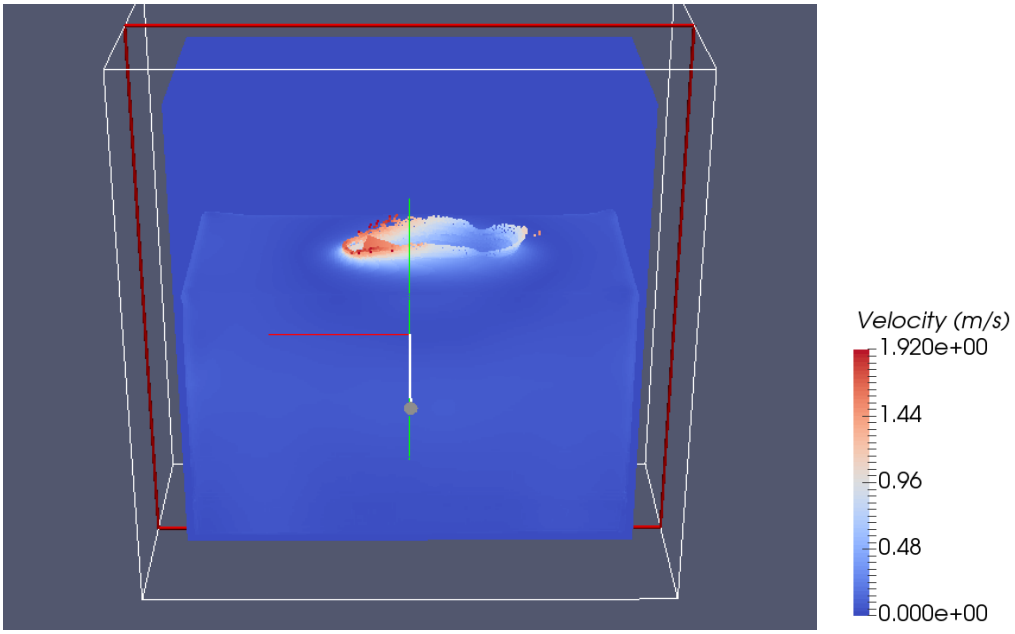

(a)

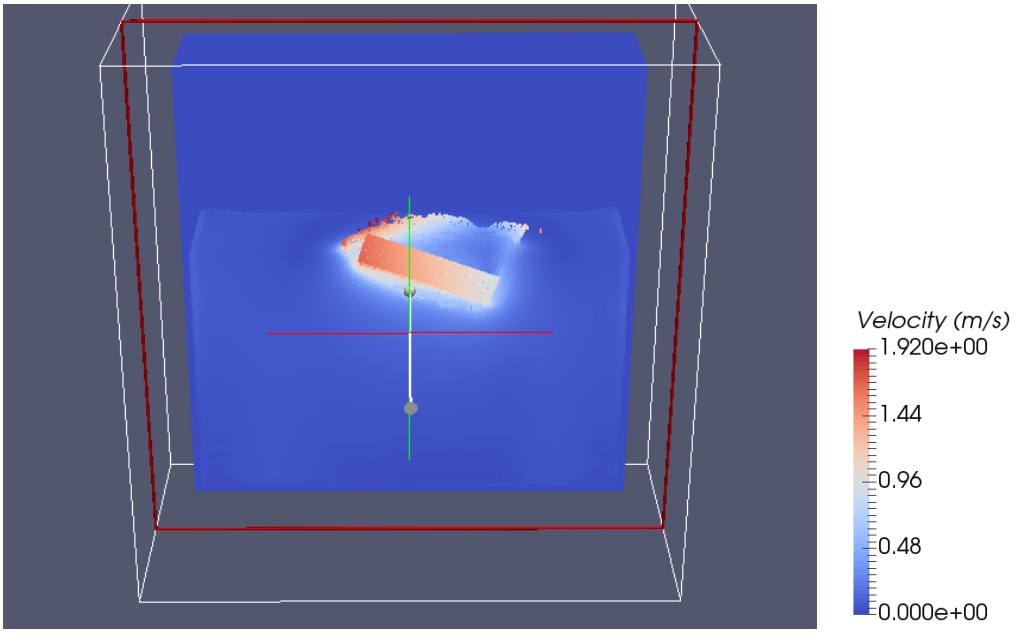

(b)

FIGURE 4.14: Snapshots of the contour of the velocity of the cylinder falling case at $t = 0.035s$. (a) shows the whole domain and (b) shows the velocity contour on half of the fluid domain at one side of the coordinate plane $oxz(y < 0)$

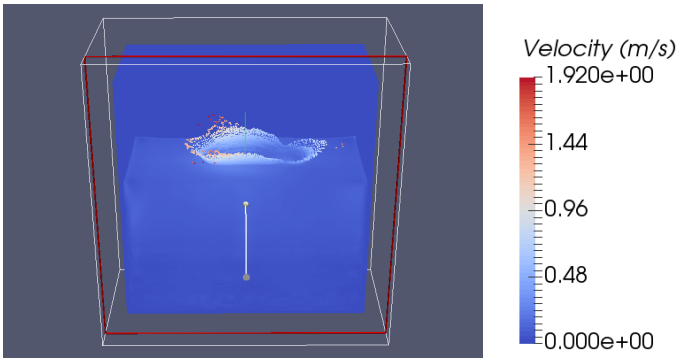

(a)

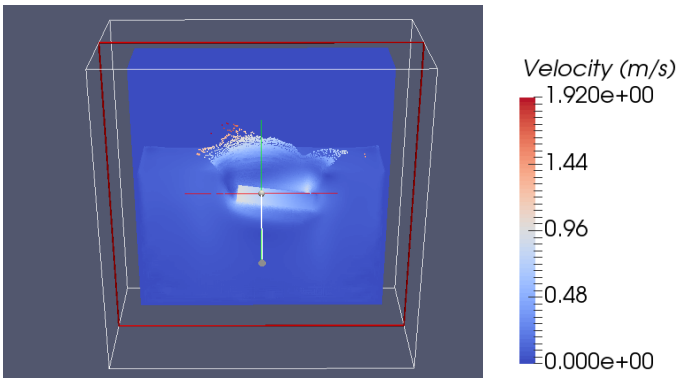

(b)

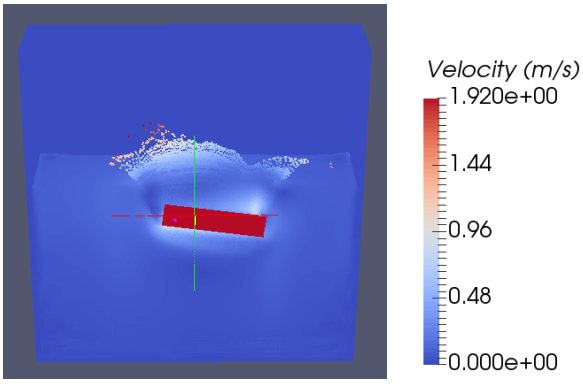

(c)

FIGURE 4.15: Snapshots of the contour of the velocity of the cylinder falling case at $t = 0.075s$. (a) shows the velocity contour on whole domain, (b) shows the velocity contour on half of the fluid domain at one side of the coordinate plane $oxz(y < 0)$ and (c) shows the velocity contour with visible enhanced on the falling cylinder on half of the fluid domain at one side of the coordinate plane $oxz(y < 0)$.

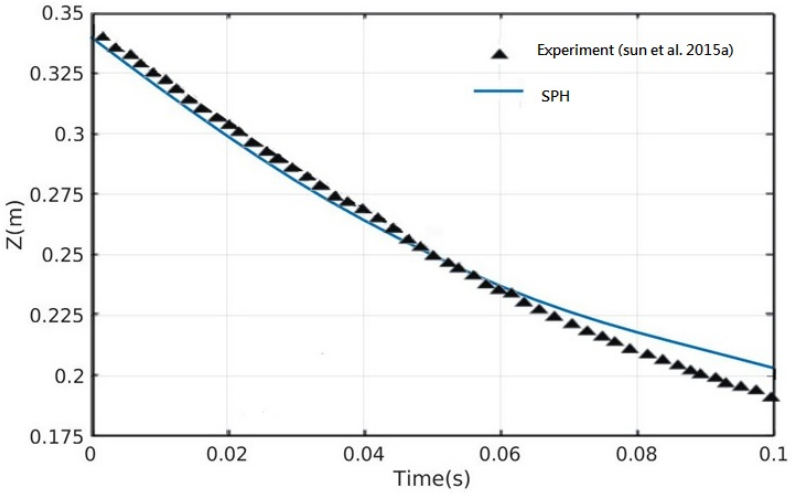

(a)

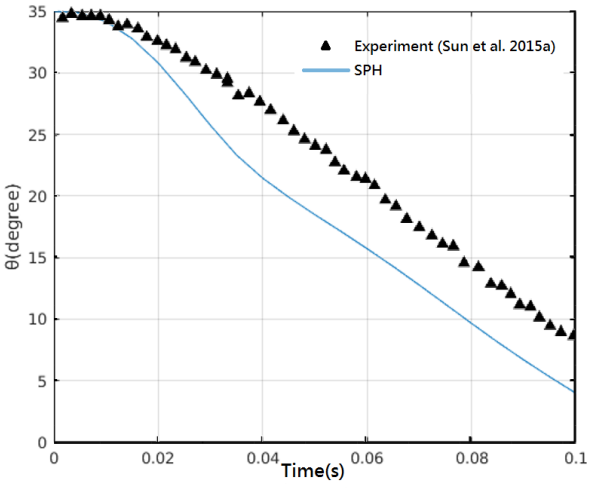

(b)

FIGURE 4.16: The results of SPH were compared with the experimental data presented by (Sun et al., 2015b). (a) The plot of position of the cylinder in Z direction and (b) The plot of the oblique angle of the cylinder about Y axis.

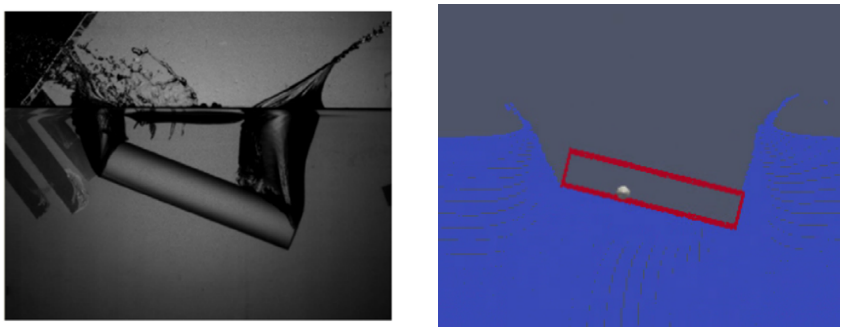

(a) (b)

FIGURE 4.17: Snapshot of the result of $t = 0.068s$. (a) Experiment result presented by (Sun et al., 2015b) (b) Simulation result from the current SPH model.

4.5 2 boxes transporting in 3D dam break

To verify the effectiveness of the current DEM-SPH model, this section employs a 3D dam break case, which is similar to the one in the section 4.3, where additional 2 boxes were released above the fluid domain at $t = 0s$. The weight of the box is $3.3384kg$ and the length of the box is $0.161m$. At $t = 0s$, the box at left side is released from $(0.5424, 0.3805, 0.6744)$ and the box at the right-hand side is released from $(1.0424, 0.5805, 0.6744)$. The entire domain is discrtized with default particle spacing $dp = 0.0161m$ and dummy particles is used directly as the spherical subshape of the DEM. Fig. 4.18 shows the snapshots of the simulation results using current SPH model, where the wall boundary is labelled with red color, and fluid particles are labelled with green color. The boxes are labelled with blue color. Fig. 4.18(a) shows that the boxes start to enter the water and driven by the flow in the direction towards the obstacle at $t = 0.1s$. As shown in Fig. 4.18(b), the box at the left side moving faster toward the obstacle than the box at the right, at t= 0.9. This is due to the left part of the fluid velocity move faster than the right side. The box at left side eventually hits the obstacle at $t = 1.0s$ as shown in Fig. 4.18(c). Fig. 4.18(d) shows that at $t = 1.1s$,

velocity of the box suddenly changes from the direction of the obstacle to the direction of the opposite side of the obstacle. This due to the box at left side colliding with the obstacle and a solid-solid contact force calculated through Eq. 3.58 is applied on the box to stop the box from penetrating the wall of the obstacle. As shown in Fig. 4.18 (e), at $t = 1.6s$, the front flow of water hits the left side of the boundary, changes the main body of the water flow and starts to move in the opposite direction to the obstacle. Fig. 4.18(f) shows that, both boxes are driven towards the opposite side of the obstacle at $t = 2.4s$. In summary, the results in this section show that the DEM-SPH model is effective and can prevent the floating body from penetrating the boundary during the collision.

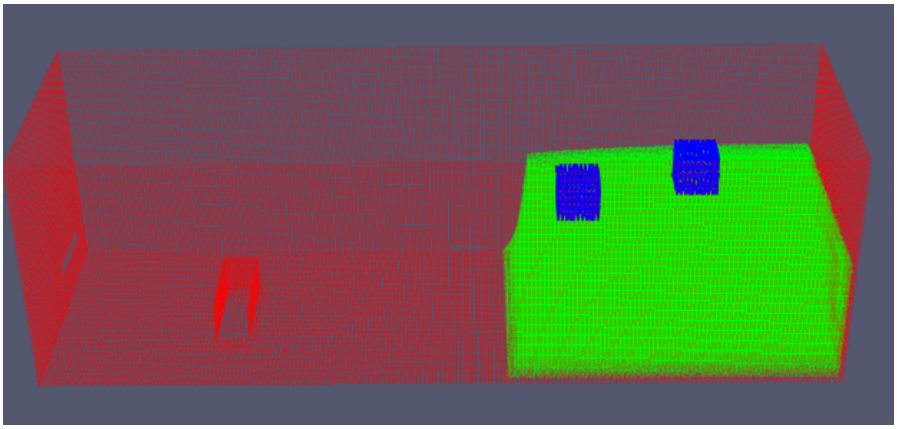

(a)

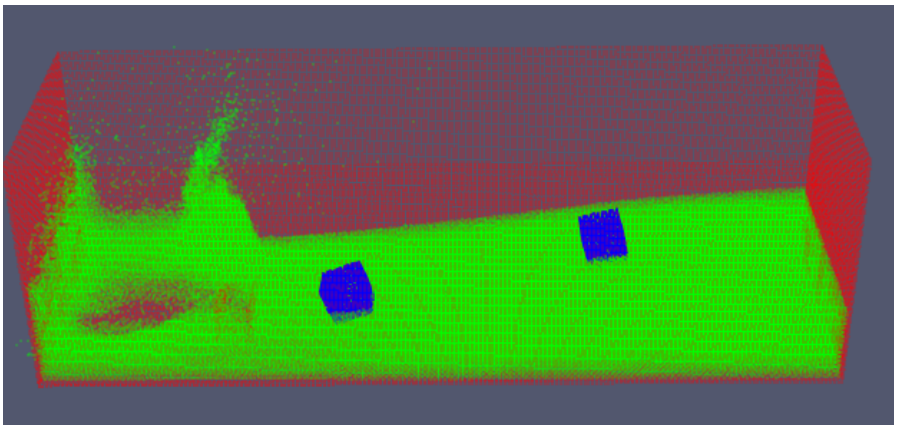

(b)

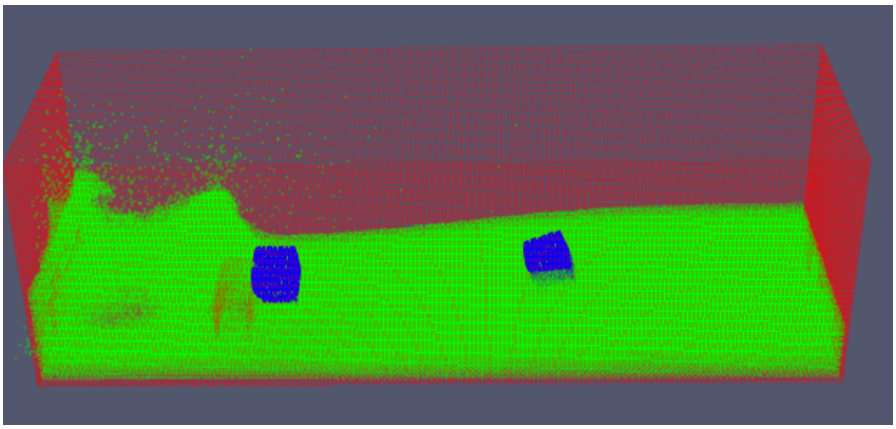

(c)

FIGURE 4.18: The snapshots of simulation result of 3D dam break with 2 additional floating boxes at (a) $t = 0.1s$ (b) $t = 0.9s$ (c) $t = 1.0s$ (d) $t = 1.1s$ (e) $t = 1.6s$ and (f) $t = 2.4s$. The dummy particles and fluid particles are labelled with red and blue colour respectively while free falling boxes are labelled with blue colour.

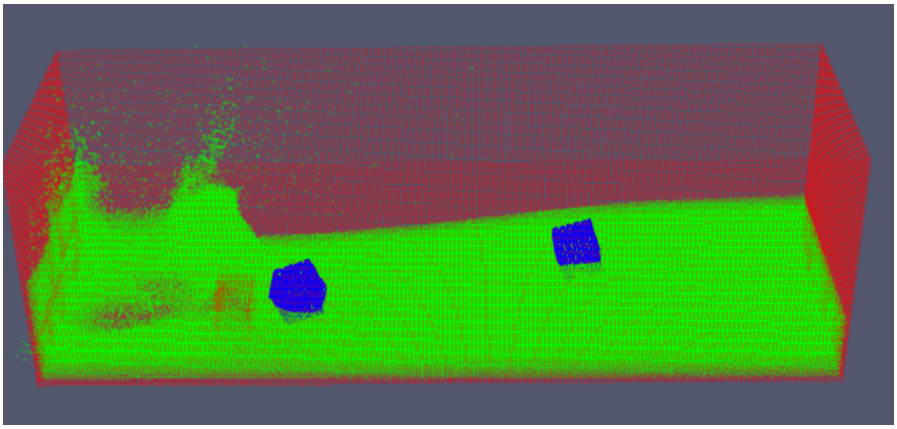

(d)

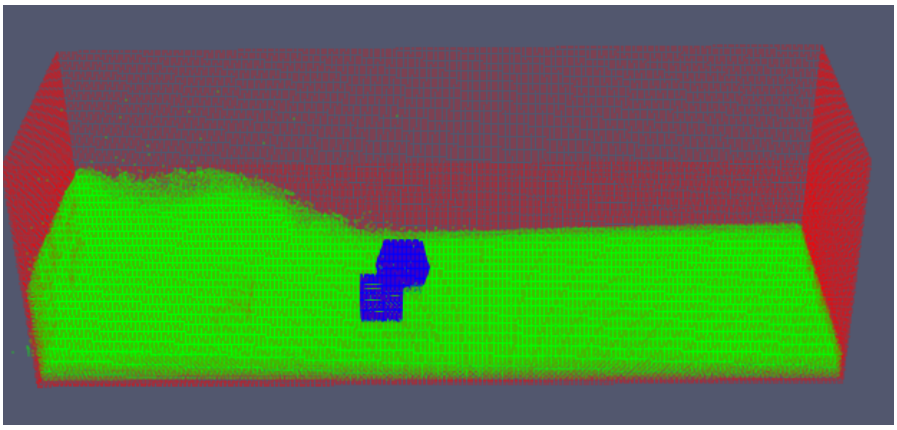

(e)

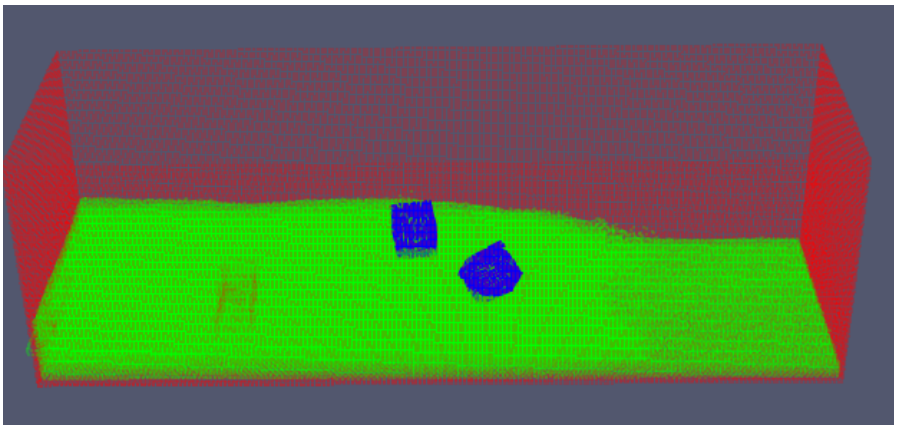

(f)

FIGURE 4.18: The snapshots of simulation result of 3D dam break with 2 additional floating boxes at (a) $t = 0.1s$ (b) $t = 0.9s$ (c) $t = 1.0s$ (d) $t = 1.1s$ (e) $t = 1.6s$ and (f) $t = 2.4s$. The dummy particles and fluid particles are labelled with red and blue colour respectively while free falling boxes are labelled with blue colour.

4.6 Flow passing though rectangular ducts

In this section, a flow passing through a rectangular duct test case is applied to validate that the open boundary method developed in section 3.3, is suitable to be used as the inlet and outlet boundary in three dimension for SPH model. To prove that the current model is valid, the theoretical model of flow passing through rectangular ducts presented by Spiga and Morino (1994) is used as the reference to compare with the current model. The sketch of the numerical setup is shown in Fig. 4.19. The length of the channel L is set to $1m$, while both height (H and width W are set to $0.25m$. A uniform inlet velocity $V_x = 0.14m/s$ is applied to the entrance of the channel and the pressure zero outlet condition is applied to the exit of the channel. The density of the fluid equals to $1000kg/m^3$ and its initial velocity is set to $V_x = 0.35m/s$. Except for the entrance and exist, no-slip condition is applied to all of the other boundary. The fluid domain in the channel is disctized by the particle spacing $\Delta x = 0.01m$.

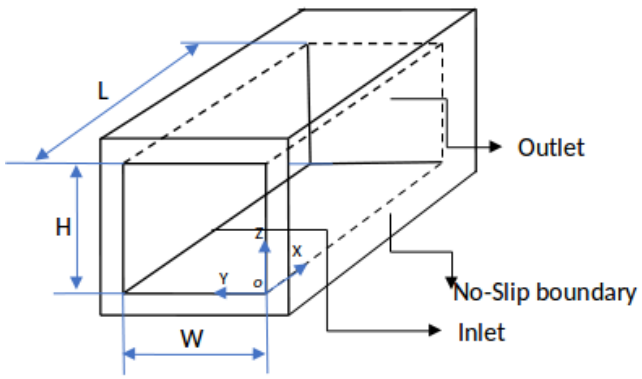

FIGURE 4.19: Sketch of flow passing though rectangular ducts.

Fig. 4.20 show the velocity (V_x) at $(x, y) = (0.7m, 0.125m)$ varying versus Z axis. It can be seen from Fig. 4.20 (a) shows, that, due to the initial velocity is given, the velocity profile at $t = 0s$ is equal to $0.35m/s$. As Fig. 4.20 (b)

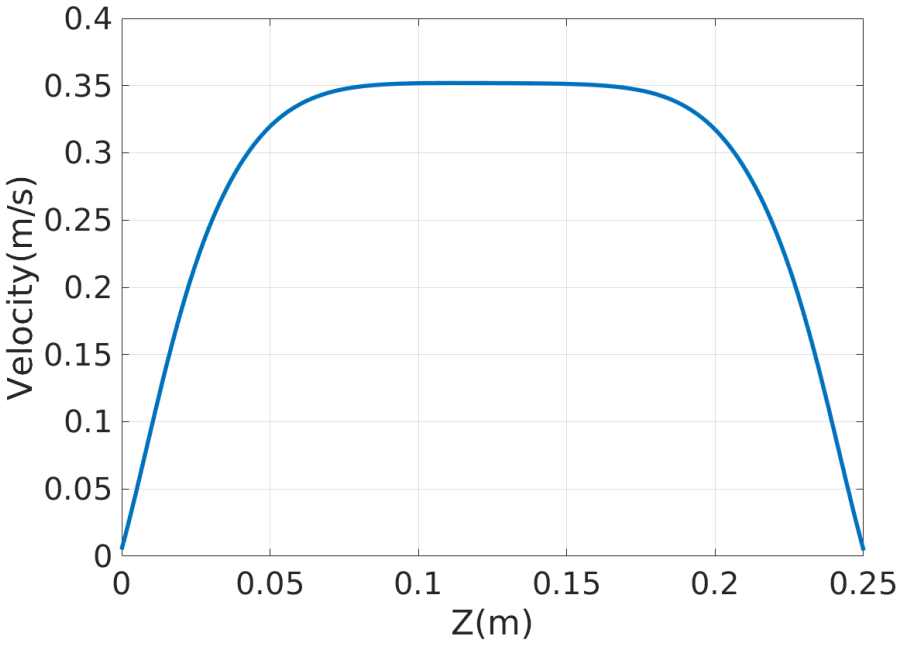

(a)

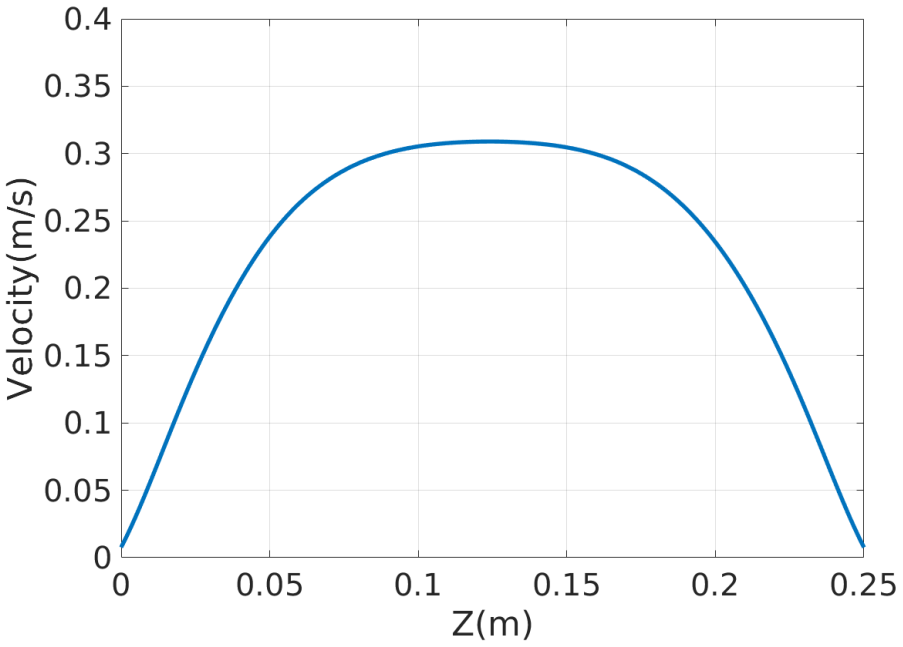

(b)

FIGURE 4.20: The velocity profile of flow passing though rectangular ducts along the z direction at $(x, y) = (0.7m, 0.125m)$ (a) $t = 0s$ (b) $t = 1s$ (c) $t = 5s$ (d) $t = 6s$.

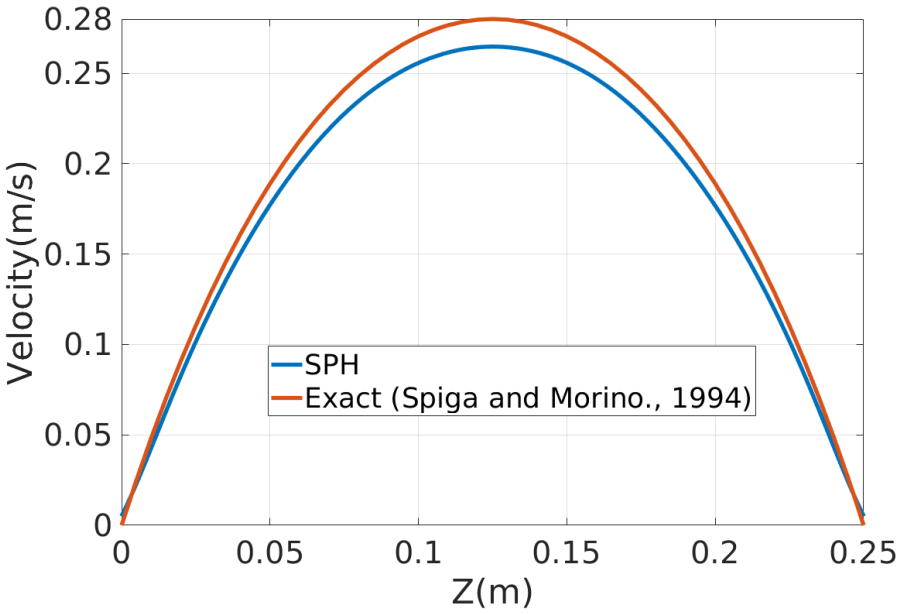

(c)

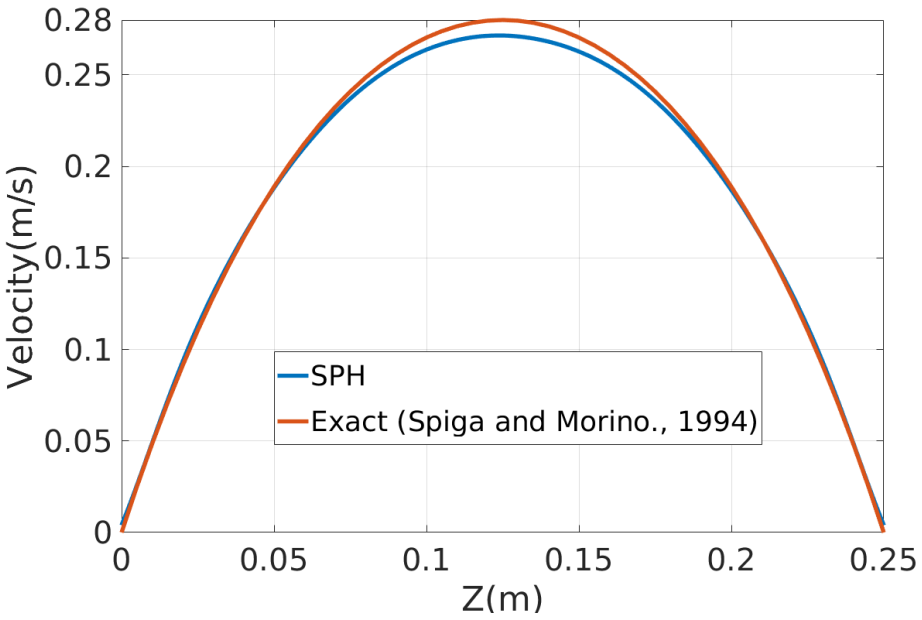

(d)

FIGURE 4.20: The velocity profile of flow passing though rectangular ducts along the z direction at $(x, y) = (0.7m, 0.125m)$ (a) $t = 0s$ (b) $t = 1s$ (c) $t = 5s$ (d) $t = 6s$.

- (d) show, withing time increased, the velocity profile slowly reached to its steady state at $t = 6s$. At $t = 6s$, the maximum velocity $V_{max} = 0.28m/s$ can be found at $z = 0.125m$, which is corresponding to the most further position from the wall on the cross section. Fig. 20(d) shows that, the velocity starts to decrease to zero within approach to the wall. This is due to the no-slip condition is applied to all the walls, this is due to the viscous force as section 4.1 demonstrated.

The velocity profile at $x = 0.7m$ varying versus Y and Z axis of the current SPH model at $t = 6s$ and the theoretical result presented by Spiga and Morino (1994) are presented in Fig. 4.20. It can be observed that at $t = 6s$ (which is the steady state of current numerical model) the current SPH model obtained a very good agreement compared with the theoretical result in general. The difference of the maximum velocity between the current model and the theoretical model, is only about 3%. In summary, the test case in this section proves that the current open boundary method is suitable to use as the inlet and outlet boundary in three dimensions.

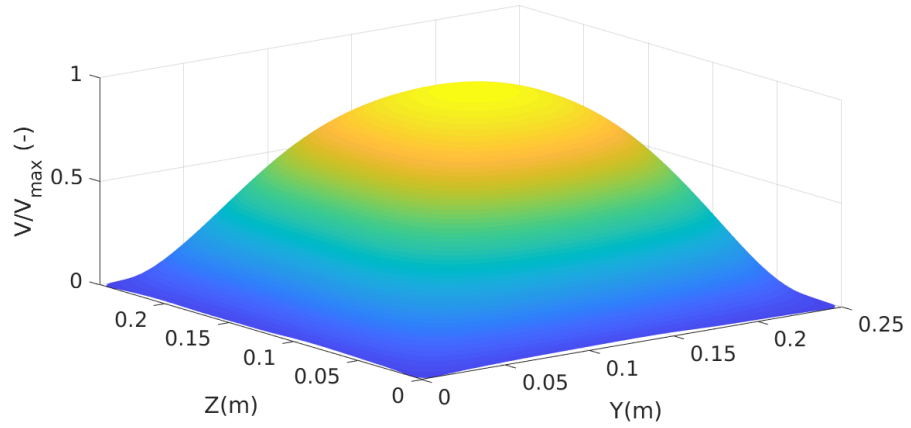

(a)

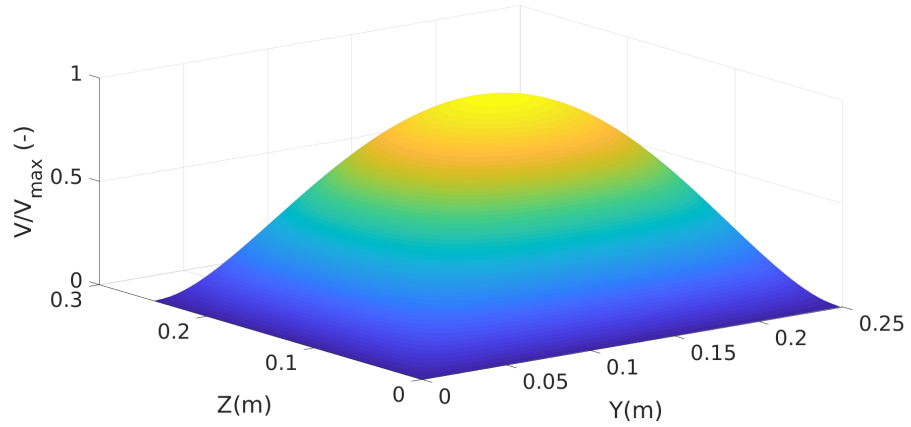

(b)

FIGURE 4.21: The velocity profile of flow passing though rectangular ducts at one side of the coordinate plane ozy and $x = 0.7m$. (a) is current SPH result and (b) the theoretical result presented by Spiga and Morino (1994).

Chapter 5

Case study

5.1 Overview

The main purpose of this thesis is to establish a numerical tool to predict and analyze the impact of a floating body on a structure during floods. In this chapter, two test cases of the impact of a floating body on a structure are presented. The first test case involves three floating bodies that are transported in a simple rectangular channel and hit on the wall of the channel. This test case demonstrates that the current numerical model is capable of tracing the trajectory of a floating body that is driven by the flow and bounce when the floating bodies hit the wall. The second test case applies a similar numerical scheme as the first test case, but instead of using a simple rectangular channel, a real river channel is used. In the second test case, the geometry of the test case is constructed according to the Mosel river flowing by Kesten, a town in the west of Germany. Cylinders are employed in this test case as the floating body, and they are placed on the surface of the river with a given initial speed. These floating bodies are driven by the current and flow downstream. Eventually, these floating bodies hit the structure along the river. The result of the impact caused by the floating bodies on the structure is further analyzed using Abaqus, which can predict the deformation of the structure. This test case demonstrates

that the current model can capture the trajectory of bodies floating along the river. Additionally, it shows that this model can be used as a numerical tool by water management authorities to predict the trajectory of floating body that is transported in a flooded river.

5.2 Impact of a floating body along a rectangular open channel flow

In this section, a numerical simulation has been employed to investigate whether the current SPH model can capture the trajectory of a floating body that is driven by the flow in an open channel. The numerical setup is presented in Section 5.1.1, and the results and discussion are presented in the section 5.1.2.

5.2.1 Numerical setup

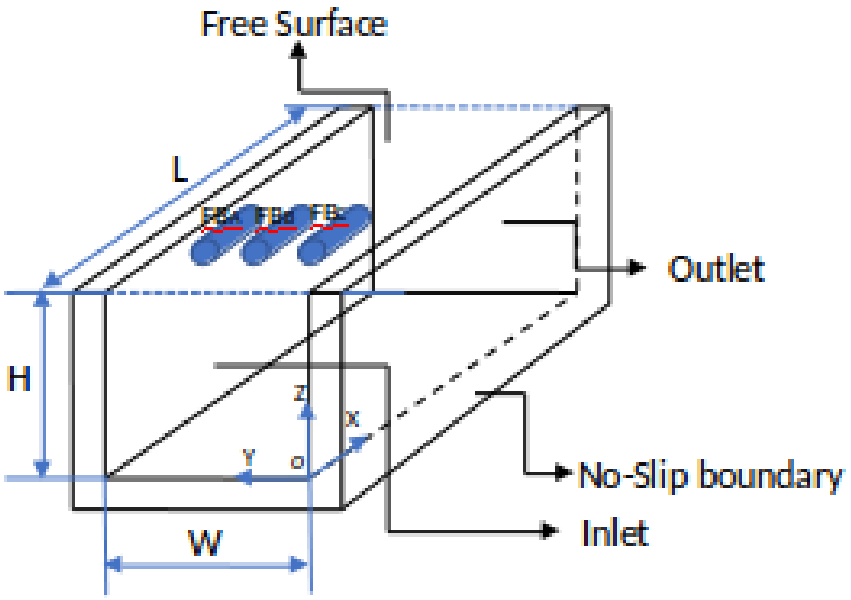

FIGURE 5.1: Schematic of the impact of a floating body along a rectangular open channel flow

The schematic of the test case in this section is illustrated in Fig. 5.1, where the channel is $5m$ in width ($W = 5m$) and $5m$ in height ($H = 5m$). The length of the channel is $10m$ ($L = 10m$), which is long enough to allow the floating bodies to hit the wall of the channel. As Fig. 5.1 shows, the front of the channel is where the inlet of the flow is, and the rear side of the channel holds the outlet. The channel is entirely filled with water, which means that the water level equals 5 m, and the reference density of the fluid is 1000 kg/m^3. The initial velocity of the fluid is set to 2 m/s along the X-direction. The point of origin for this test case is located at the bottom right corner of the channel, as Fig. 5.1 indicates. The floating bodies in this test case are represented by cylinders that are ($2m$ in length and $0.25m$ in radius. These are initially placed on the surface of the fluid. The reference density of these floating bodies is 750 kg/m^3. The first floating body, which is denoted

as FB_A, is initially located at $(3, 4, 5.4)$. The second floating body (FB_B) is located at $(3, 2.5, 5.4)$. Finally, the last floating body (FB_C) is located at $(3, 1, 5.4)$. In this section, the no-slip boundary condition is adopted for all solid wall boundaries, including the surface of the floating body. The uniform inlet condition is applied to the entrance of the channel, 2 m/s in X-direction, while the zero pressure condition is applied to the outlet. The particle spacing (Δx) to be used in the SPH model in the current case is 0.05 m, which resulted in around 2 million particles being used to conduct this simulation.

5.2.2 Results and discussion

The snapshot of the simulation results is presented as Fig. 5.2 and Fig. 5.3. It can be seen that at $t = 0s$, all the floating bodies are located evenly in the Y-direction inside the channel and slightly above the water level. At $t = 0.47s$, all three floating bodies move according to the given initial velocity, while the FB_C has almost reached the upper side of the wall. At $t = 0.49s$, the FB_C collides with the upper side of the wall, resulting in a sudden change of the velocity in the Y direction from positive to negative. At $t = 0.51s$, the FB_C starts traveling in the inverse-Y direction, while FB_A and FB_B continue traveling along the Y direction.

From the results of the current simulation, it can be observed that the current model can capture the interaction between the floating body and fluid, when the inlet and outlet conditions are prescribed. More importantly, the results reveal that the current numerical model is capable of capturing the impact between a floating body and a solid boundary. Therefore, it was deemed suitable to extend the current model to a real-world case to predict the impact of a floating body on a structure during flooding.

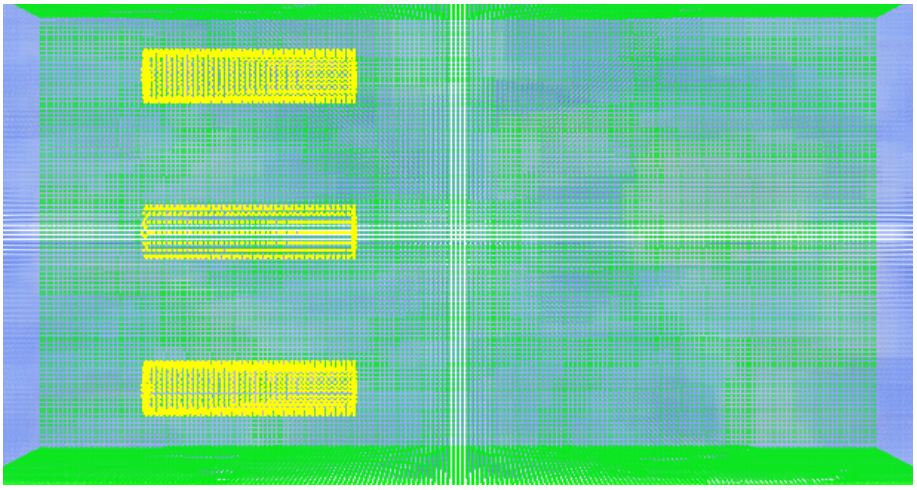

(a) t = 0 s

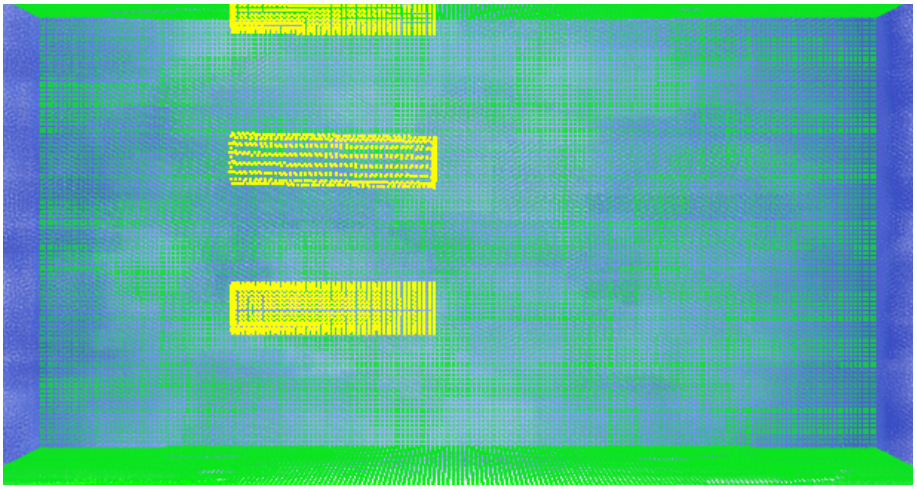

(b) t = 0.47 s

FIGURE 5.2: The snapshots of the simulation's result: the impact of floating body in a rectangular open channel flow at (a) t = 0 s (b) t = 0.25 s (c) t = 0.38 s (d) t = 0.51 s.

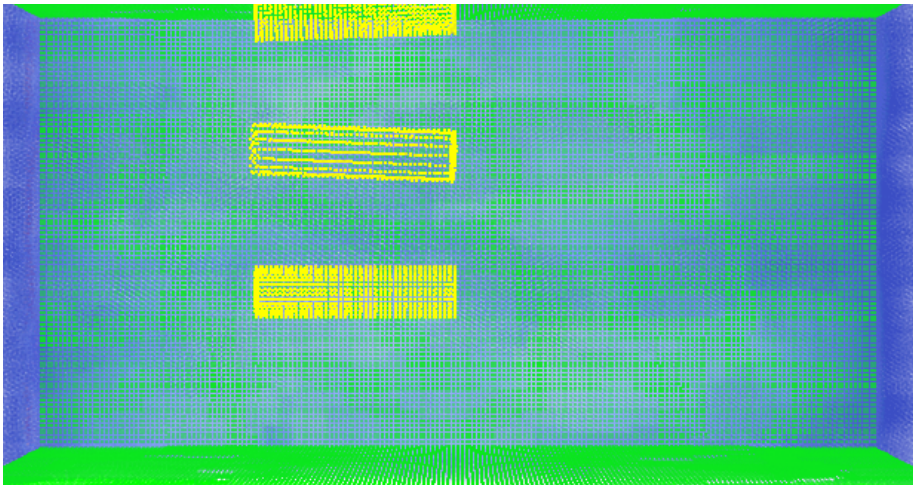

(c) t = 0.49 s

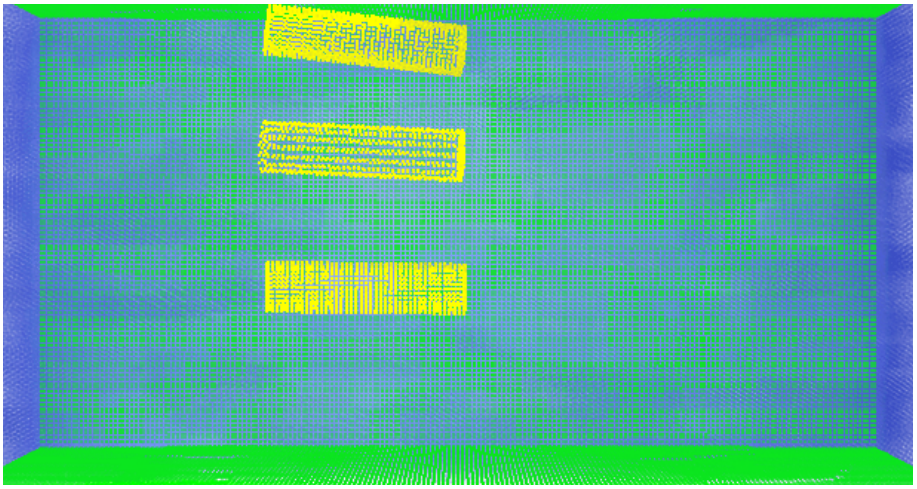

(d) t = 0.51 s

FIGURE 5.2: The snapshots of the simulation's result: the impact of floating body in a rectangular open channel flow at (a) t = 0 s (b) t = 0.25 s (c) t = 0.38 s (d) t = 0.51 s.

5.3 Numerical simulations of the impact of a floating body on a structure during flooding of the Mosel river in Kesten

In this section, the numerical model is applied to investigate the impact of a floating body on any structure during the flooding of the Mosel river. This section is organized as follows. First, the background of this test case is provided. Second, the numerical setup of the scenario is presented. Third, the results of the simulation is discussed. Finally, the impact of the floating body on the structure is further analyzed using Abaqus.

5.3.1 Background of the test case

The Mosel river is a left tributary of the Rhine river that originates from France, passes by Luxembourg, and converges with the Rhine river again in Germany. As with all the other rivers in the world, the Mosel river also tends to flood, especially during spring, when the snow higher up along the stream starts melting. Kesten is a town located along the Mosel river's river, in Rheinland-Pfalz in western Germany, and the town is affected by the flooding of the Mosel river. Several prevention methods, such as flood control walls, flood control dykes, flooding pumphouse, and underground waterproofing with retaining walls have been deployed in Kesten to prevent the flood overflow in the region. Among the the prevention methods mentioned above, the flood control walls, which are deployed for the Mosel river from 138.9 km to 139 km, is one of the most important flood control devices. However, during the floods, floating body such as trees, vehicles, and trash along riverbank may be flushed into the river and transported downstream, and that can potentially hit the water protection devices. This may damage the flood control walls and even deform them, eventually causing a failure to prevent the flood overflow in the region. Therefore, in this section, a simulation scheme suitable for the analysis and prediction of the impact of floating body on the flood control walls by the water management authority is presented. The following section presents a simulation scenario, which

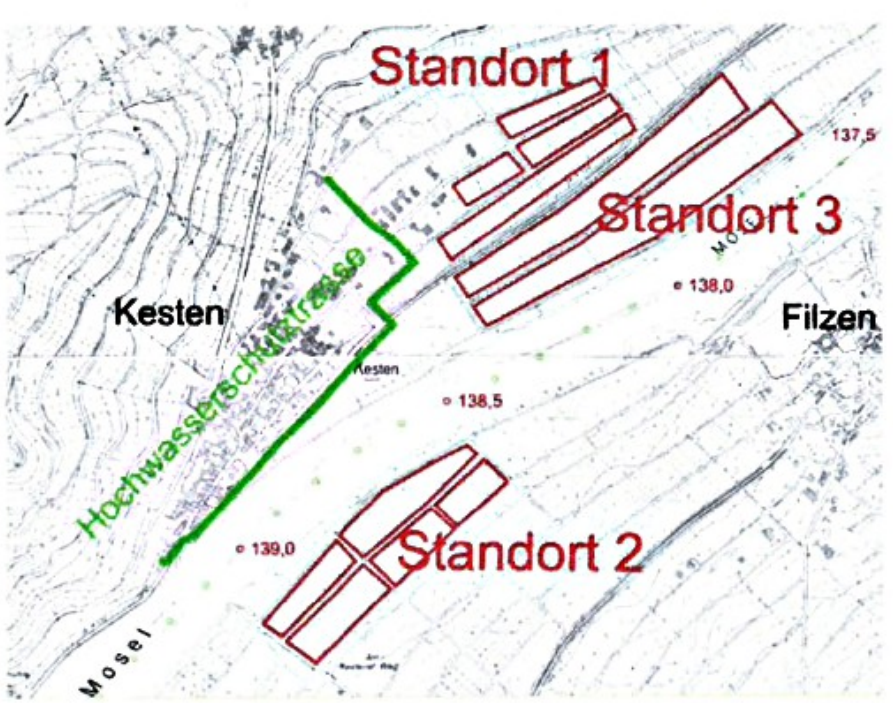

FIGURE 5.3: Map of the Mosel river and Kesten town.

is based on the situation that floating bodies in the Mosel hit the flood protection devices along the river bank. To design a numerical study of current scenario, the following sections are organized as follows. First, the geometrical data of the Mosel river near Kesten is discussed. Second, the numerical setup of the scenario is presented. Third, the result of simulation is presented and discussed. Finally, the impact of the floating body on the flood control wall is further analyzed using Abaqus.

5.3.2 Numerical setup

Fig. 5.4 shows the geometrical setup of the bed of the Mosel river, from 138.9 km to 139.2 km. The blue points in the image represent the measured GPS data and depth of the Mosel river bed. The grey surface represents the surface of riverbed. The brown area is the flood control wall. It can be seen that along the deepest part of every cross section of the channel, the river can be separated to the outer side and the inner side of the river.

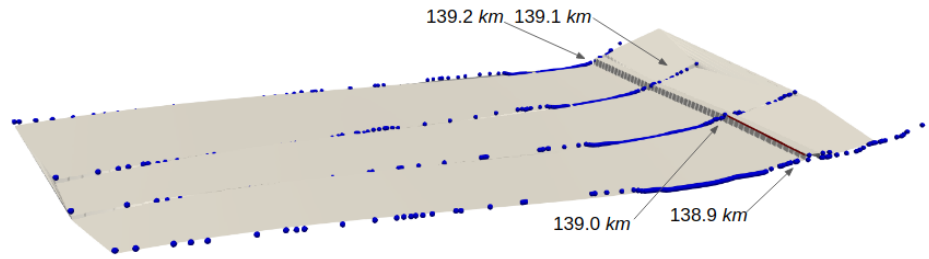

(a)

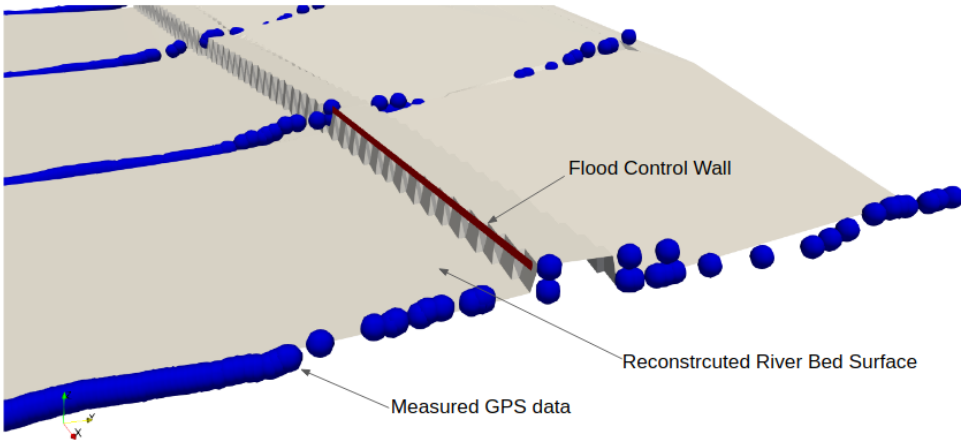

(b)

FIGURE 5.4: The geometry data of the Mosel river (a) from 138.9km to 139.2km (b) from 138.9km to 139.0km. The blue points represent the measured GPS data and depth of the river bed, the grey surface and brown area represent the surface of the river bed and the flood control wall, respectively.

Since Kesten is located on the outer side of the river bank, the flood control wall is deployed at the river cliff on the outer side to prevent any damage caused by flooding. Since the flood control wall is mainly deployed along the river cliff between 138.9 km and 139.0 km of the Mosel river, the simulation scenario will focus on this region.

The GPS data and depth of the riverbed only provide its geometric structure every 100m. Therefore, it is necessary to measure the surface of the river

basin for the simulation. In the current test case, the geometry of the river basin is constructed by interpolating the measured GPS data and depth of 138.9km, 139.0km, 139.1km, and 139.2km. The geometry of the current test case is represented as the grey surface in Fig. 5.4.

The boundary of the simulation is reconstructed based on the interpolated surface of the river bed. Fig. 5.5 illustrates the numerical setup of the current test case, where the blue particles represent the inlet and outlet, the green particles represent the fluid, the red particles represent the boundary, and the purple cylinders are the floating bodies. The uniform inlet velocity condition of 2 m/s in the X-direction is applied to the cross section of 139.0 km, and the fixed pressure outlet condition is applied to the cross section of 138.9 km. The pressure of the outlet is set equal to the static pressure, wherein the pressure is calculated as $p_{outlet} = \rho gh$.

The density of the fluid is set to 1000 kg/m^3. Trees are some of the most common floating body transported along the river during flooding. Therefore, two trees are included as the floating bodies in the current scenario. These trees are represented using cylinders that are of 7 m in height and 0.25 m in radius. Since these floating bodies are trees, their density is set to 750 kg/m^3 and initially placed at (35 m, 354 m, 13 m) and (35 m, 348 m, 13 m) from the origin. In the following section, two test cases are presented. The first test case considers that the floating bodies are moving in X-direction with an initial velocity $V_x = 2$ m/s. In the second test case, the initial velocity of the floating body is set to 2 m/s in X-direction and 3 m/s in the Y-direction.

5.3.3 Results of the test case with floating bodies without the initial velocity in the Y direction

Fig. 5.6 is a snapshot of the simulation results, where the arrows indicate the fluid particle's direction and its colors represent the pressure exerted by the fluid particles. It can be seen that from t = 0 s to t = 0.75 s, a small vortex surrounding both the floating bodies has been forged, resulting in

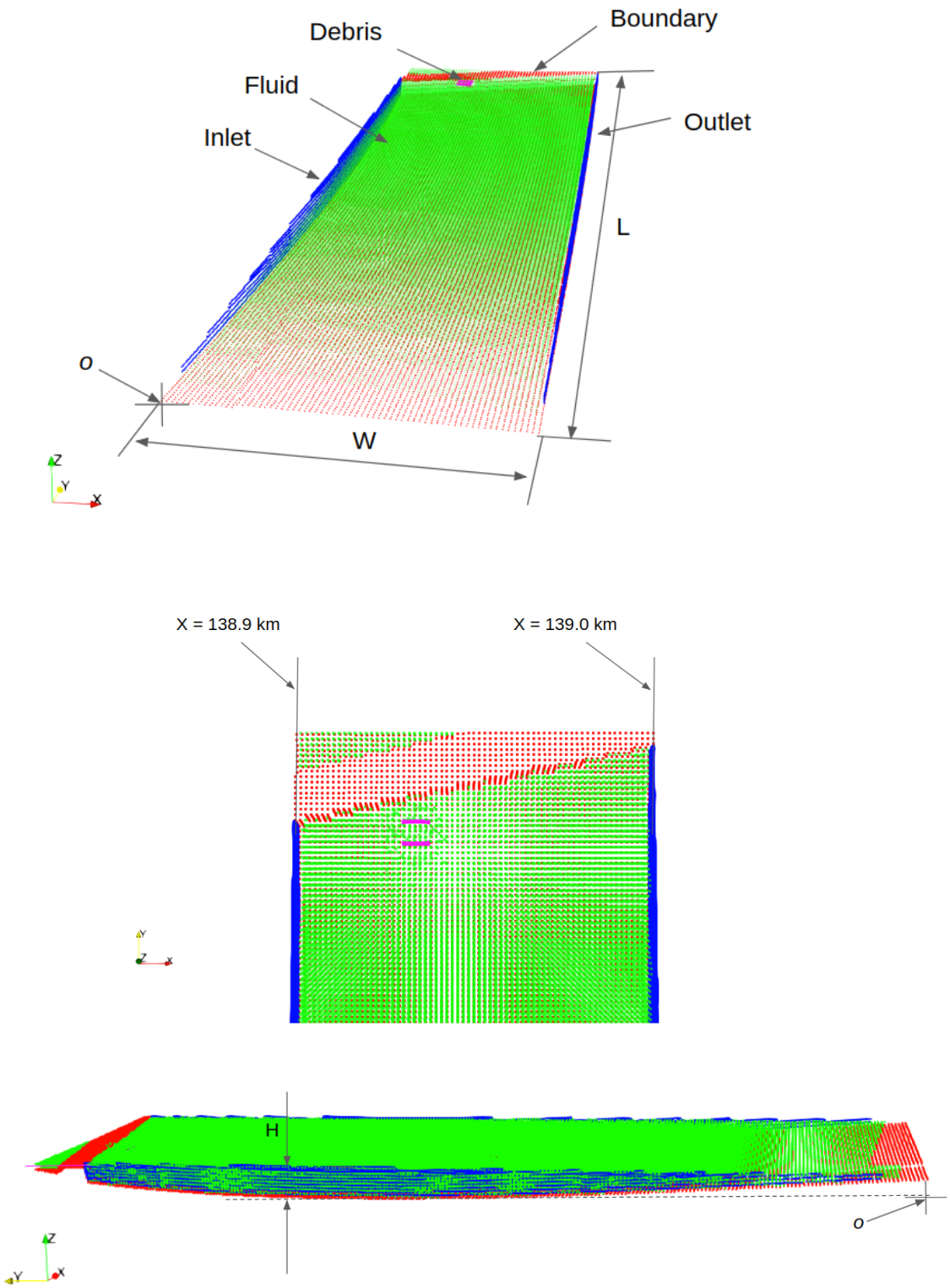

FIGURE 5.5: The discretized SPH model of the impact of a floating body on the structure during the flooding of the Mosel river near Kesten.

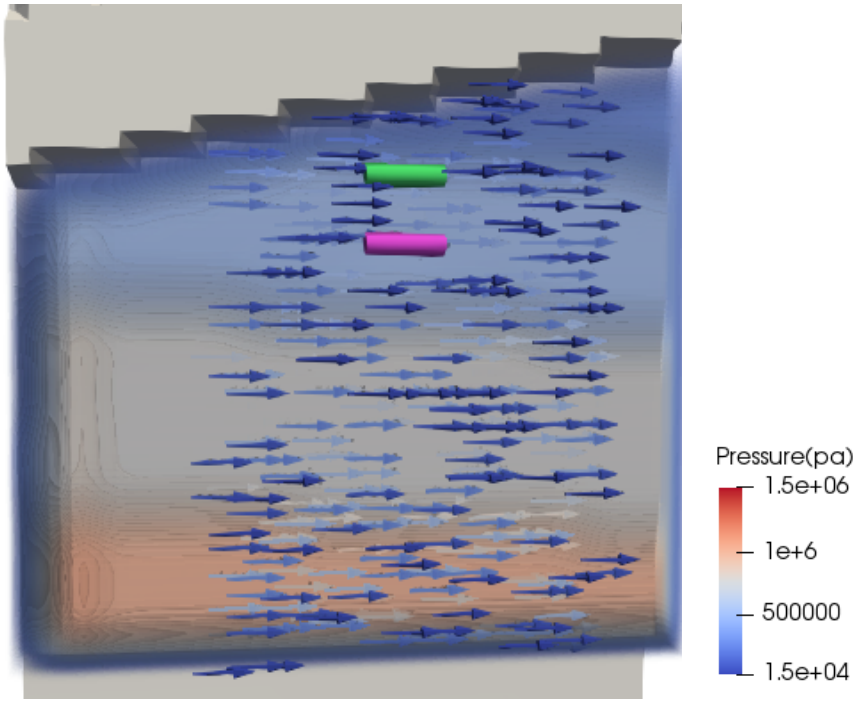

(a)

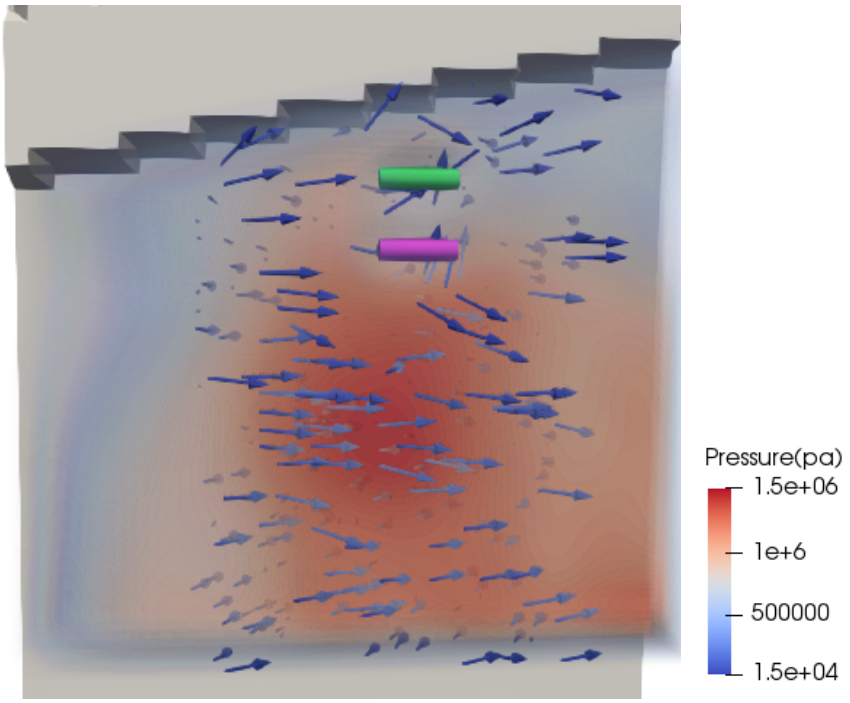

(b)

FIGURE 5.6: The snapshot of the floating bodies without the initial velocity in the Y-direction case at (a) t = 0 s (b) t = 0.75 s (c) t = 1.05s (d) t = 1.65s (e) t = 2.4s (f) t = 2.55s (g) t = 3.33 s (h) t = 6.5 s, where the arrows represent the direction of the fluid particles, while the colors of the contour represent the pressure the flow. (The radius of the cylinders in this figure is increased to 1m for enhanced visualization.)

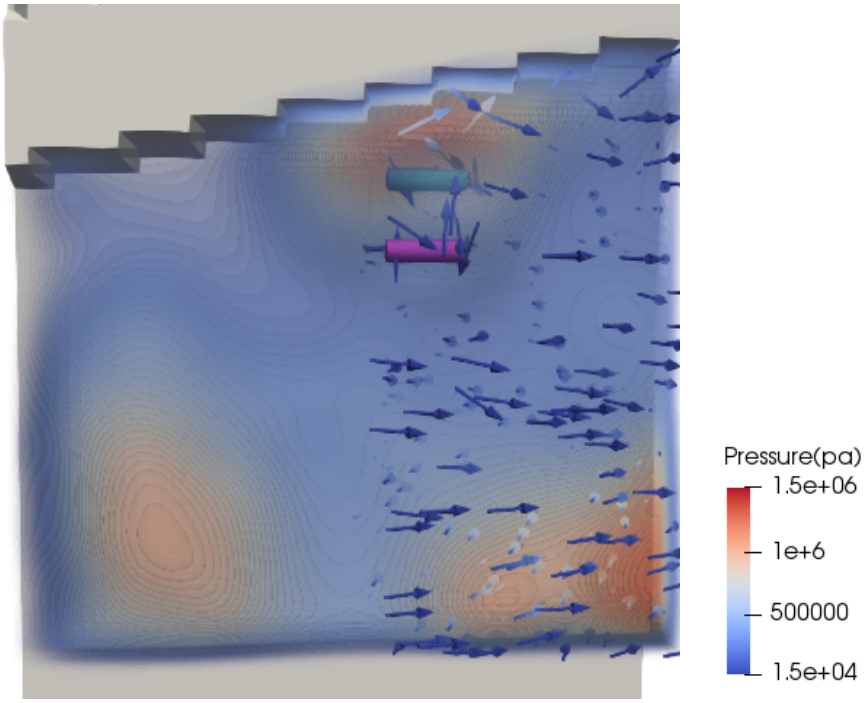

(c)

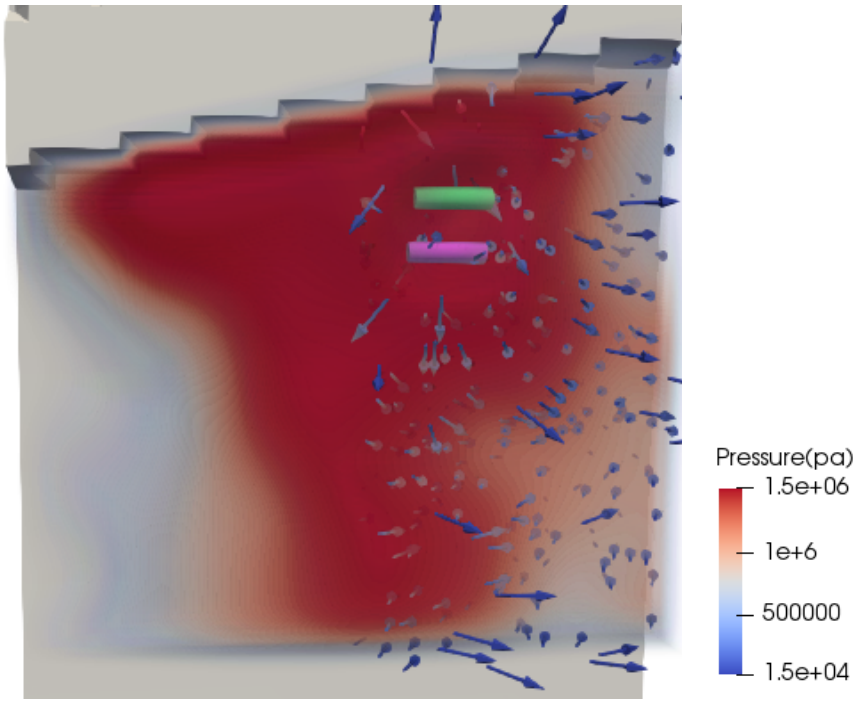

(d)

FIGURE 5.6: The snapshot of the floating bodies without the initial velocity in the Y-direction case at (a) $t = 0s$ (b) $t = 0.75s$ (c) $t = 1.05s$ (d) $t = 1.65s$ (e) $t = 2.4s$ (f) $t = 2.55s$ (g) $t = 3.33s$ (h) $t = 6.5s$, where the arrows represent the direction of the fluid particles, while the colors of the contour represent the pressure the flow. (The radius of the cylinders in this figure is increased to 1m for enhanced visualization.)

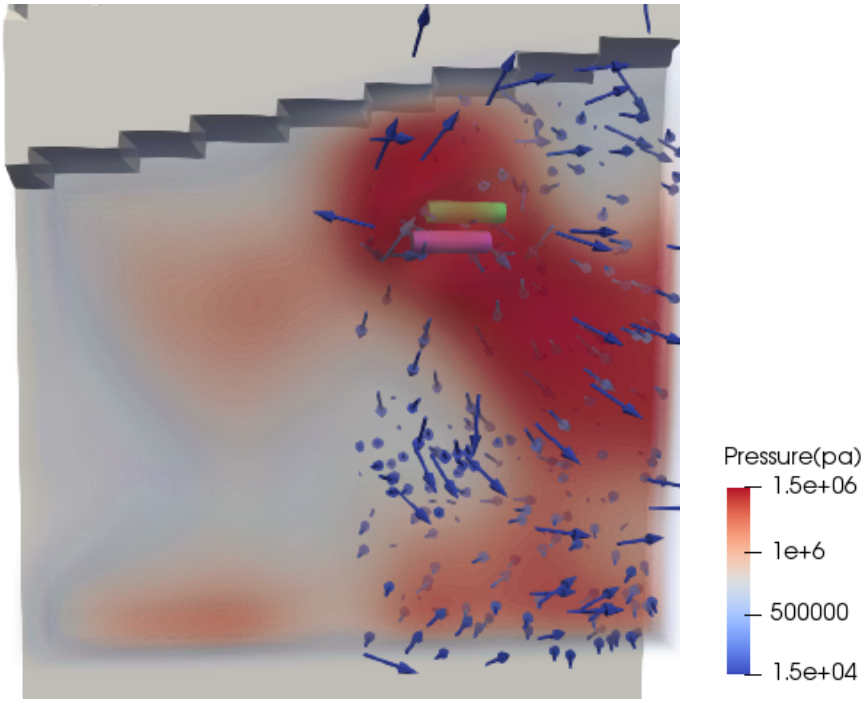

(e)

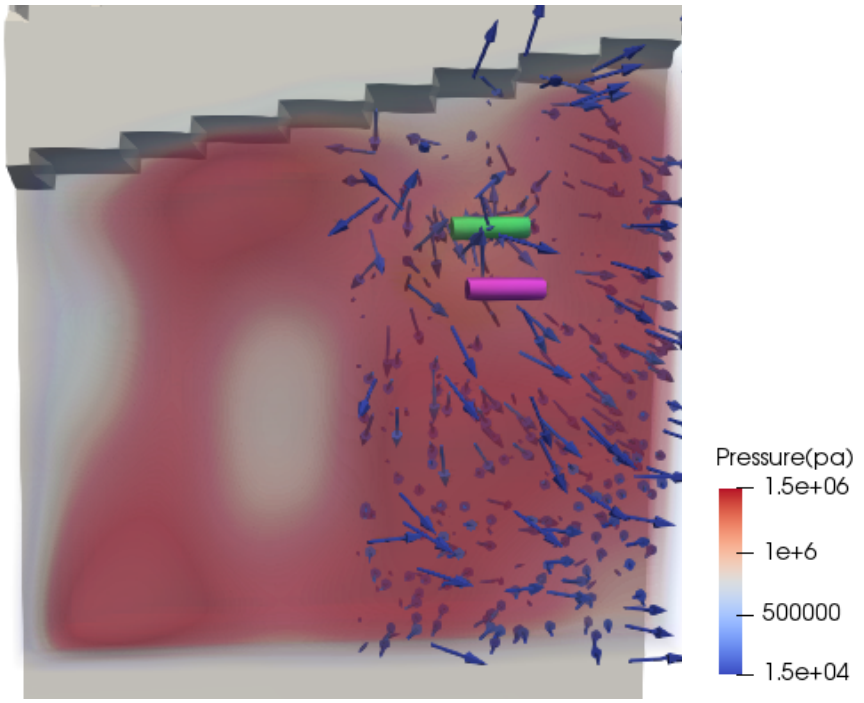

(f)

FIGURE 5.6: The snapshot of the floating bodies without the initial velocity in the Y-direction case at (a) $t = 0s$ (b) $t = 0.75s$ (c) $t = 1.05s$ (d) $t = 1.65s$ (e) $t = 2.4s$ (f) $t = 2.55s$ (g) $t = 3.33s$ (h) $t = 6.5s$, where the arrows represent the direction of the fluid particles, while the colors of the contour represent the pressure the flow. (The radius of the cylinders in this figure is increased to 1m for enhanced visualization.)

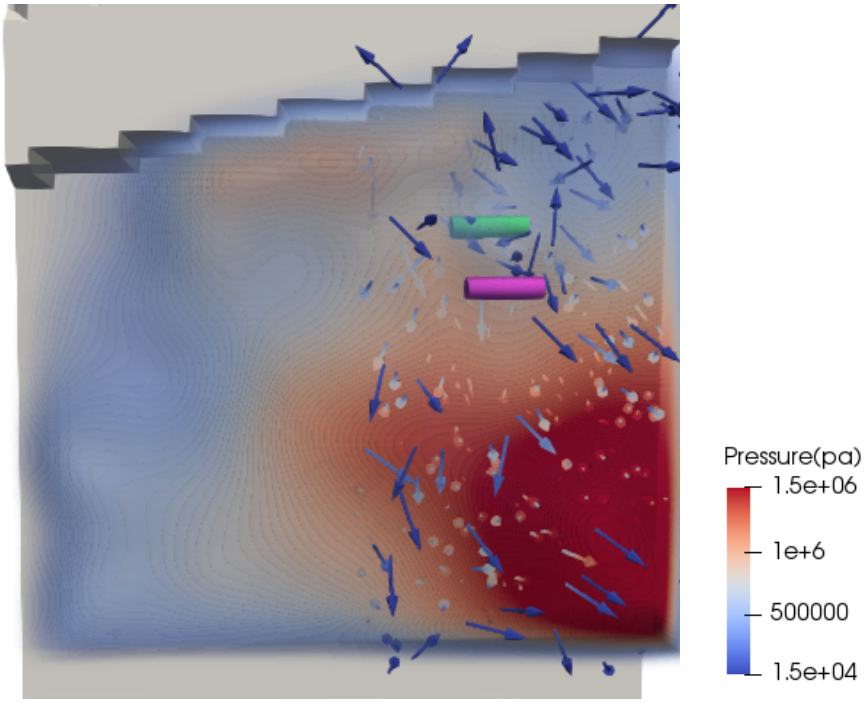

(g)

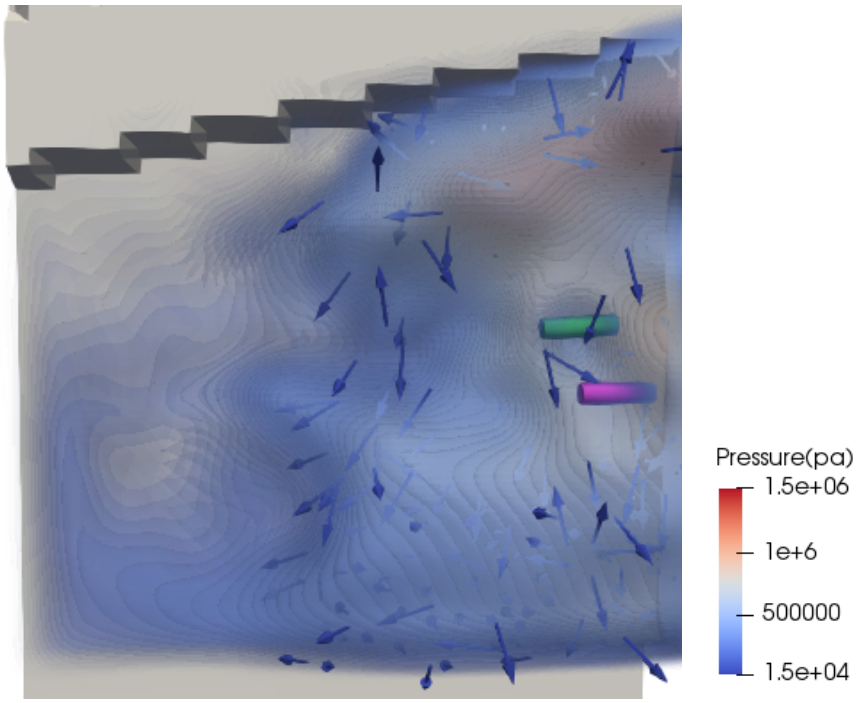

(h)

FIGURE 5.6: The snapshot of the floating bodies without the initial velocity in the Y-direction case at (a) t = 0 s (b) t = 0.75 s (c) t = 1.05 s (d) t = 1.65 s (e) t = 2.4 s (f) t = 2.55 s (g) t = 3.33 s (h) t = 6.5 s, where the arrows represent the direction of the fluid particles, while the colors of the contour represent the pressure the flow. (The radius of the cylinders in this figure is increased to 1m for enhanced visualization.)

the two bodies moving closer to each other. Eventually, a collision occurs between the two floating bodies at t = 2.44 s. Fig. 5.6. (f) shows that due to this collision, the purple floating body starts moving inversely to the river cliff, while the green floating body remains at nearly the same location. This is due to the pressure of the fluid between the green floating body and river cliff being much higher than the other region, which results in the hydrodynamic force that keeps pushing the green floating body to move toward the river bank. After that, both floating bodies keep traveling along the X-direction and never collide with the flood control wall, as shown in Fig. 5.6 (h). As it can be seen that, during the entire simulation, both floating bodies have not collided the with flood control wall along the river cliff, it is not necessary to analyze the impact of floating bodies on the flood control wall. However, this test case does indeed show that the current numerical model is capable of predicting the trajectory of a floating body in rivers during flooding.

5.3.4 Results of the test case with floating bodies, with the initial velocity $V_y = 3m/s$ along the Y-direction

In this section, the initial velocity of the floating bodies are set equal to $V_x = 2m/s$ and $V_y = 3m/s$. Fig. 5.7 is the snapshot of the simulation result of the test case with a static pressure outlet, where the arrows represent the direction of the fluid and the colors of the arrows represent the pressure of the fluid particles. It can be seen that at $t = 0.9s$, both the floating bodies were moving toward the river cliff. Since the green floating body was moving toward the river cliff, the fluid between the green floating body and the river cliff is compressed, creating a region of higher pressure between the green floating body and the river cliff. Moreover, due to this pressure being higher than the pressure between the green floating body and purple floating body, the green floating body was impacted by a stronger hydrodynamic force in the negative Y-direction. This eventually stops the green floating body

from moving in the Y-direction, and it starts to translate in the negative Y-direction at t = 1.2 s. However, at t = 2.4 s, the two floating bodies collide at (39.7487 m, 354.4963 m, 11.8182 m) from the origin of the numerical setup. Due to this collision, the green floating body starts moving toward the river cliff again, while the purple floating body starts moving toward the direction opposite the river cliff. The green floating body eventually collides with the river cliff at t = 3.5 s and (x, y, z) = (47.517 m, 363.919 m, 12.757 m). During the collision, the center of gravity of the green floating body is at (x, y, z) = (48.3318 m, 360.65 m, 11.81 m). The impact velocity of the floating body is $(6.22, 3.21, 0.0276)$ with the unit meter per second and the impact velocity magnitude being 7 m/s. It is worth to mention that the initial design of the flood control wall can only withstand a maximum impact velocity of 3 m/s (Bund der Ingenieure für Wasserwirtschaft and Pasche, 2005). The result of the current simulation shows that the SPH-DEM model is capable of capturing the impact of the floating bodies on the structure. This impact velocity obtained from the current model is extracted to design a finite-element simulation for the analysis of the impact on the structure caused by the floating body in the next section.

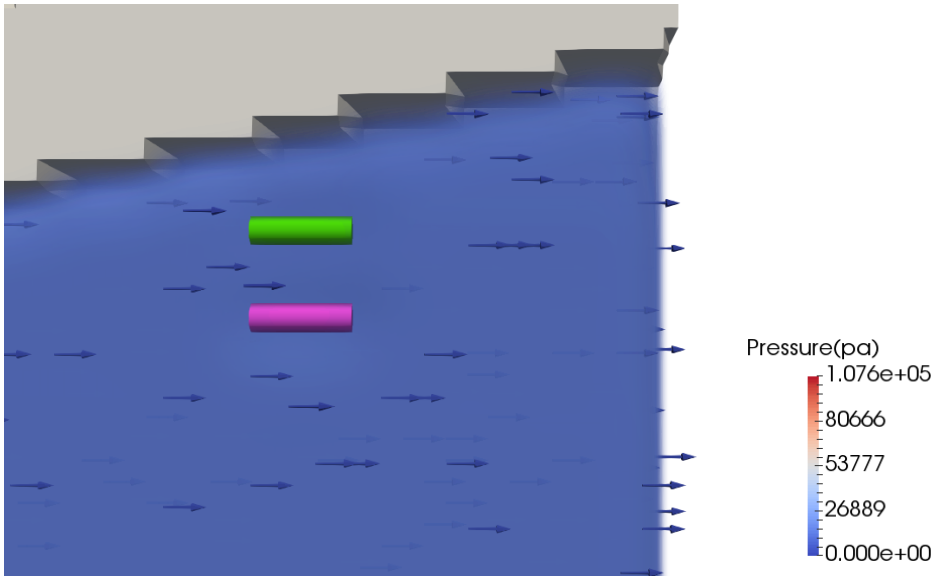

(a)

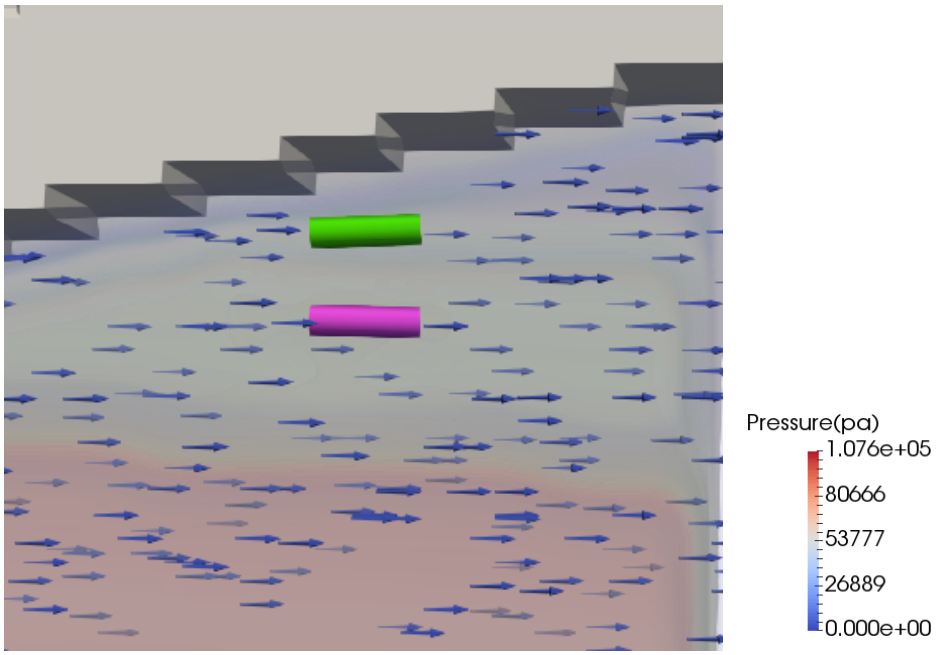

(b)

FIGURE 5.7: The snapshot of the floating bodies with the initial velocity in the Y-direction case at (a) t = 0 s (b) t = 0.9 s (c) t = 1.2 s (d) t = 2.4 s (e) t = 3.5 s , where the arrows represent the direction of the fluid particles, while the colors of the contour represent the pressure the flow. (The radius of the cylinders in this figure is increased to 1m for enhanced visualization.)

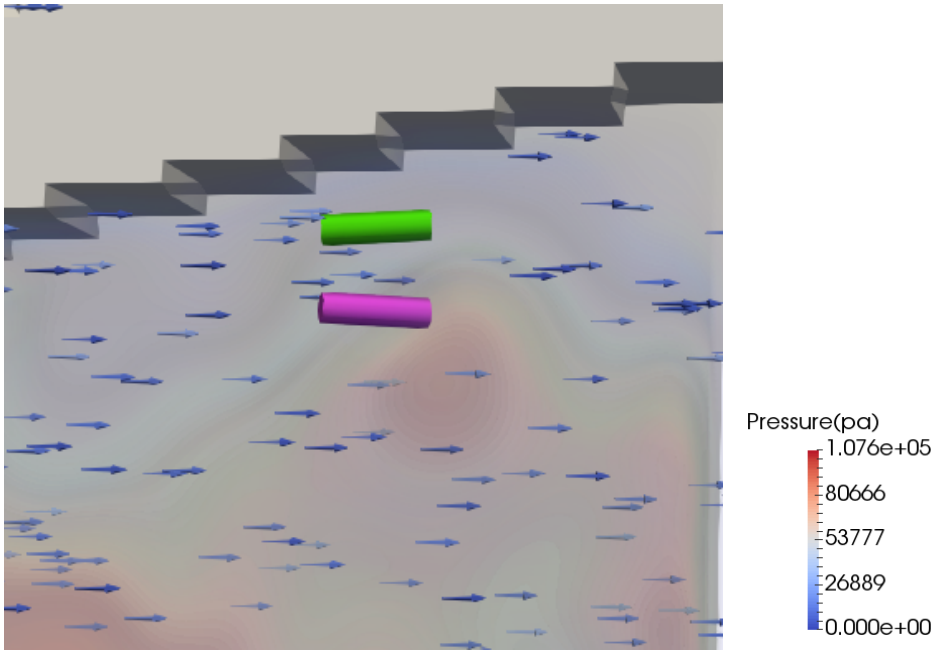

(c)

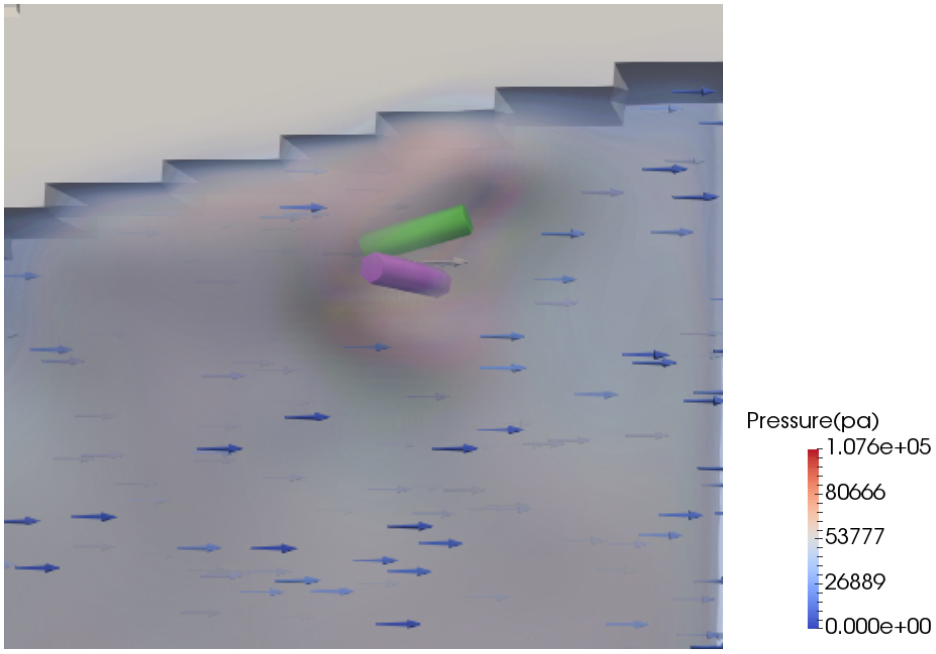

(d)

FIGURE 5.7: The snapshot of the floating bodies with the initial velocity in the Y-direction case at (a) $t = 0s$ (b) $t = 0.9s$ (c) $t = 1.2s$ (d) $t = 2.4s$ (e) $t = 3.5s$, where the arrows represent the direction of the fluid particles, while the colors of the contour represent the pressure the flow. (The radius of the cylinders in this figure is increased to 1m for enhanced visualization.)

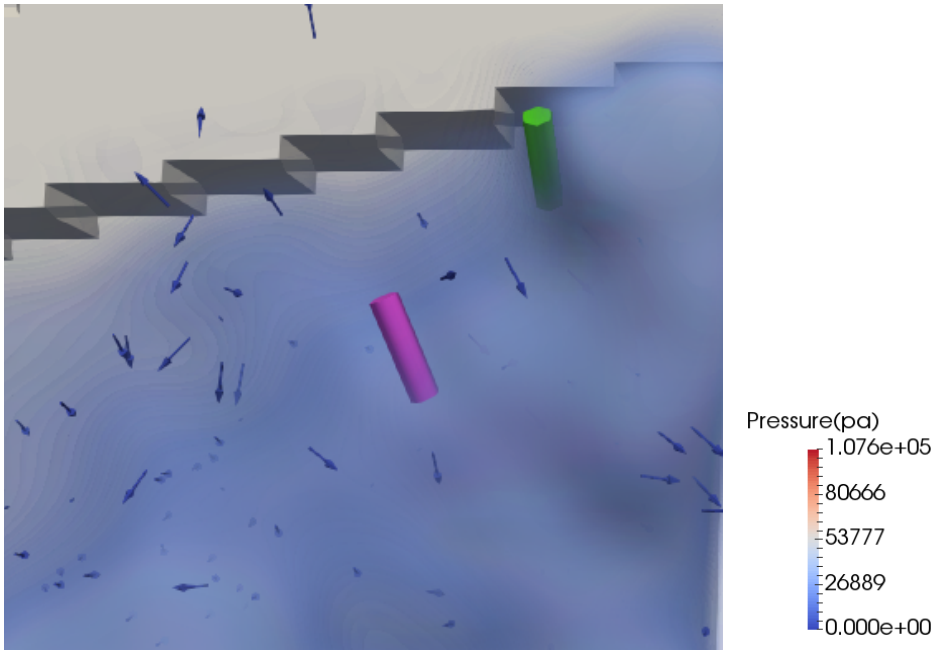

(e)

FIGURE 5.7: The snapshot of the floating bodies with the initial velocity in the Y-direction case at (a) $t = 0s$ (b) $t = 0.9s$ (c) $t = 1.2s$ (d) $t = 2.4s$ (e) $t = 3.5s$, where the arrows represent the direction of the fluid particles, while the colors of the contour represent the pressure the flow. (The radius of the cylinders in this figure is increased to 1m for enhanced visualization.)

5.3.5 Analysis for the deformation of the structure on impact

To further investigate the impact and analyze the damage caused to the structure, as the scenario in the previous section showed, the commercial FEM software Abaqus is applied.
Fig. 5.8 is a sketch of the flood control wall that is deployed along the Mosel river from 138.9 km to 139.0 km. The flood control wall is 2.5 m in width and 2.05 m in height. Between each flood control wall, there is a pillar to hold the walls up. Fig. 5.8 shows that the thickness of the flood control wall is 20 cm. Furthermore, the flooding wall actually consists of a thin layer of Aluminum that is 3 mm in thickness. The numerical setup of the current test case is represented in Fig. 5.9. The main purpose of the pillar is to hold up the flood control wall, the encastre boundary condition, which means that there are no displacements in any direction, is applied on both sides of the flood control wall. Aluminum 6061-T6 is a commonly used material for flood control wall, so this section applies its properties to the simulated flood control walls. The mechanical properties of Aluminum 6061-T6 are presented in Table 5.1.

TABLE 5.1: Mechanical Properties of Aluminum 6063-T5.

Properties	Metric
Density	2.7 g/cm^3
Young's modulus	70 GPa
Tensile strength	276 MPa
Poisson's ratio	0.33

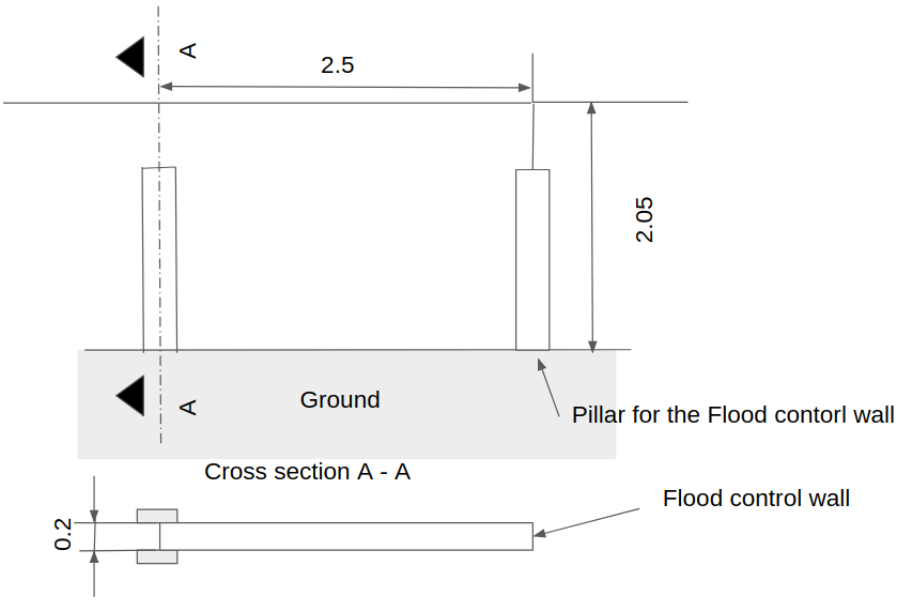

FIGURE 5.8: A sketch of the flood control wall (unit in meters).

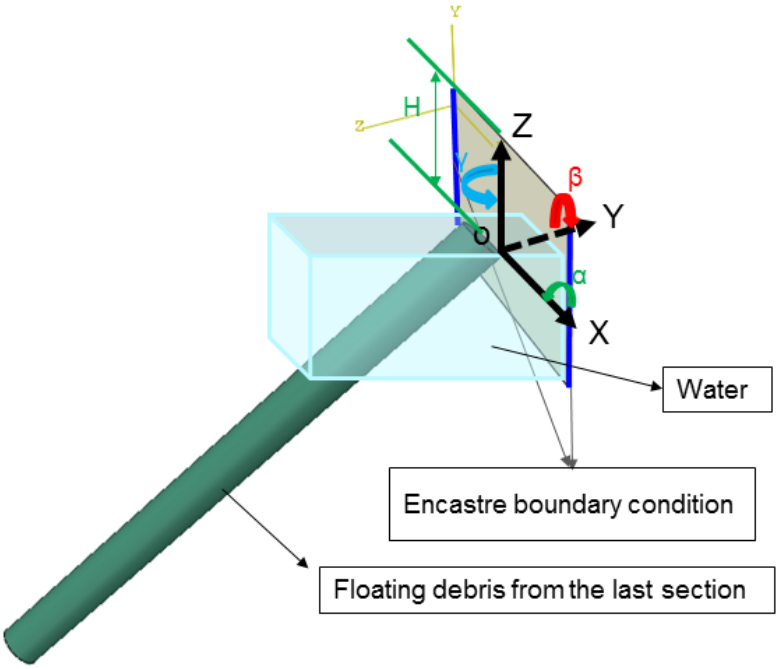

FIGURE 5.9: A sketch of the numerical setup for Abaqus in the current work. The green cylinder represents the floating body, while the gray wall represents the flood control wall. The encastre boundary condition is applied to the blue line of the wall.

The floating bodies in the last section are considered to be trees, but this section only focuses on the impact of the side of the flood control wall. Thus, for the sake of simplicity, this section assumes that the floating body is rigid with uniform density 750 kg/m^3. The initial velocity of the floating body is $(6.22\ m/s, 3.21\ m/s, 0.0275\ m/s)$, which means the impact velocity at normal direction is 3.21 m/s. Fig 5.10 shows the impact load time history of the current numerical model. It is shown that the maximum impact load is 166.064 kN, which happens at 0.033 second after the initial impact. The duration of the impact is 0.063 second. Table 5.2 shows the comparison of the maximum impact load between current work and impact load obtained by using the design codes that is mentioned in section 2.2.4. In the method

suggested by FEMA to calculate the impact load, it is necessary to provide the suitable contact duration time. However, the contact duration between wood and aluminum is not available. Therefore, the contact duration time of the steel wall is adopted. Consequently, the impact load calculated by the method suggested by FEMA is 26.250 kN. Apparently, this value is much lower than the value obtained by the numerical model in the current work. This is due to the fact that the contact duration time of steel (0.2s) suggested by FEMA is not suitable for the current scenario.

Since contact duration of the impact for steel suggested by FEMA is not suitable for Aluminum 6061-T6. It is possible to apply the contact duration obtained from the numerical model. The impact load obtained by using the method of FEMA and contact duration time obtained by the current numerical model is 83.333 kN. Which is much closer to the value obtained by the current numerical model. However, there is still a huge gap between the impact load obtaining from the current numerical model and the method suggested by FEMA. This is due to in the method of FEMA, the floating body is assumed to impact the structures with its horizontal position. While in the current scenario, the floating body impacted the flood control wall with an angle. Consequently, the impact load obtained from the current work is larger than the one obtained from the FEMA.

The impact load obtained by using the method suggested by AASHTO (section 2.2.4.1) is 23.3877 kN, which is much lower than the result obtained from the current work – this is due to how the original method is constructed; based on the collision between ship and pier. For calculating the impact load by using the method suggested by AS5100 (2004) (section 2.2.4.3), it is necessary to know the stopping distance, however, the stopping distance for Aluminum 6063-T5 is not provided. Therefore, the stopping distance obtained from the current numerical simulation is employed to calculate the impact load through the method of AS5100 (2004). The result of the impact load of AS5100 (2004) in the current scenario is 148.217 kN. This value is slightly lower than the one obtained from the current numerical model. One of the main reasons of this difference is that the formulation of AS5100 (2004) is established based on considering the 2 metric-tons log, while in

the current scenario, the floating body is only 750 kg in weight. Using the method of design codes for calculating impact load may underestimate the real impact load. Moreover, many parameters, such as contact duration of FEMA and stopping distance of AS5100 (2004), are unavailable. As a result, the methods for estimating the impact loads provided by the design codes are not suitable for the scenario in the current work.

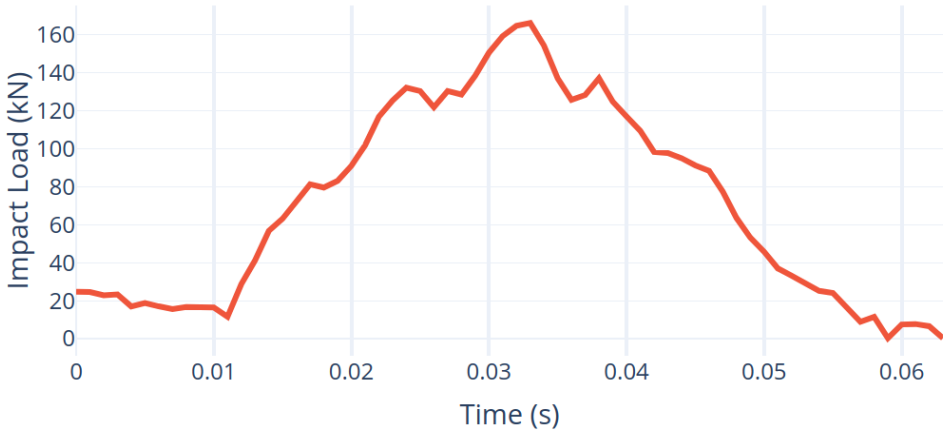

FIGURE 5.10: The impact load-time curve obtained from the current work.

TABLE 5.2: The comparison of the maximum impact loads obtained between the current work and using the design codes.

Model	Maximum Impact Load
Numerical Results (Current Work)	166.064 kN
FEMA($t_{Duration} = 0.2s$)	26.250 kN
FEMA($t_{Duration} = 0.063s$)	83.333 kN
AASHTO	23.3877 kN
NAASRA (Stopping Distances = 0.3 m)	122.500 kN

To analyze the damage caused by the impact of the floating body, the JC material model (Johnson and Cook, 1983, 1985) and Johnson-Cook failure

model (Johnson and Cook, 1985) is employed in the current work. The JC model is given as

$$Y = [A + B\epsilon_p^n][1 + Cln(\frac{\epsilon_p}{\epsilon_0})][1 - \frac{T - T_{room}}{T_{melt} - T_{room}}] \tag{5.1}$$

where Y is effective yield stress ϵ_p is effective plastic strain rate, ϵ_0 is reference strain rate, T_{room} is room temperature of material and T_{melt} is the melting temperature of material, A is initial yield stress, B is hardening constant, C is strain rate constant, n is hardening exponent and m is thermal softening exponent. The parameters of JC model for Aluminum 6061-T6 are given in Table 5.3. The Johnson-Cook failure model is one of the most popular model to analyze ductile failure. The Johnson-Cook failure model is given as:

$$\textbf{Damage} = \sum \frac{\delta\epsilon_p}{\epsilon_f} \tag{5.2}$$

where ϵ_f is equivalent strain at failure. The material is assumed to be intact until the **Damage** > 1. The ϵ_f is given as:

$$\epsilon_f = [D_1 + D_2 exp(D_3\sigma^*)][1 + D_4 ln(\frac{\epsilon_p}{\epsilon_0})][1 + D_5\frac{T - T_{room}}{T_{melt} - T_{room}}] \tag{5.3}$$

where $D_1 - D_5$ are constant, σ^* is mean stress normalized by the effective stress. The parameters of Johnson-Cook Failure model for Aluminum 6061-T6 are given in Table 5.4.

Fig. 5.11 and Fig. 5.12 visualize the results of the deformation of the flood control wall after the impact of the floating body. Fig. 5.11 (b) shows that, the kinetic energy of the floating body was absorbed by the flood control wall, which in result the flood control wall experienced the deformation. It can be seen from FIG. 5.12 (b), the deformation of flood control wall exceeded the limit of elastic deformation of its material, which eventually leaded to the failure of the material and the appearance of cracks. It can be seen that the flood control wall is damaged by the impact of the floating

body, Which means that the flood control wall will not survive a collision with floating bodies in the current scenario.

As the results indicated using the current numerical model, if such a scenario did occur in the real world, the flood control wall would not be capable of preventing the river overflowing and flooding Kesten.

TABLE 5.3: Parameters of the Johnson–Cook material model for Aluminum 6061-T6 (Lesuer, 1999).

A	324 MPa
B	114 MPa
C	0.002
n	0.42
m	1.34

TABLE 5.4: The constants of Johnson–Cook damage model for Aluminum 6061-T6 (Lesuer, 1999).

Initial failure strain, D_1	-0.77
Exponential factor, D_2	1.45
Triaxiality factor, D_3	-0.47
Strain rate factor, D_4	0.0
Temperature factor, D_5	1.6
T_{room}	20°C
T_{melt}	650°C

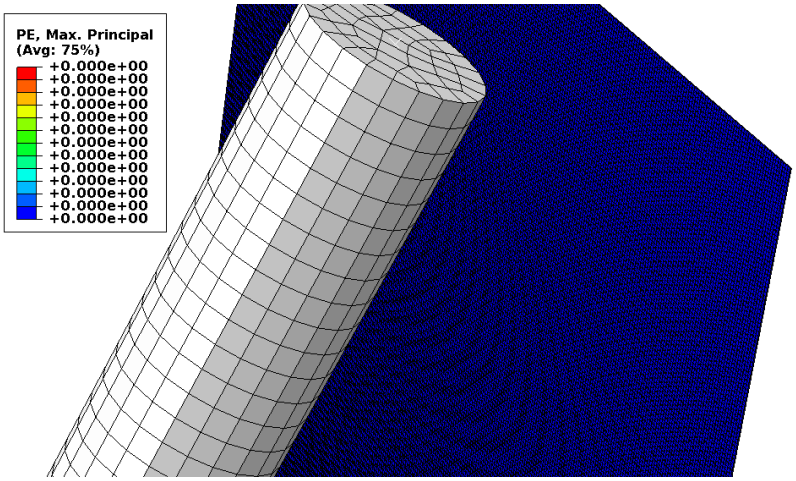

(a)

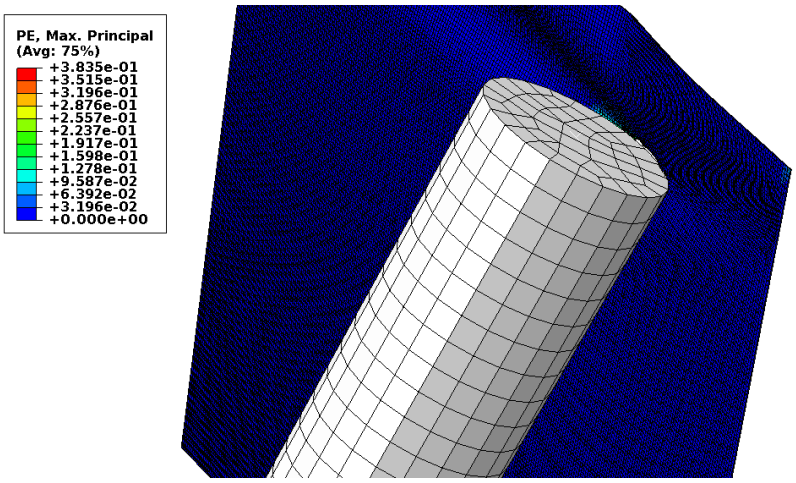

(b)

FIGURE 5.11: Snapshots and contours of plastic strain of the flood control wall from the view of the impact side (a) before impact and (b) after impact.

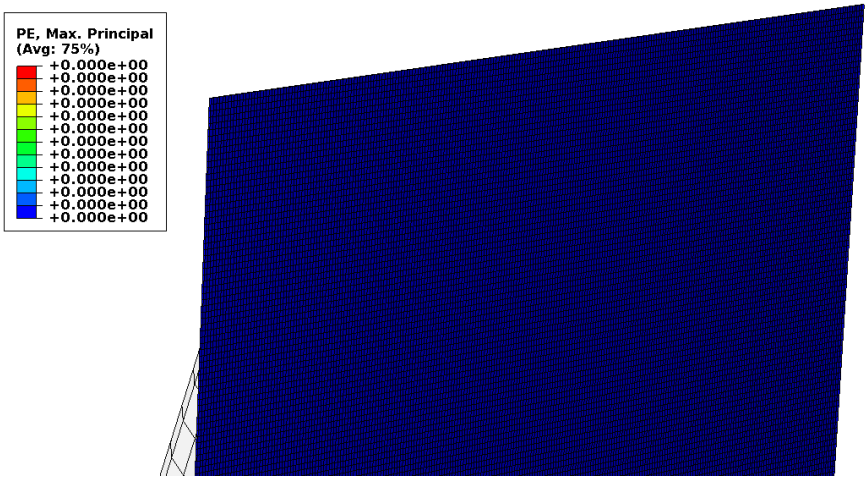

(a)

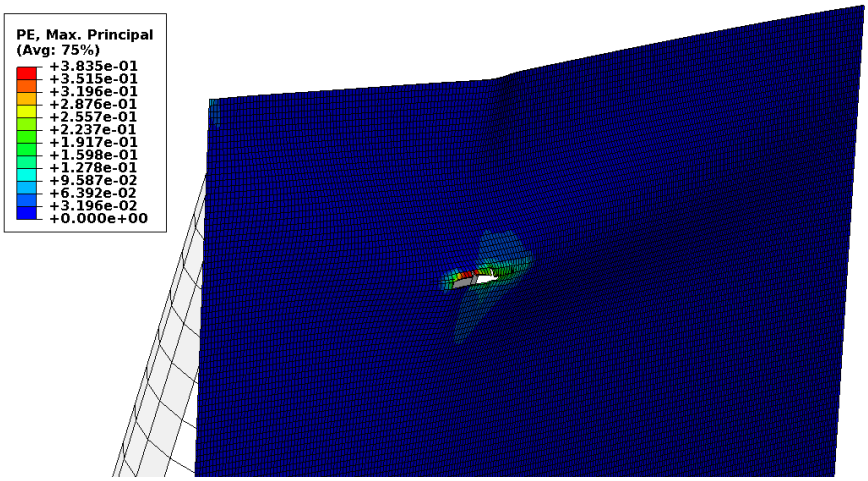

(b)

FIGURE 5.12: Snapshots and contours of plastic strain of the flood control wall from the view of the opposite side of the impact side (a) before impact and (b) after impact.

Chapter 6

Conclusion and Future Work

6.1 Conclusion

This research project was conducted to design a numerical tool that is suitable to analyze the impact of floating bodies on a structure during flooding.

This thesis presented an lagrangian meshless SPH-DEM model to simulate the interaction between floating bodies and free surface flows and the interaction between floating bodies and structures. Various test cases were conducted in this thesis, which proved that the current the SPH-DEM model is appropriate and applicable to simulate the interaction between arbitrary floating bodies and flow, tracking the trajectory of a floating body and capture wave collision with structures. In which the traditional methods, i.e., analytical methods and empirical methods, of analyzing the impact of floating bodies on the structures during flooding are not capable of dealing with the interaction between floating bodies and flooding. Moreover, traditional methods are not capable of tracking the trajectory of a floating body during such floods. Traditional methods are also limited to simple geometries of floating bodies and structures. In addition, the wave force and hydrodynamic forces applied to a structure during flooding are difficult to analyze using traditional methods.

In this thesis, an open boundary method developed by Ferrand et al. (2017) for 2D work was extended to 3D, in which there is still a lack of proper open boundary treatment for the SPH in the literature.. A simple rectangular duct flow test case was used to validate the current open boundary method. This shows that the current open boundary method has only 3% difference in terms of the maximum velocity when compared to the theoretical model. This means that the current open boundary method is highly appropriate to be applied to the 3D SPH model. Which is to simulate the flooding, it was necessary to have a proper open boundary condition to be applied at the inlet and outlet.

The numerical model presented in the current work is coupled with the Abaqus, a commercial FEM software, to further analysis the impact of the floating bodies on the structures. A real world scenario is presented in the thesis to demonstrate that the current numerical model is suitable to analyze the impact of floating bodies on a structure, such as flood walls, during flooding. The test case is based on the floating trees, transported down the Mosel river near Kesten, located in the west of Germany. Moreover, the objective of this test case was to predict the damage caused by floating bodies on the flood control wall that is deployed at the river cliff of the Mosel river in Kesten. The result of the test case shows that the current SPH-DEM model is capable of simulating the dynamics of the floating bodies in the flooding river. It was able to capture the impact between the floating bodies and the solid structure. After capturing this, the commercial FEM software Abaqus was applied to investigate the damage of the structure caused by the floating bodies. According to the results presented in this thesis, it is highly possible that in an instance where a floating tree collides with the food control wall, it could cause damage to the wall or potentially destroy it.

6.2 Future Work

It will be invaluable to extend the work presented in this thesis as described in this section.

6.2.1 Adaptive Particle Refinement (APR)

In the current numerical model, a very fine particle resolution is required to accurately capture the impact between the floating body and the structure as well as the interaction between the flow and floating body. This leads to a very fine particle resolution being adopted throughout the computational domain and increases the computational cost. In order to reduce the computational cost while maintaining the accuracy of the simulation, it is advisable to implement the Adaptive Particle Refinement (APR) feature (Vacondio et al., 2013), allowing a variable particle resolution in the domain.

6.2.2 Turbulent Model

The numerical model in this work can capture the impact between a floating body and a structure and the trajectory of the floating body along the flow. However, the flow of the current work is assumed to be a laminar flow, whereas most floods in the nature are turbulent. Therefore, it is recommended to implement the turbulent model in the future.

6.2.3 2-way coupling with FEM

In the current work, the FEM is applied to predict the deformation of the structure due to the hydrodynamic forces and the impact of floating bodies. However, this is only a one-way coupling, in which the fluid in the current model does not experience the deformation of the structure. Consequently, the current model is not capable of predicting leakages due to the deformation of the structure. Therefore, it will be invaluable to extend the

application of one-way coupling with FEM to two-way coupling with FEM in the current model.

Appendix A

Appendices

A.1 Algorithm for the analytical computation of γ and $\nabla\gamma$ in 3-D

The boundary of three dimensional geometry is two dimensional. To discretize the boundary, the most basic bounded two-dimensional element is the triangular element, which can be represented by 3 co-planer vertices. As Eq. 3.29 shows, when the boundary is discretized by triangular element, then the analytical function of $\nabla\gamma$ is calculated as the integral of the kernel function over a triangle. However, the kernel support domain of the kernel function is a sphere and the integration of the intersection of an arbitrary triangle and the sphere is not over complicated. Therefore, Mayrhofer et al. (2015b) decided to decompose the surface integration domain to 8 possible configurations, as shown in Fig. A.2, to find an analytical solution of $\nabla\gamma$. These 8 possible configurations could be assembled by using the circular sector, circular segment and full circle as Fig. A.2 shown. Moreover, a circular segment could be assembled by 2 circular sectors and a full circle could be assembled by 2 circular segments. Following Mayrhofer et al. (2015b)'s work, the $\nabla\gamma$ in a circular sector can be calculated as follows

$$\nabla\gamma = \left(\int_q^R w(q)(\theta - \arcsin\frac{r\sin\theta}{\sqrt{q^2-d^2}})qdq \right) n_s \tag{A.1}$$

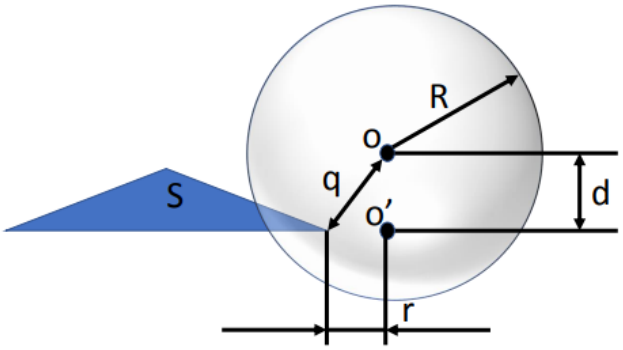

(a)

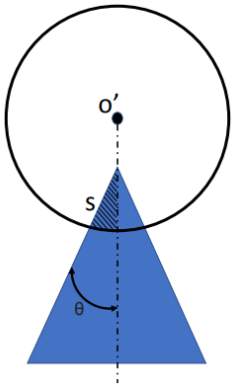

(b)

FIGURE A.1: Illustration of the intersection of support domain, shown as a sphere, and a triangular element (a) 3D (b) project support domain onto the co-planer of the triangular element.

The above formula is valid for $0 < \theta < /2{,}0 \leq r \leq 2$ and $0 \leq d \leq 2$. Where R is the radius of support domain, θ is the angle of the circular sector as Fig. A.1 (b) shown, r is the closest distance between a circular sector and the projected center of the support domain and d is the distance between the co-planer of the circular center and center of the support domain. q is the distance from the center of the support domain to the closet vertex of

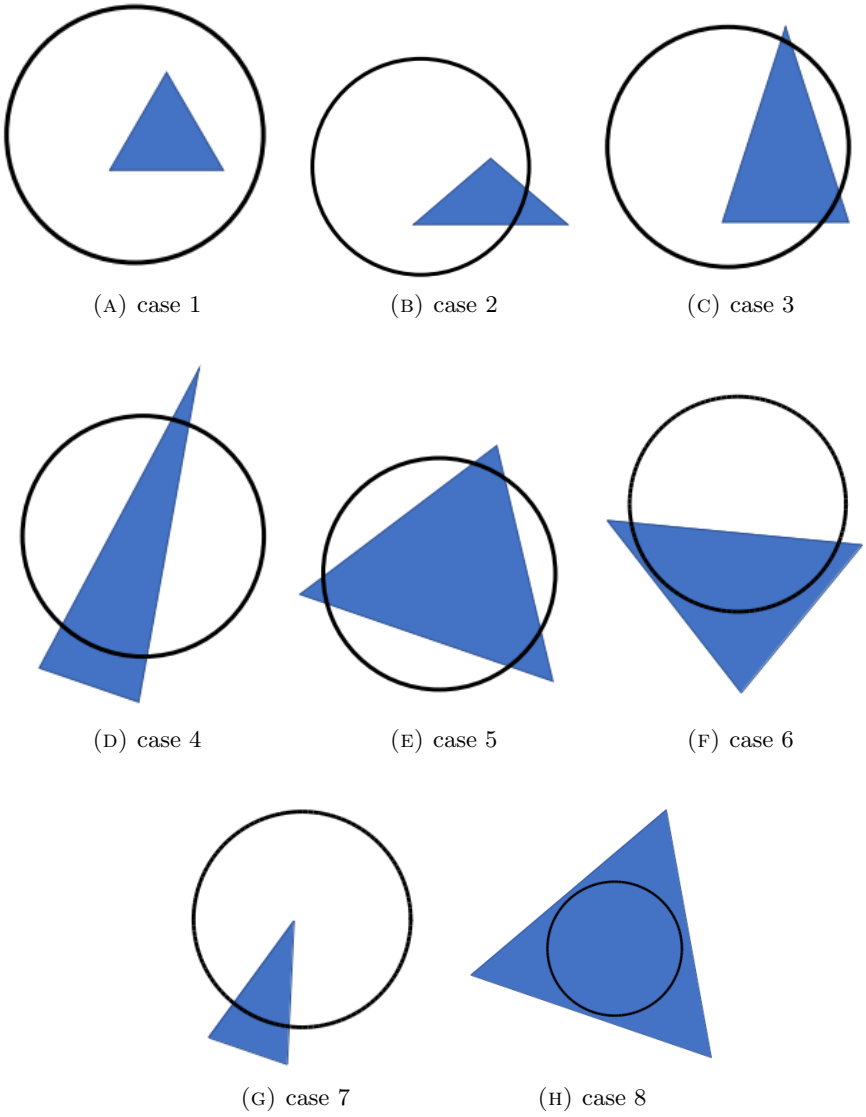

(A) case 1 (B) case 2 (C) case 3

(D) case 4 (E) case 5 (F) case 6

(G) case 7 (H) case 8

FIGURE A.2: 8 possible configurations of domain decomposition.

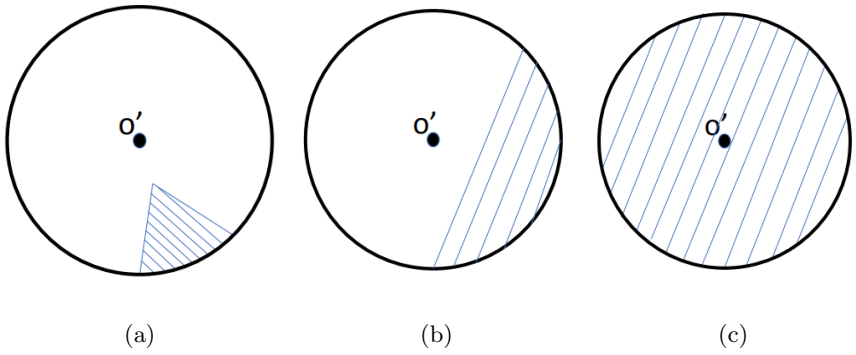

FIGURE A.3: Illustration of the (a) circular sector (b) circular segment and (c) full circle that can be used to calculate $\nabla\gamma$.

the circular sector, which can be calculated as follows

$$q = \sqrt{r^2 + d^2} \tag{A.2}$$

It is worth noting that the above equation is not suitable for kernel functions constructed based on Gaussian functions, because there are no analytical solutions available, as indicated by Fayed and Atiya (2014). The author tries to calculate the $\nabla\gamma$ by using pieces-wise kernel function, such as cubic kernel. However, due to the pieces-wise kernel function has to consider multiple function in one integration, the results are too complicated to be implemented in code. After obtaining $\nabla\gamma$, one can easily obtain γ with the following equation

$$\gamma = \int_q^R \nabla\gamma dq \tag{A.3}$$

Bibliography

AASHTO. *AASHTO LRFD Bridge Design Specifications Set: (Metric Units)*. Bridges and Structures Series. American Association of State Highway & Transportation Officials, 1997. ISBN 9781560510871.

S. Adami, X. Y. Hu, and N. A. Adams. A generalized wall boundary condition for smoothed particle hydrodynamics. *Journal of Computational Physics*, 231(21):7057–7075, 2012. ISSN 00219991. doi: 10.1016/j.jcp.2012.05.005.

M. Antuono, A. Colagrossi, S. Marrone, and D. Molteni. Free-surface flows solved by means of SPH schemes with numerical diffusive terms. *Computer Physics Communications*, 181:532–549, 2010.

AS5100. *Bridge Design: Scope and general principles (AS 5100.1-2004)*. AUSTROADS publication. Standards Association of Australia and Australasian Railway Association and Austroads, 2004. ISBN 9780733756276.

ASCE. *Minimum Design Loads and Associated Criteria for Buildings and Other Structures*. ASCE Standard - ASCE/SEI. American Society of Civil Engineers, 2017. ISBN 9780784414248.

F. Blondel, B. Audebert, T. Pasutto, and M. Stanciu. Condensation models and boundary conditions for non-equilibrium wet steam flows. *International Journal on Finite Volumes*, pages http–www, 2013.

B. Bouscasse, A. Colagrossi, S. Marrone, and M. Antuono. Nonlinear water wave interaction with floating bodies in SPH. *Journal of Fluids and Structures*, 42:112–129, 2013.

A. u. K. Bund der Ingenieure für Wasserwirtschaft and E. Pasche. *Mobile Hochwasserschutzsysteme: Grundlagen für Planung und Einsatz*. BWK-Merkblatt. BWK, 2005. ISBN 9783936015195.

A. Calderer, S. Kang, and F. Sotiropoulos. Level set immersed boundary method for coupled simulation of air/water interaction with complex floating structures. *Journal of Computational Physics*, 277:201–227, 2014. ISSN 10902716. doi: 10.1016/j.jcp.2014.08.010. URL http://dx.doi.org/10.1016/j.jcp.2014.08.010.

R. Canelas, R. M. Ferreira, A. J. Crespo, and J. Domínguez. A generalized sph-dem discretization for the modelling of complex multiphasic free surface flows. In *Proceedings of the 8th International SPHERIC Workshop*, pages 74–79, 2013.

R. B. Canelas, A. J. Crespo, J. M. Domínguez, R. M. Ferreira, and M. Gómez-Gesteira. Sph–dcdem model for arbitrary geometries in free surface solid–fluid flows. *Computer Physics Communications*, 202 (Supplement C):131 – 140, 2016. ISSN 0010-4655. doi: https://doi.org/10.1016/j.cpc.2016.01.006.

A. Carlebur. Full-scale collision tests. *Safety science*, 19(2-3):171–178, 1995.

P. M. Carrica, R. V. Wilson, R. W. Noack, and F. Stern. Ship motions using single-phase level set with dynamic overset grids. *Computers and Fluids*, 36(9):1415–1433, 2007. ISSN 00457930. doi: 10.1016/j.compfluid.2007.01.007.

A. Colagrossi and M. Landrini. Numerical simulation of interfacial flows by smoothed particle hydrodynamics. *Journal of Computational Physics*, 191 (2):448–475, 2003. ISSN 00219991. doi: 10.1016/S0021-9991(03)00324-3.

A. Colagrossi, M. Antuono, and D. Le Touzé. Theoretical considerations on the free-surface role in the smoothed-particle-hydrodynamics model. *Physical Review E*, 79(5):056701, 2009.

S. J. Cummins and M. Rudman. An sph projection method. *Journal of computational physics*, 152(2):584–607, 1999.

W. Dehnen and H. Aly. Improving convergence in smoothed particle hydrodynamics simulations without pairing instability. *Monthly Notices of the Royal Astronomical Society*, 425(2):1068–1082, 2012.

S. Doocy, A. Daniels, C. Packer, A. Dick, and T. D. Kirsch. The human impact of earthquakes: a historical review of events 1980-2009 and systematic literature review. *PLoS currents*, 5, 2013.

H. Fayed and A. Atiya. An evaluation of the integral of the product of the error function and the normal probability density with application to the bivariate normal integral. *Mathematics of Computation*, 83(285):235–250, 2014.

FEMA. *Coastal construction manual: Principles and practices of planning, siting, designing, constructing, and maintaining residential buildings in coastal areas*, volume 2. Federal Emergency Management Agency, Mitigation Directorate, 2000.

FEMA. *Engineering Principles and Practices for Retrofitting Flood-Prone Residential Structures*. Federal Emergency Management Agency, 2001.

M. Ferrand, A. Joly, C. Kassiotis, D. Violeau, A. Leroy, F.-X. Morel, and B. D. Rogers. Unsteady open boundaries for SPH using semi-analytical conditions and Riemann solver in 2D. *Computer Physics Communications*, 210:29–44, 2017. ISSN 00104655. doi: 10.1016/j.cpc.2016.09.009.

U. Ghani, P. R. Wormleaton, and H. N. HASHMI. Three dimensional cfd modeling of flow structure in compound channels. *Mehran University Research Journal of Engineering and Technology*, 29(4):557–568, 2010.

J. N. Ghazali and A. Kamsin. A real time simulation and modeling of flood hazard. In *WSEAS International Conference. Proceedings. Mathematics and Computers in Science and Engineering*, number 12. WSEAS, 2008.

U. Ghia, K. N. Ghia, and C. Shin. High-re solutions for incompressible flow using the navier-stokes equations and a multigrid method. *Journal of computational physics*, 48(3):387–411, 1982.

R. A. Gingold and J. J. Monaghan. Smoothed particle hydrodynamics - Theory and application to non-spherical stars. , 181:375–389, Nov. 1977. doi: 10.1093/mnras/181.3.375.

K. Gong, B. Wang, and H. Liu. Modelling water entry of a wedge by multiphase sph method. *Coastal Engineering Proceedings*, 1(32):10, 2011.

K. Guo, P.-n. Sun, X.-y. Cao, and X. Huang. A 3-D SPH model for simulating water flooding of a damaged floating structure. *Journal of Hydrodynamics*, 29(5):831–844, 2017. ISSN 1001-6058. doi: 10.1016/S1001-6058(16)60795-3.

M. Gómez-Gesteira, D. Cerqueiro, C. Crespo, and R. Dalrymple. Green water overtopping analyzed with a sph model. *Ocean Engineering*, 32(2): 223–238, 2005. doi: 10.1016/j.oceaneng.2004.08.003.

I. Hadžić, J. Hennig, M. Perić, and Y. Xing-Kaeding. Computation of flow-induced motion of floating bodies. *Applied Mathematical Modelling*, 29 (12):1196–1210, 2005. ISSN 0307904X. doi: 10.1016/j.apm.2005.02.014.

R. B. Haehnel and S. F. Daly. Maximum impact force of woody debris on floodplain structures. *Journal of Hydraulic Engineering*, 130(2):112–120, 2004.

S. Haris and J. Amdahl. An analytical model to assess a ship side during a collision. *Ships and Offshore Structures*, 7(4):431–448, 2012.

W. D. Henshaw and D. W. Schwendeman. An adaptive numerical scheme for high-speed reactive flow on overlapping grids. *Journal of Computational Physics*, 191(2):420–447, 2003. ISSN 00219991. doi: 10.1016/S0021-9991(03)00323-1.

K. Hu, C. G. Mingham, and D. M. Causon. Numerical simulation of wave overtopping of coastal structures using the non-linear shallow water equations. *Coastal engineering*, 41(4):433–465, 2000.

P. Incardona, A. Leo, Y. Zaluzhnyi, R. Ramaswamy, and I. F. Sbalzarini. Openfpm: A scalable open framework for particle and particle-mesh codes on parallel computers. *arXiv preprint arXiv:1804.07598*, 2018.

G. J.A.C., H. H.J., and S. S. Convection cells in vibrating granular media. *Physical Review Letters*, 69(9):pp. 1371–1374, 1992.

G. R. Johnson and W. H. Cook. A constitutive model and data for materials subjected to large strains, high strain rates, and high temperatures. *Proc. 7th Inf. Sympo. Ballistics*, pages 541–547, 1983.

G. R. Johnson and W. H. Cook. Fracture characteristics of three metals subjected to various strains, strain rates, temperatures and pressures. *Engineering fracture mechanics*, 21(1):31–48, 1985.

B. Kallemov, A. P. S. Bhalla, B. E. Griffith, and A. Donev. An immersed boundary method for rigid bodies. *Communications in Applied Mathematics and Computational Science*, 11(1):79–141, 2016. ISSN 21575452. doi: 10.2140/camcos.2016.11.79.

H.-M. Kao and T.-J. Chang. Numerical modeling of dambreak-induced flood and inundation using smoothed particle hydrodynamics. *Journal of hydrology*, 448:232–244, 2012.

S. Khorasanizade and J. M. M. Sousa. An innovative open boundary treatment for incompressible SPH. (August 2015):161–180, 2016.

O. Kitamura. Fem approach to the simulation of collision and grounding damage. *Marine Structures*, 15(4-5):403–428, 2002.

J. Klapp and L. D. G. Sigalotti. Computers and Fluids. 159:177–188, 2017. doi: 10.1016/j.compfluid.2017.09.020.

K. M. Kleefsman, G. Fekken, A. E. Veldman, B. Iwanowski, and B. Buchner. A Volume-of-Fluid based simulation method for wave impact problems. *Journal of Computational Physics*, 206(1):363–393, 2005. ISSN 10902716. doi: 10.1016/j.jcp.2004.12.007.

S. Koshizuka and Y. Oka. Moving-particle semi-implicit method for fragmentation of incompressible fluid. *Nuclear science and engineering*, 123 (3):421–434, 1996.

H. Kruggel-Emden, S. Rickelt, S. Wirtz, and V. Scherer. A study on the validity of the multi-sphere discrete element method. *Powder Technology*, 188(2):153–165, 2008.

P. Kunz, M. Hirschler, M. Huber, and U. Nieken. Inflow/outflow with Dirichlet boundary conditions for pressure in ISPH. *Journal of Computational Physics*, 326:171–187, 2016. ISSN 0021-9991. doi: 10.1016/j.jcp.2016.08.046.

G. Kuwabara and K. Kono. Restitution coefficient in a collision between two spheres. *Japanese journal of applied physics*, 26(8R):1230, 1987.

E.-S. Lee, C. Moulinec, R. Xu, D. Violeau, D. Laurence, and P. Stansby. Comparisons of weakly compressible and truly incompressible algorithms for the sph mesh free particle method. *Journal of Computational Physics*, 227(18):8417 – 8436, 2008. ISSN 0021-9991. doi: https://doi.org/10.1016/j.jcp.2008.06.005.

A. Leroy, D. Violeau, M. Ferrand, and C. Kassiotis. Unified semi-analytical wall boundary conditions applied to 2-D incompressible SPH. *Journal of Computational Physics*, 261:106–129, 2014. ISSN 00219991. doi: 10.1016/j.jcp.2013.12.035.

A. Leroy, D. Violeau, M. Ferrand, L. Fratter, and A. Joly. A new open boundary formulation for incompressible SPH. *Computers and Mathematics with Applications*, 72(9):2417–2432, 2016. ISSN 0898-1221. doi: 10.1016/j.camwa.2016.09.008.

D. Lesuer. R., kay, g, j., and leblanc, m, m.,"modeling large–strain, high-rate deformation in metals". In *Third Biennial Tri-Laboratory Engineering Conference Modelling and Simulation, CA USA*, 1999.

Q. Liang, K.-c. Chen, J. Hou, Y. Xiong, G. Wang, and J. Qiang. Hydrodynamic modelling of flow impact on structures under extreme flow conditions. *Journal of Hydrodynamics*, 28(2):267–274, 2016.

L. D. Libersky, A. G. Petschek, T. C. Carney, J. R. Hipp, and F. A. Allahdadi. High strain lagrangian hydrodynamics: A three-dimensional sph

code for dynamic material response. *Journal of Computational Physics*, 109(1):67 – 75, 1993. ISSN 0021-9991. doi: https://doi.org/10.1006/jcph.1993.1199.

G. R. Liu and M. B. Liu. *Smoothed Particle Hydrodynamics - A Meshfree Particle Method*, volume 68. 2003. ISBN 9789812564405. doi: 10.1142/9789812564405.

L. B. Lucy. A numerical approach to the testing of the fission hypothesis. , 82:1013–1024, Dec. 1977. doi: 10.1086/112164.

J. R. Macdonald. Some simple isothermal equations of state. *Reviews of Modern Physics*, 38(4):669, 1966.

F. Macia Lang, A. Souto Iglesias, M. Antuono, and A. Colagrossi. Benefits of using a wendland kernel for free-surface flows. 2011.

S. Marrone, M. Antuono, A. Colagrossi, G. Colicchio, D. Le Touzé, and G. Graziani. Violent fluid-structure impacts solved through a δ-sph model. In *5th SPHERIC workshop*, 2010.

A. Mayrhofer, B. D. Rogers, D. Violeau, and M. Ferrand. Investigation of wall bounded flows using SPH and the unified semi-analytical wall boundary conditions. *Computer Physics Communications*, 184(11):2515–2527, 2013. ISSN 00104655. doi: 10.1016/j.cpc.2013.07.004.

A. Mayrhofer, M. Ferrand, C. Kassiotis, D. Violeau, and F. X. Morel. Unified semi-analytical wall boundary conditions in SPH: analytical extension to 3-D. *Numerical Algorithms*, 68(1):15–34, 2015a. ISSN 15729265. doi: 10.1007/s11075-014-9835-y.

A. Mayrhofer, D. Laurence, B. D. Rogers, and D. Violeau. DNS and LES of 3-D wall-bounded turbulence using Smoothed Particle Hydrodynamics. *Computers and Fluids*, 115(April):86–97, 2015b. ISSN 00457930. doi: 10.1016/j.compfluid.2015.03.029.

M.Ferrand, D.R.Lurence, D.Rogers, D. Violeau, and C. Kassiotis. Unified semi-analytical wall boundary conditions for inviscid,laminar or turbulent

flows in the meshless SPH method. *International Journal for Numerical Methods in Fluids*, 71(4):446–472, 2011. doi: 10.1002/fld.3666.

D. Molteni and A. Colagrossi. A simple procedure to improve the pressure evaluation in hydrodynamic context using the sph. *Computer Physics Communications*, 180(6):861 – 872, 2009. ISSN 0010-4655. doi: https://doi.org/10.1016/j.cpc.2008.12.004.

J. Monaghan and A. Kos. Solitary waves on a cretan beach. *Journal of waterway, port, coastal, and ocean engineering*, 125(3):145–155, 1999.

J. J. Monaghan. Smoothed particle hydrodynamics. *Annual review of astronomy and astrophysics*, 30(1):543–574, 1992.

J. J. Monaghan. Simulating free surface flows with SPH. *J. Comput. Phys.*, 110:399–406, 1994.

J. J. Monaghan and A. Kos. Scott russell's wave generator. *Physics of Fluids*, 12(3), 2000.

J. Monaghan, J. Smoothed Particle Hydrodynamics. *Annual Review of Astronomy and Astrophysics*, 30:543–574, 1992. ISSN 0066-4146. doi: 10.1146/annurev.aa.30.090192.002551. URL http://adsabs.harvard.edu/full/1992ARA{&}A..30..543M.

J. P. Morris, P. Fox, and Y. Zhu. Modeling low reynolds number incompressible flows using sph. *Journal of Computational Physics*, 136(1):214–226, 1997.

H. P. Morvan. *Three-dimensional simulation of river flood flows*. PhD thesis, University of Glasgow, 2001.

B. Nassauer, T. Liedke, and M. Kuna. Development of a coupled discrete element (DEM)–smoothed particle hydrodynamics (SPH) simulation method for polyhedral particles. *Computational Particle Mechanics*, 3(1):95–106, 2016. ISSN 2196-4378. doi: 10.1007/s40571-015-0097-9.

G. Oger, M. Doring, B. Alessandrini, and P. Ferrant. Two-dimensional SPH simulations of wedge water entries. *Journal of Computational Physics*, 213(2):803–822, 2006a. ISSN 00219991. doi: 10.1016/j.jcp.2005.09.004.

G. Oger, M. Doring, B. Alessandrini, and P. Ferrant. Two-dimensional sph simulations of wedge water entries. *Journal of Computational Physics*, 213:803–822, 2006b.

C. P.A. and S. O.D.L. A discrete numerical model for granular assemblies. *Geotechnique*, 29:pp. 47–65, 1979.

G. Pahar and A. Dhar. Robust boundary treatment for open-channel flows in divergence-free incompressible sph. *Journal of Hydrology*, 546:464–475, 2017.

A. Panizzo, T. Capone, and R. Dalrymple. Accuracy of kernel derivatives and numerical schemes in sph. *Submitted to Journal of Computational Physics*, 2007.

H. P.K. and W. B.T. Computer simulation of the mechanical sorting of grains. *Powder Technology*, 48:pp. 239–245, 1986.

A. V. Potapov, M. L. Hunt, and C. S. Campbell. Liquid-solid flows using smoothed particle hydrodynamics and the discrete element method. *Powder Technology*, 116(2-3):204–213, 2001. ISSN 00325910. doi: 10.1016/S0032-5910(00)00395-8.

M. Prakash, K. Rothauge, and P. W. Cleary. Modelling the impact of dam failure scenarios on flood inundation using SPH. *Applied Mathematical Modelling*, 38(23):5515–5534, 2014. ISSN 0307904X. doi: 10.1016/j.apm.2014.03.011.

S. Quallen, T. Xing, P. Carrica, Y. Li, and J. Xu. CFD Simulation of a Floating Offshore Wind Turbine System Using a Quasi-static Crowfoot Mooring-Line Model. *Journal of Ocean and Wind Energy*, 1(3):143–152, 2014. ISSN 10986189. URL http://www.isope.org/publications.

B. Ren, Z. Jin, R. Gao, Y.-x. Wang, and Z.-l. Xu. Sph-dem modeling of the hydraulic stability of 2d blocks on a slope. *Journal of Waterway, Port, Coastal, and Ocean Engineering*, 140(6):04014022, 2013.

B. Ren, M. He, P. Dong, and H. Wen. Nonlinear simulations of wave-induced motions of a freely floating body using WCSPH method. *Applied Ocean Research*, 50:1–12, 2015. ISSN 01411187. doi: 10.1016/j.apor.2014.12.003.

D. M. Robb, S. Gaskin, and J.-C. Marongiu. SPH-DEM model for free-surface flows containing solids applied to river ice jams. *Journal of Hydraulic Research*, 54(1):27–40, 2016. ISSN 00221686. doi: 10.1080/00221686.2015.1131203.

M. Robinson and M. Ramaioli. Mesoscale fluid-particle interaction using two-way coupled sph and the discrete element method. In *Proceedings of the 6th SPHERIC Workshop*, pages 72–78, 2011.

M. Robinson, M. Ramaioli, and S. Luding. Fluid-particle flow simulations using two-way-coupled mesoscale SPH-DEM and validation. *International Journal of Multiphase Flow*, 59:121–134, 2014. ISSN 03019322. doi: 10.1016/j.ijmultiphaseflow.2013.11.003.

N. Rüther and Ø. Pedersen. 3d numerical modeling of the flow over a gravel river bed due to hydropower peaking. *STAMM, J.(Hg.): Simulationsverfahren und Modelle für Wasserbau und Wasserwirtschaft*, 37: 375–382, 2014.

M. Sarfaraz and A. Pak. An integrated SPH-polyhedral DEM algorithm to investigate hydraulic stability of rock and concrete blocks: Application to cubic armours in breakwaters. *Engineering Analysis with Boundary Elements*, 84(July):1–18, 2017. ISSN 09557997. doi: 10.1016/j.enganabound.2017.08.002.

I. F. Sbalzarini, J. H. Walther, M. Bergdorf, S. E. Hieber, E. M. Kotsalis, and P. Koumoutsakos. Ppm–a highly efficient parallel particle–mesh library for the simulation of continuum systems. *Journal of Computational Physics*, 215(2):566–588, 2006.

H. T. Shen, J. Su, and L. Liu. SPH Simulation of River Ice Dynamics. *Journal of Computational Physics*, 165(2):752–770, 2000. ISSN 00219991. doi: 10.1006/jcph.2000.6639.

L. Shen and E. S. Chan. Numerical simulation of fluid-structure interaction using a combined volume of fluid and immersed boundary method. *Ocean Engineering*, 35(8-9):939–952, 2008. ISSN 00298018. doi: 10.1016/j.oceaneng.2008.01.013.

M. Spiga and G. Morino. A symmetric solution for velocity profile in laminar flow through rectangular ducts. *International communications in heat and mass transfer*, 21(4):469–475, 1994.

P. Sun, F. Ming, and A. Zhang. Numerical simulation of interactions between free surface and rigid body using a robust SPH method. *Ocean Engineering*, 98(April):32–49, 2015a. ISSN 00298018. doi: 10.1016/j.oceaneng.2015.01.019.

P. Sun, F. Ming, and A. Zhang. Numerical simulation of interactions between free surface and rigid body using a robust SPH method. *Ocean Engineering*, 98(April):32–49, 2015b. ISSN 00298018. doi: 10.1016/j.oceaneng.2015.01.019.

X. Sun, M. Sakai, and Y. Yamada. Three-dimensional simulation of a solid-liquid flow by the DEM-SPH method. *Journal of Computational Physics*, 248:147–176, 2013. ISSN 00219991. doi: 10.1016/j.jcp.2013.04.019.

C. Ulrich and T. Rung. Multi-physics sph simulations of launching problems and floating body interactions. In *ASME 2012 31st International Conference on Ocean, Offshore and Arctic Engineering*, pages 685–694. American Society of Mechanical Engineers, 2012.

USACE. Shore protection manual: Volume ii. *US Army Corps of Engineers*, 1984.

R. Vacondio, B. Rogers, P. Stansby, P. Mignosa, and J. Feldman. Variable resolution for sph: a dynamic particle coalescing and splitting scheme. *Computer Methods in Applied Mechanics and Engineering*, 256:132–148, 2013.

R. B. S. P. M. P. Vacondio, R. SPH modeling of shallow flow with open boundaries for practical flood simulation. *J. Hydraul. Eng.*, 138 (6):530–541, 2012.

S. Varrette, P. Bouvry, H. Cartiaux, and F. Georgatos. Management of an academic hpc cluster: The ul experience. In *Proc. of the 2014 Intl. Conf. on High Performance Computing & Simulation (HPCS 2014)*, pages 959–967, Bologna, Italy, July 2014. IEEE.

D. Violeau and B. D. Rogers. Smoothed particle hydrodynamics (SPH) for free-surface flows: Past, present and future. *Journal of Hydraulic Research*, 54(1):1–26, 2016. ISSN 00221686. doi: 10.1080/00221686.2015.1119209.

E. Walhorn, A. Kölke, B. Hübner, and D. Dinkler. Fluid–structure coupling within a monolithic model involving free surface flows. *Computers & structures*, 83(25-26):2100–2111, 2005.

O. R. Walton and R. L. Braun. Viscosity, granular-temperature, and stress calculations for shearing assemblies of inelastic, frictional disks. *Journal of rheology*, 30(5):949–980, 1986.

Y.-h. Wang, Y.-s. Zou, L.-q. Xu, and Z. Luo. Analysis of water flow pressure on bridge piers considering the impact effect. *Mathematical Problems in Engineering*, 2015, 2015.

K. Wu, D. Yang, and N. Wright. A coupled SPH-DEM model for fluid-structure interaction problems with free-surface flow and structural failure. *Computers and Structures*, 177(August):141–161, 2016. ISSN 00457949. doi: 10.1016/j.compstruc.2016.08.012.

L. Zhen, T. Bin, D.-Z. Ning, and G. Ying. Wave-current interactions with three-dimensional floating bodies. *Journal of Hydrodynamics, Ser. B*, 22 (2):229–240, 2010.